RECOMBINATION MECHANISMS IN GALLIUM ARSENIDE

A STUDY OF RECOMBINATION MECHANISMS IN GALLIUM ARSENIDE USING TEMPERATURE-DEPENDENT TIME-RESOLVED PHOTOLUMINESCENCE

By MARTIN W. GERBER, B.A.Sc., B.S.

A Thesis Submitted to the School of Graduate Studies in Partial Fulfilment of the Requirements for the Degree Doctor of Philosophy

McMaster University DOCTOR OF PHILOSOPHY (2016)
Hamilton, Ontario (Engineering Physics)

TITLE: A Study of Recombination Mechanisms in Gallium Arsenide using Temperature-Dependent Time-Resolved Photoluminescence
AUTHOR: Martin W. Gerber, B.A.Sc. (University of Toronto), B.S. (McMaster University)
SUPERVISOR: Professor Rafael N. Kleiman
NUMBER OF PAGES: xxiv,132

Abstract

Recombination mechanisms in gallium arsenide have been studied using temperature-dependent time-resolved photoluminescence-decay. New analytical methods are presented to improve the accuracy in bulk lifetime measurement, and these have been used to resolve the temperature-dependent lifetime. Fits to temperature-dependent lifetime yield measurement of the radiative-efficiency, revealing that samples grown by the Czochralski and molecular-beam-epitaxy methods are limited by radiative-recombination at 77K, with defect-mediated nonradiative-recombination becoming competitive at 300K and above. In samples grown with both doping types using molecular-beam-epitaxy, a common exponential increase in capture cross-section characterized by a high value of $E_\infty = (258 \pm 1)meV$ was observed from the high-level injection lifetime over a wide temperature range (300-700K). This common signature was also observed from 500-600K in the hole-lifetime observed in n-type Czochralski GaAs where $E_\infty = (261 \pm 7)meV$ was measured, which indicates that this signature parametrizes the exponential increase in hole-capture cross-section. The high E_∞ value rules out all candidate defects except for EL2, by comparison with hole-capture cross-section data previously measured by others using deep-level transient spectroscopy.

Acknowledgements

This work would not have been possible without the patience and support of my wife, Alyshia. She has been by my side through every triumph and challenge, encouraging me and assuring me that everything would all come together in the end. Dating back to my undergrad senior thesis days, Alyshia would ask me questions about my research and want me to explain it to her. Whenever I came home with exciting results, she would want to hear all about it. She has come along with me on my journey, and has picked me back up when I have fallen down.

The guidance offered by my supervisor, Dr. Rafael Kleiman, has been invaluable. When presented with baffling experimental results that challenged my understanding of the underlying physics, Dr. Kleiman was supportive and taught me that the greatest satisfaction comes from making sense of the seemingly inexplicable. While providing me with excellent supervision, he encouraged me to be creative and generate my own solutions to theoretical and experimental problems. The academic freedom that Dr. Kleiman provided gave me the opportunity to explore and discover, while his profound insights pointed me in the right direction. I am thankful to have had the opportunity to develop my abilities in this imaginative environment.

My committee members Dr. Harold Haugen and Dr. Qiyin Fang went out of their way to provide exceptional guidance. With their shared expertise, I avoided many technical pitfalls in the design of my experimental system. They were engaged during our annual meetings, and corresponded with me to advise me during my experimental design. In the early stages Dr. Fang often lent me equipment, which allowed me to refine my design so that the final system met our experimental needs.

When I began graduate studies, I was new to the world of solid-state physics. I struggled to learn these concepts on my own, and made some headway. It was truly during Dr. Peter Mascher's solid-state course that I developed a depth of understanding and appreciation for the beauty of semiconductor physics. His lectures were structured in a way that taught us how to analyze the literature, and this amplified my enjoyment of exploring scientific journals. Dr. Mascher helped me make sense of a mysterious field, and patiently engaged in the long after-class discussions that led me to feel confident in my understanding.

Dr. Shahram Tavakoli went beyond the hours spent growing the atomic layers our molecular beam epitaxy crystals, one by one, and made time to teach me how to cleave wafers and mount electrical contacts in the hydrogen-chloride reactor.

During my first attempts at theoretically modelling the physics underlying my future experiments, I was apprehensive about investing time on a problem for which there may be no solution. Discussions with Manuel Gil helped to build confidence in my mathematical approach, and assure me that I was on the right track.

At one point, I was feeling particularly discouraged about my progress. After a memorable conversation with George Chiran, I was left with sustained motivation and the feeling that my research was of value to the scientific community. George often expressed an interest in my research, and became a supportive friend.

Throughout my time at McMaster, I have engaged in countless discussions with Abhi Rampal. While usually scientific in nature, our discussions often covered broader ground and I learned a lot about the world from him. He was never too busy for technical troubleshooting, or to teach me how to etch the InGaP capping layer from my samples. His enthusiasm is bottomless, and his curiosity never waivers. It has been enriching to have a friend that shares my passion for finding truth.

Thanks to my friends who have stayed in touch, even when I became so engrossed in my research that I forgot how to pick up the phone. Balance between lab life and quality time spent with good people helped me face challenges with renewed energy. Many of us would get together to make music, which would take my mind off of things so that I could come back to the problem at hand with a fresh perspective. Time spent with all of you has reminded me of what life is like outside the lab.

Of course, none of the experimental work would have been possible without the financial support of the Canada Foundation for Innovation, the Ontario Research Fund and the Natural Sciences and Engineering Research Council of Canada.

Finally, I am thankful for the support that I have received from my family. My parents have encouraged my interests in science, while giving me opportunities to develop hobbies. In my younger days, my parents were there to provide the motivation that I would often lack. Now, they remain a source of love, support, inspiration and guidance. While the nature of carrier dynamics in gallium arsenide might not make the most exciting dinner conversation, my family has expressed ongoing curiosity about my research. Through these discussions at family gatherings, I have made new connections while searching for ways to describe my research in common language.

Contents

List of Figures

List of Abbreviations and Symbols

α	Absorptivity (at the excitation wavelength)
α_{BB}	Band-to-band absorption coefficient
ΔE_t	Depth of defect energy level from nearest band
Δn	Excess carrier-density
η	Injection level ($\eta = \Delta n/(n_o + p_o)$)
$\hbar$	Planck constant (divided by 2π)
ρ	Radial cylindrical coordinate
$\rho_{tail}(E)$	Modified conduction-band density of states
σ_ℓ	Minority-carrier trap-capture cross-section
σ_ρ	Breadth of the Gaussian excitation beam
σ_n	Electron-capture cross-section
σ_n^S	Electron capture cross-section for surface states
σ_p	Hole-capture cross-section
σ_p^S	Hole capture cross-section for surface states
τ_ρ	Radial diffusion time-constant
τ_p	Hole-lifetime
τ_r	Radiative lifetime

τ_S Effective two-surface loss time constant [4]

τ_z Axial diffusion time-constant

$\tau_{bulk}(T)$ Temperature dependent lifetime signal

τ_{FS} Front-surface loss (diffusion-related) time-constant

τ_{HLI} High-level injection SRH-lifetime

τ_{LLI} Low-level injection SRH-lifetime

τ_{maj} Majority carrier lifetime

τ_{min} Minority carrier lifetime

τ_{nr} Nonradiative lifetime

τ_{SRH} Shockley-Read-Hall lifetime

τ_{tr} Transit time-constant for axial diffusion

A_{diff}, $R(\rho,t)$, $Z(B_z(z,t),C_z(z,t))$ Magnitude and separable (cylindrical) solutions to the semi-infinite diffusion problem with surface loss

$B(T)$ Radiative recombination coefficient

c Speed of light

C_{3v} Trigonal symmetry group

D_a Ambipolar diffusivity

E_ℓ Effective energy level of localized states

E_C Conduction band energy level ($E_C = E_g$)

E_F Fermi energy

E_F^n Quasi-Fermi level (electrons)

E_F^p Quasi-Fermi level (holes)

E_g Bandgap energy

E_V Valence band energy level ($E_V = 0$)

$f(T)$ Radiative efficiency ($f = \tau_{bulk}/\tau_r$)

$I_{PL}(t)$ Expected PL signal

k Asymmetry ratio $k \equiv \sigma_n/\sigma_p$

k_B Boltzmann constant

m^* Effective mass

N_ℓ Effective density of localized states

$N_C(T)$ Conduction-band effective density-of-states

n_i Intrinsic carrier density

$n_o + p_o$ Total equilibrium density of electrons (n_o) and holes (p_o)

N_T Total number of photons in excitation pulse

N_t Total trap-density

$N_V(T)$ Valence-band effective density-of-states

n_{ref} Refractive index

r Ratio of HLI and LLI lifetimes ($r = \tau_{HLI}/\tau_{LLI}$)

r_σ Ratio of high- to low-temperature cross-sections

S Surface recombination velocity

S_{min} Minority-carrier surface recombination velocity

T_d Tetrahedral symmetry group

U_{rad} Radiative recombination

v_{th} Thermal velocity ($v_{th} = \sqrt{\frac{3k_BT}{m^*}}$)

W Sample width

z Axial cylindrical coordinate

APD Avalanche photodiode

CFD Constant fraction discriminator

CZ Czochralski

DH Double hetero-structure

DLTS Deep-level transient spectroscopy

DOS Density of states

EO Edmund Optics

EPR Electron paramagnetic resonance

HLI High-level injection

IR Infrared

LLI Low-level injection

LPE Liquid phase epitaxy

LS Lifetime spectroscopy

MBE Molecular beam epitaxy

MOCVD Metalorganic chemical vapour deposition

MPE Multi-phonon-emission

NTD Neutron-transmutation doping

OD Optical density

ODENDOR Optically detected electron-nuclear double resonance

ODEPR Optically detected electron paramagnetic resonance

PC Photoconductance

PL Photoluminescence

QSS Quasi-steady-state

SRH Shockley-Read-Hall

TAC Time-to-amplitude converter

TCSPC Time-correlated single-photon counting

TD-TR-PLD Temperature-dependent time-resolved PL-decay

TR-PL Time-reolved photoluminescence

TR-PLD Time-resolved photoluminescence-decay

Declaration of Academic Achievement

With the support and guidance of Dr. Rafael Kleiman, I have developed all theoretical models contained in this thesis. I designed, assembled, and aligned the described experimental temperature-dependent time-resolved photoluminescence-decay system, and performed each measurement, as well as the data analysis. Molecular beam epitaxial growth of our GaAs samples was performed by Dr. Shahram Tavakoli.

Chapter 1

Introduction

Using a new temperature-dependent time-resolved photoluminescence decay (TD-TR-PLD) system, I have been able to resolve the temperature-dependent bulk-lifetime (τ_{bulk}) and radiative efficiency ($f(T)$) in GaAs samples grown using Czochralski (CZ) and molecular-beam-epitaxy (MBE). Measurement of $f(T)$ is possible using TD-TR-PLD because the radiative (τ_r) and nonradiative (τ_{nr}) lifetimes follow opposite temperature dependence, so this method does not rely on comparison to the theoretical radiative lifetime. While these methods are demonstrated on GaAs, the TD-TR-PLD system has been built to accommodate many different materials to allow for the measurement of $f(T)$ in other direct bandgap semiconductors. High $f(T)$ is required to meet the thermodynamic maximum for power-conversion efficiency of photovoltaic solar cells [14], and is equally important for maximizing output-intensity of light-emitting diodes [15] and solid-state lasers [16].

When direct bandgap semiconductors are heated, the capture cross-sections (σ) of defects often undergo an exponential increase, characterized by E_∞. By fitting the temperature-dependent τ_{bulk}, I have found that the measurement of E_∞ is possible. This enables characterization of the dominant defect that limits τ_{bulk} and $f(T)$ in the material, which is important because it provides a signature that can be used to identify that defect. Once the dominant defect has been identified, research efforts

can be focused on eliminating the defect, or mitigating its negative electronic effects. Defects that reduce $f(T)$ [14] and τ_{bulk} [17] limit photovoltaic cell-efficiency at the bulk material-quality level, and cell-efficiency is the predominant factor affecting the economics of solar energy [18]. The σ of many direct bandgap semiconductors (e.g. GaAs [8, 9, 11, 19], GaP [11], InGaP [20], GaAsN [21], InP [22], InGaAs [23]) have been previously characterized using deep-level-transient spectroscopy (DLTS) and defects in these materials were found to exhibit this exponential change in σ, which makes these dominant-defect characterization methods widely applicable.

Decades of research with DLTS have characterized many of the electronic properties of defects in as-grown and intentionally-contaminated GaAs, including the measurement of temperature-dependent electron- (σ_n) and hole-capture (σ_p) cross-sections. The σ_n and σ_p of many defects in GaAs undergo an exponential increase proportional to e^{-E_∞/k_BT} when temperature is increased, and their E_∞ have been reported in the literature. This existing knowledge is extremely valuable to the association of defects characterized using TD-TR-PLD with those already studied by DLTS, based on the measured E_∞. Through application of complementary techniques and theoretical modelling, some of these defects have been associated with intrinsic crystallographic defects (As- and Ga-related) and extrinsic impurities. While we understand much about the electronic properties of defects in GaAs, there is still no clear consensus as to what defect plays the dominant role in recombination [10]. Temperature dependent τ_{bulk} analysis provides a new means of applying the information gleaned from DLTS-based studies to identify the specific defect that limits the carrier lifetime.

In my experiments, I have observed a characteristic drop in τ_{bulk} in GaAs samples grown using CZ and MBE when heated above 300K, associated with the exponential increase in σ. Fits to TD-TR-PLD have revealed that this change is characterized by the same E_∞ in samples grown using both growth methods. The hole-lifetime (τ_p) has been measured in the TD-TR-PLD experiments on n-CZ-GaAs, where the injected carrier density was orders of magnitude below the doping level. Because of

this low-level of injection (LLI), we can associate the common E_∞ with a change in σ_p. The lifetime drops too abruptly to be consistent with most characterized defects in GaAs; however, the behaviour is consistent with the known σ_p of the EL2 defect.

The EL2 defect has received more attention than any other defect in GaAs [24], and is of both technical and scientific interest [25]. While EL2 was associated with the arsenic antisite defect (As_{Ga}) [26–28], several experimental findings (such as the observed low-temperature metastability) could not be explained by the isolated-As_{Ga} defect [25]. While scientifically interesting, the metastable-state only exists below 140K [29] where radiative recombination limits the lifetime, and is therefore not relevant to defect-characterization and device operation near 300K. Some past studies from GaAs grown using various methods have indicated EL2 as the lifetime-limiting defect [30, 31], while others have claimed limitation by HL10 [9], EL6 [10], and EL5 [12]. The most recent conclusion [31] indicating EL2 as the dominant defect relies on the observation that both the recombination current and EL2-density varied by about three orders of magnitude between GaAs p^+-n junctions grown using metalorganic chemical vapour deposition (MOCVD) and CZ methods; however, this result could be spurious as some other defect density may have also changed by three orders of magnitude between growth methods. There is an unsettled debate as to what defect limits the lifetime in GaAs, and experimental work with temperature-dependent τ_{bulk} measurement provides missing clues that can potentially answer this standing question.

TR-PLD from GaAs is not monoexponential [32], and accurate physical modelling is essential for resolution and analysis of the temperature-dependent τ_{bulk} signal and $f(T)$. To address this, I have developed new analytical models, and these have enabled measurement of τ_{bulk} and $f(T)$ from this nonlinear decay. In thick materials, nonlinearity arises due to diffusion and surface recombination. Vaitkus [3] solved the diffusion problem for the semi-infinite slab with arbitrary surface-recombination velocity (S), and I have generalized this model to three dimensions. In studying this theory further, I have found that TR-PLD from thick (in relation to the diffusion length),

unpassivated materials has a time-dependence of $e^{-t/\tau_{bulk}}/\sqrt{t}$. Experimentally, I have found that this approximation is applicable from 77-700K. This greatly simplifies the interpretation and analysis of TR-PLD from thick, unpassivated samples and provides confidence in the analytical model and the measured τ_{bulk}.

Nonlinearity also arises due to the presence of localized states. This is typically accounted for by fitting a monoexponential subset of the TR-PLD, or by performing a biexponential fit. By modelling the system with one dominant localized energy level, I improve upon the biexponential modelling of trapping processes and derive an analytical relationship that illuminates the relationship between the measured parameters and the trap-capture (τ_o), trap-emission (τ_1), trap-decay (τ_ℓ), and τ_{bulk} time constants. This new analytical model provides insight into the complex domain of trap-dominated TR-PLD, and allows extraction of more information than was previously possible.

Localization effects are commonly observed in GaAs photoluminescence (PL) spectra, and give rise to significant deviation between experiment and the PL spectrum calculated using the parabolic-band approximation of the density of states. This is the result of the formation of an exponential tail in the conduction-band density of states (DOS), which occurs above doping levels of ($10^{17}cm^{-3}$) in GaAs [33]. Halperin and Lax [34] have treated this topic with rigour; however, a clear method of fitting experimental data is not provided. By applying an area-preserving transformation to the parabolic-band DOS, I have found an analytical expression that exhibits the appropriate exponential tail (e^{E/E_o}). Using this new model, I have found that PL spectra with band-tail states can be fit, allowing for measurement of the Fermi level (E_F), bandgap (E_g), and E_o. Carrier density can be calculated from the extracted E_F, enabling a new contactless method of measuring the doping-level from PL spectra.

To obtain an accurate measurement of τ_{bulk} from TR-PLD, the laser power must be increased sufficiently to ensure quasi-equilibrium between the localized and extended states. Under these circumstances, TR-PLD is not monoexponential in thin-film

samples due to the nature of radiative recombination, leaving behind a limited dynamic range where monoexponential decay is observed. For the case where τ_{nr} remains sufficiently constant ($|\Delta\tau_{nr}|/\tau_{nr} \ll \tau_{nr}/\tau_r$) throughout the decay, I have found a new analytical model that accounts for both radiative and nonradiative recombination. This model provides new insight that can be used to interpret TR-PLD, explicitly illustrating the effects of $f(T)$, and the initial injection-level[1] (η_o). Since the intensity of the TR-PLD signal is nonlinear with injection-level (η), both η_o and $f(T)$ (as well as τ_{bulk}) can be measured by fitting with this new model.

The new models and experimental equipment allow for TD-TR-PLD measurements, providing a powerful method of characterizing defects that limit τ_{bulk} and $f(T)$. In order to identify these defects from extracted signatures, there must be sufficient information available from complementary techniques, such as DLTS. The complementarity of TD-TR-PLD and DLTS should encourage new development in this field, to address questions about recombination mechanisms in GaAs as well as other direct bandgap semiconductors. In particular, high-temperature DLTS is of great value to the identification of defects characterized by TD-TR-PLD, as this is where the information regarding E_∞ lies. While DLTS studies of GaAs are fairly comprehensive, there are significant gaps in the understanding of the electronic properties of defects in other compound semiconductors. Thorough high-temperature DLTS studies of σ_n and σ_p performed on a wider variety of direct bandgap semiconductors will allow the analysis of temperature-dependent τ_{bulk} to play a role in identifying the dominant defects in these material systems.

[1]The injection level ($\eta = \Delta n/(n_o + p_o)$) is the ratio of excess (Δn) and equilibrium ($n_o + p_o$) carrier densities.

Chapter 2

Literature Review

2.1 Lifetime Spectroscopy

Lifetime spectroscopy (LS) is a technique that allows for the characterization of the lifetime-limiting defect in a material. In LS, the lifetime-limiting defect is characterized through observation of the dependence of the carrier-lifetime on temperature, injection-level,[1] doping-level, and doping-type. A good description of the theory and history of LS in Si is given in [17]. The nature of LS changes dramatically in GaAs, as radiative recombination becomes 10,000 [17] times more likely than in Si, while the wide bandgap[2] and background doping[3] increase the onset temperature of the deep-level Arrhenius increase.

Application of LS in GaAs has been relatively limited. Bergman et al. [36] have measured the temperature dependence of the lifetime in p-type GaAs grown with

[1]The ratio of excess to (total) equilibrium carrier densities ($\Delta n/(n_o + p_o)$).

[2]To be clear, an Arrhenius increase could still be observed for shallow energy levels (close to the band edges); however, recombination is typically dominated by deep energy levels (near midgap) since they minimize the Shockley-Read-Hall lifetime [17, 35].

[3]The Arrhenius-increase onset-temperature increases with doping [17], and due to background doping incorporated unintentionally during growth it is challenging to achieve $< 10^{16} cm^{-3}$ doping in GaAs without the intentional addition of deep levels that leads to a semi-insulating material. Even if lower doping were possible, the large degree of localization and trap-emission screen the measurement of LLI lifetime in TR-PLD, which continues to complicate the Arrhenius analysis (see Section 5.3.2).

liquid-phase-epitaxy (LPE), and their results indicate that the lifetimes measured in their samples are radiatively limited at temperatures below 500K. Temperature dependent results were presented below 300K by Olson et al. [37] (see Section 2.2 for additional discussion), and the increase in lifetime with temperature demonstrated that radiative recombination is limiting in their lightly n-type ($\sim 10^{14} cm^{-3}$) MOCVD-GaAs.

Haughn et al. [38] have looked into injection level dependence, and conclude that recombination in each of their lightly p-type (background doped to $10^{15} cm^{-3}$) MOCVD-GaAs is defect-limited at 300K. Note that [38] is observing the effects of elevated MOCVD growth-rate for photovoltaic applications, and do not provide any measurements of samples grown below $14 \mu m/hr$. While Johnston and Ahrenkiel performed a comprehensive TD-TR-PLD study on MBE-GaAs samples [32] and commented on the potential of these types of measurements, they did not use the data to perform defect characterization or identification. They also studied unintentionally (background) doped (with $n_o < 10^{15} cm^{-3}$, [32]) samples, and their results are definitely indicative of defect-dominated recombination as the decay rate increases dramatically with temperature.

By mapping out these variations in the lifetime using TD-TR-PLD, I have been able to measure the radiative efficiency, which demonstrates a capability of LS in GaAs that is not possible in Si. Also, many defects in GaAs undergo large changes to their cross-section [8, 9, 11, 19] at elevated temperatures,[4] which provides an additional observable defect-parameter that is not screened by the Arrhenius increases observed [17] in Si. The measured temperature-dependent cross-section can then be used as the fingerprint for defect identification through comparison with previous studies using DLTS [8, 9, 11, 19].

[4]The exponential ($e^{-E_\infty / k_B T}$) increase is associated with the multi-phonon emission (MPE) capture mechanism [9, 11, 39]. While MPE capture dominates in GaAs [9, 11], Stefan Rein [17, pp. 179-183] reviews various mechanisms including: MPE-, cascade-, and Auger-capture.

2.2 Lifetime Measurement: Time-Resolved Photoluminescence Decay

Time-resolved photoluminescence (TR-PL) involves monitoring the intensity of light emitted by a material in response to some modulated excitation source. TR-PL experiments typically either monitor transient time-resolved photoluminescence decay (TR-PLD) following pulsed excitation, or quasi-steady-state PL (QSS-PL) in response to more slowly varied excitation. This thesis focuses on TR-PLD in GaAs;[5] however, the system that I have built (Section 4) can be expanded to allow for excitation by a modulated light source for quasi-steady-state PL (QSS-PL) lifetime measurements on a wide variety of semiconductor materials.[6] While QSS-PL has been applied to silicon [40, 41], it has not yet been applied to GaAs.

On the other hand, TR-PLD has a long history of use with GaAs. In early studies, Bludau and Wagner [43] used TR-PLD to measure the lifetime of the donor-acceptor transition at 2K, and Kamiya and Wagner [44] performed wavelength-resolved TR-PLD to measure the acceptor binding energies of carbon and silicon in GaAs. Nelson and Sobers varied doping [45] and sample width [46] and observed the changes in lifetime using TR-PLD in order to measure the interfacial recombination velocity in the AlGaAs-passivated double-heterostructure (DH),[7] using photon-recycling arguments to reconcile their lifetime and quantum-efficiency results. Olson et al. [37] later demonstrated the superior passivation quality of the InGaP/GaAs interface using comparative PLD measurements.

Lush et al. [47, 48] performed a comprehensive lifetime study on n-type GaAs

[5] While TRPL technically encompasses QSS-PL as well, it is currently the most common acronym used to refer TR-PLD.

[6] QSS-PL has been developed by Trupke et al. [40], and shown [41] to be less sensitive to trapping (and space-charge effects) than the original QSS-photoconductive (QSS-PC) technique proposed by Sinton and Cuevas [42].

[7] A DH is a layer of one material sandwiched between two relatively thin passivating layers with a larger bandgap. These layers electrically isolate the charge carriers, and reduce the density of surface states (and therefore also the interfacial recombination).

grown using metalorganic-chemical-vapour-deposition (MOCVD), and reported an anomalously high set of lifetimes exceeding the radiative limit for samples of a wide range of thicknesses from 250nm to $10\mu m$ (doped to 1.3×10^{17} to $3.8 \times 10^{18} cm^{-3}$). The reported lifetimes measured in these samples exceeded the radiative limit, in the most extreme example by a factor of 27 times [47], and this was attributed to photon recycling. The lifetime was further increased by removal of the optically absorbing substrate [47], and this is consistent with expectations based on photon recycling. The bulk lifetime was observed[8] [47, 48] to increase with sample thickness, and this increase is in agreement with the Asbeck model of photon recycling [49, 50].

Yablonovitch et al. [51] presented an elegant picture of radiative recombination, demonstrating that the rate of spontaneous emission depends on the refractive index of the surrounding medium. Beginning with Fermi's "Golden Rule", they derive a relation between the radiative lifetime and the refractive index of the surrounding medium. The idea of inhibited spontaneous emission had been a subject of investigation in atomic physics [51], and they demonstrated this phenomenon in the solid state. By using the lift-off technique that they developed [52], they were able to transfer the same undoped 500nm GaAs DH between three substrates (GaAs, TiO_2, SiO_2), and demonstrate that the lifetime increases with decreasing refractive index. The TR-PLD results demonstrate nonlinearity that the authors associate with radiative recombination. They argue that the large spread in measured radiative recombination coefficients ($B(T)$) in the literature is due to the dependence of the overall spontaneous emission rate on the optical properties of the GaAs and its surroundings. [51]

2.3 Defects in GaAs

Electrical characterization of deep levels in GaAs has been done by various groups [8, 9, 11, 19, 25, 30, 31, 53–57] using some variation of DLTS (first developed by

[8] The increase in τ_{bulk} is observed assuming a fixed interfacial recombination velocity.

Lang [53]) which involves monitoring the temperature-dependent transient depletion-capacitance following a perturbing voltage pulse.[9] DLTS research has provided measurement of energy-levels, cross-sections, and defect densities in GaAs [8, 9, 11, 19, 25, 57]. While DLTS provides information about many defects present in the material, the identification of the lifetime-limiting defect is typically restricted to either arguments based on comparison between the observed lifetime and estimates of minority lifetimes based on the DLTS-measured defect-densities and carrier cross-sections [9], or associations based on correlations with growth stoichiometry [30]. Previous studies from GaAs have indicated various defects as being dominant, such as: EL2 [30, 31], HL10 [9], EL6 [10], and EL5 [12]. TD-TR-PLD is an ideal complementary technique to DLTS, as it enables the measurement of defect parameters of the dominant defect. DLTS provides an excellent source of reproducible defect-parameters that can be used for identification of the lifetime-limiting defect with the parameters extracted from TD-TR-PLD. In this section, I provide a review of the most well-studied deep-level in GaAs, called EL2.[10]

2.3.1 EL2: $\mathbf{As_{Ga}}$+X

EL2 is the most researched defect in GaAs [24], and has received considerable attention from both applied and pure physicists [25]. A diagram illustrating the EL2 energy-levels (measured by [1]) is shown in Figure 2.1. The most basic model of EL2 is the isolated arsenic-antisite defect (As_{Ga}) [58]; however, it has been shown [28, 59] that EL2 must be a complex involving As_{Ga} (i.e. EL2=As_{Ga}+X, where X is some unknown defect). The association between EL2 and As_{Ga} was made first [26–28] based on correlation between growth stoichiometry and EL2 density [60].

[9] In DLTS, carriers are swept into the depletion region by the voltage pulse, and the re-emission of the carriers from these defect-states gives rise to a transient capacitance-signal. This transient capacitance signal is temperature-dependent, as are the emission properties of the defect. By sweeping the temperature and monitoring these transients, the defect parameters (energy-level, density, majority-carrier cross-section) can be extracted.

[10] The name EL2 was given to this defect by Martin et al. [54].

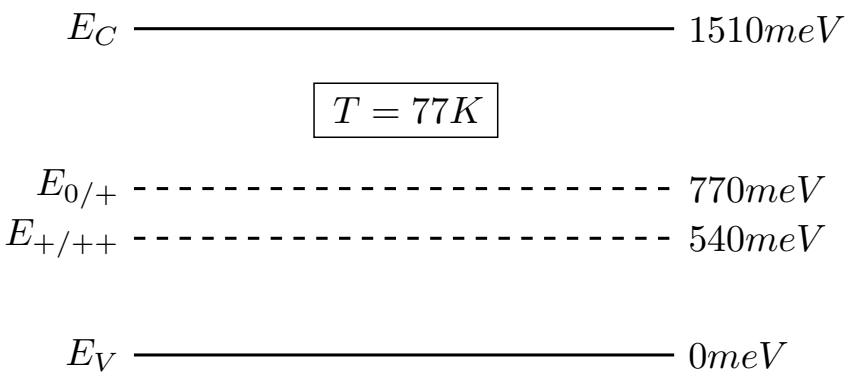

Figure 2.1: Both of the EL2 energy levels were measured by Lagowski et al. [1] in a single study involving DLTS and photocapacitance spectroscopy, and reported with $\pm 20meV$ precision. The authors specify that both levels are in relation to the valence band energy. I have calculated the band gap energy of $1510meV$ for $T = 77K$, and have included it here for reference. All energy levels are drawn to scale.

Isolated-As_{Ga} defects can be generated via neutron-transmutation doping (NTD), and using this method the As_{Ga} energy-levels were measured using photo-electron-paramagnetic-resonance (photo-EPR) [61]. Two energy levels were associated with As_{Ga} (at $E_C - 770meV$ and $E_V + 520meV$) in the NTD materials [61]; and these levels closely agree with those measured ($E_V + 770meV$[11] and $E_V + 540meV$) at T=77K using DLTS and photocapacitive (see Footnote 14) spectroscopy [1]. Lagowski et al. [1] strengthened the association between As_{Ga} and EL2 by measuring both ionization states of EL2, and also demonstrate that EL2 is neutral in n-GaAs, while positively charged in p-GaAs.

The scientific interests have largely been efforts to explain the observed metastability of the defect [24, 56, 62–64], while the technical importance comes from the role that EL2 plays in compensation mechanisms[12] [58] and in achieving reasonably high-mobility materials with subpicosecond lifetimes for fast photoconductive switching applications

[11] Using a T=77K bandgap of 1510meV, this corresponds to $E_C - 740meV$.

[12] The EL2 defect acts as a double donor, and is the defect that allows for semi-insulating GaAs (SI-GaAs) to be made without the addition of deep-level impurities. In SI-GaAs, EL2 compensates (captures) the native carbon acceptors, resulting in a low-carrier density ($\sim 10^6 cm^{-3}$) material while maintaining good mobility [58]. The mobility criteria of SI materials distinguishes them from high-resistivity materials with low-mobility and high carrier-density. SI-GaAs is used as the substrate for high-speed integrated circuits [25].

[65]. Gupta et al. [65] did not claim that EL2 was responsible for limiting the lifetime in their low growth-temperature (200°C) samples (LT-MBE-GaAs); however, Hall effect measurements [66] and infrared (IR) absorption [28] have been used to observe the two energy levels of EL2 ($E_C - 750meV$ and $E_V + 550meV$, respectively) in MBE-GaAs grown at 200°C. Both groups [28, 66] measured a defect density (associated with As_{Ga} by [28]) around $\sim 3 \times 10^{19} cm^{-3}$. The densities of EL2 observed in LT-MBE-GaAs [28, 66] are well above any possible residual impurity concentrations in the material, which further supports the conclusion that EL2 is an intrinsic defect.

As mentioned above, the EL2 defect is known to transition into a metastable state[13] when exposed to sub-bandgap (1.1-1.3eV) light below 140K, and this was observed through IR-absorption spectroscopy [29]. When EL2 is in its metastable state, its energy-levels change and the defect no longer compensates acceptors, and so this transition induced by sub-bandgap light is called photoquenching [25]. The metastability has also been observed from the photocapacitance[14] transient [67]. Using the IR-absorption technique [28] measured that only 10% (i.e. $\sim 3 \times 10^{18} cm^{-3}$) of the As_{Ga} defects in their samples undergo the photoquenching process and transition into a metastable state. This demonstrates that not all As_{Ga} is metastable, and that another defect (X) is required to give rise to the metastable nature.

Many theorists [24, 56, 62–64] have proposed EL2 models involving various complexes with As_{Ga} (i.e. attempts at identifying X); however, there are still inconsistencies between the models. While the magnetic-field dependence of the zero-phonon line

[13]This EL2 metastability refers to a crystallographic state, with electronic properties that correspond to the metastable configuration. The electronic properties of the metastable state of EL2 are not relevant to room-temperature operation, as the effect is only observed below 140K [29].

[14]Photocapacitance involves monitoring the change in capacitance that occurs when a Schottky diode is illuminated (initial conditions are dark). Prior to illumination, the Schottky diode is put into forward bias (to fill the traps) and then reverse bias [25]. Typically, the capacitance increases with illumination corresponding to the depletion-width reduction associated with the injection of photoionized excitons; however, the photoionizing illumination (1.2eV) also induces the transformation of EL2 into its metastable state (below 120K) and the photocapacitance is observed to decrease back to the dark value as the sample becomes transparent to the photo-excitation. Above 120K, the metastable transition cannot occur and the persistent 1.2eV absorption (via the defect-states) gives rise to a steady photocapacitance [67].

(ZPL) in the IR-absorption spectrum [64] suggested that EL2 is an isolated point defect with tetrahedral (T_d) symmetry (i.e. the As_{Ga} defect has As as its four nearest neighbours), the absence of metastability in NTD-generated As_{Ga} defects indicates that another defect must play a role in the actuation of the metastability transition [27]. Further problems with the isolated-As_{Ga} model of (photoquenchable) EL2 arose when early work [26] in optically-detected electron-nuclear resonance (ODENDOR) suggested that EL2=As_{Ga}+As_i in its stable state (supporting the model of Bardeleben et al. [56]); however, more recent work using ODENDOR[15] with better precision and higher-order theoretical interpretation has ruled out both EL2=As_{Ga}+As_i and isolated-As_{Ga} as hypothetical stable configurations of EL2 [59]. The symmetry was measured to deviate slightly from tetrahedral symmetry. The relatively modern results of [59] are quite significant, and confirm the growing consensus [24, 27, 28, 56, 61] that EL2 is more than an isolated-As_{Ga} (i.e. it involves another defect) while ruling out one of the models that has lead to much controversy [56, 68–71].[16] Knowing the (near-T_d) symmetry of EL2 in its stable state (see above), and also of the metastable state (see below) provides a powerful signature, and contributes to the identification of the EL2 complex by ruling out any hypothetical crystallographic models that violate this symmetry.

The metastable state of EL2 is difficult to probe without causing it to relax into its stable configuration, and it also leaves no signature in IR-absorption, EPR, or luminescence signals [25]. To probe the symmetry of EL2 in its metastable configuration, Trautman and Baranowski [72] demonstrated that the thermal recovery (near 130K) of stable EL2 (monitored with IR-absorption) is unaffected by stress applied in the [100] direction; however, stress in the [111] direction caused a splitting of the thermal recovery into two stages (one lower than 130K, one higher). If metastable-EL2 also

[15] Along with ODENDOR, optically-detected electron paramagnetic resonance (ODEPR) was also applied in [59].

[16] The initial ODENDOR results [26] that suggested EL2=As_{Ga}+As_i created much discussion in the community (see [25]), since it challenged the tetrahedral symmetry (and Isolated-As_{Ga} model for stable-EL2) suggested by experiments such as the ZPL dependence on magnetic-field strength [64].

had tetrahedral symmetry, this splitting would not be observed in any orientation. The combined splitting in the [111] direction and lack of splitting in the [100] direction [72] is only possible if EL2 is configured with trigonal symmetry (C_{3v}) in its metastable configuration.

An important theoretical contribution was given by Baraff and Schluter [24], where they used the Green's-function method to calculate the energy levels of the $As_{Ga}+V_{As} \rightleftharpoons V_{Ga}$ system. In their study, they solved the problem in a continuous sense where the As atom can be at any position between the As and Ga vacancies, and demonstrated that the compensation can be quenched as the As atom moves towards the V_{Ga} site and the donor levels fall below the valence band edge. While their (trigonally-symmetric) model [24] is not in accord with the near-tetrahedral symmetry suggested by ODENDOR and ODEPR [59], it provides an example of how these types of instabilities can be theoretically addressed in III-V materials.

A model proposed by Wager and Van Vechten [63, 71] involves As_{Ga} surrounded by four As-nearest-neighbours, and a divacancy (V_{Ga} and V_{As}). In the metastable state, As_{Ga} moves to fill the gallium vacancy, and its variation in properties is explained by the arsenic-vacancy nearest-neighbour. Their model is consistent with near-T_d-symmetry in the stable case (four As nearest-neighbours), and with C_{3v}-symmetry in the metastable case (with three As nearest-neighbours, and one V_{As}). A nearby vacancy is suggested as the subtle T_d-symmetry-breaking defect by [59], which suggests that this model is consistent with the most recent ODENDOR and ODEPR findings.[17] The concept that EL2 is a complex involving vacancies is supported by the $\sim 10^{16} - 10^{17} cm^{-3}$ vacancy densities measured in all types of GaAs using positron-annihilation measurements [71].

While the subtle nature of the metastability of EL2 (i.e. determining X, in EL2=As_{Ga}+X) is scientifically interesting; we are characterizing only the recombination-relevant defect parameters above the stable-EL2 thermal recovery temperature of

[17]Note that it was the original ODENDOR results that had challenged the model of [63], as it was one of the main experimental findings that were not explained by their model (see the relevant Comment [70] and Reply [71]).

140K[18] and so the electronic properties of the metastable-EL2 [9] are not relevant to this work. In fact below 140K, the injection of free electrons will recover the stable-EL2 configuration [63]. The electronic properties that are relevant to recombination are the energy levels, and the capture cross-sections for electrons and holes (σ_n and σ_p, respectively). The electron ($\sigma_n = (6 \times 10^{-15} e^{-66meV/k_BT}) cm^2$) and hole ($\sigma_p = 2 \times 10^{-18} cm^2$ at T=320K) cross-sections measured by Martin et al. using DLTS [54] have been reproduced by Prinz and Rechkunov [8] for 77-340K, which provides confidence in these parameters. The effect of strong electric fields (as present in depletion regions) on the cross-sections of defects in GaAs was also explored by [8], and they found that both the electron and hole cross-sections increase to $\sim 10^{-13} cm^2$ in a strong ($\sim 10 kV/cm$) electric field.

An early report by Miller et al. [30] suggested that EL2 was the lifetime-limiting defect.[19] This claim was based on the observation that both the defect-density (observed using DLTS) and the lifetime were correlated to stoichiometry. As the As/Ga ratio was increased during growth (from 1/3 to 3/1) the defect density increased (from $2 \times 10^{13} cm^{-3}$ to $9 \times 10^{13} cm^{-3}$), and the minority carrier lifetime decreased (from 15ns to 5ns). The findings that both the lifetime and the defect-density scaled by approximately the same factor is an indicator that EL2 may limit hole-lifetime in their undoped ($n_o \sim 6 \times 10^{15} cm^{-3}$) n-MOCVD-GaAs material. Mitonneau et al. [9] believed the findings of [30] to be accidental, as the hole-lifetime would be much too high at typical EL2 densities;[20] however, in light of the 5 to 6 order of magnitude increase in σ_p observed by [8], Miller et al. [30] could have been observing electric-field-enhanced EL2-mediated recombination in the depletion region of their junctions.[21] In a more

[18] In our samples, we are screened from the EL2 lifetime below 140K by radiative recombination.

[19] Note that [30] did not call the defect EL2, as the paper where the term was coined [54] was published during the same year; however, the variation with stoichiometry and the $E_C - 820meV$ energy-level measurement are consistent with EL2.

[20] Using a defect-density of $\sim 10^{14} cm^{-3}$, hole-capture cross-section of $\sigma_p \sim 10^{-18} cm^2$, and T=300K thermal velocity of 0.02cm/ns, one calculates (using (3.12)) a hole-lifetime of $500 \mu s$, which is 5 orders of magnitude higher than the lifetime observed by [30].

[21] The structure studied in [30] is a p-n junction, and the authors assert that the defect being characterized is in the n-type side of the junction.

recent study, Bourgoin and De Angelis found that the recombination current and EL2 density both varied by about three orders of magnitude between $p^+ - n$ junctions grown using CZ and MOCVD GaAs [31] and conclude that EL2 was the lifetime-limiting defect, and so it appears as though it may play a role in some depleted GaAs structures.

Chapter 3

Theoretical Background

3.1 Photoluminescence and Injection Level

Photoluminescence (PL) is the light emitted from a material in response to the absorption of optical excitation. The rate of emission of PL from a semiconductor depends on the injection level (η), which is the ratio (3.1) of excess (Δn) and equilibrium ($n_o + p_o$) carrier densities.

$$\eta = \frac{\Delta n}{n_o + p_o} \tag{3.1}$$

The emission rate is not linear with η, as it is proportional to the product of electron (n) and hole (p) densities [17]. $B(T)$ parametrizes the probability of a radiative recombination event occurring at a given n and p, and the net rate of radiative recombination (U_{rad}) is obtained by subtracting the thermal generation rate at equilibrium (where $np = n_i^2$, the squared intrinsic carrier density). The PL signal (I_{PL}) is proportional to U_{rad} and is given by (3.2), which is also expressed (3.2c) in terms of η.

$$I_{PL}(t) = A_{PL} \cdot B(T) \cdot (np - n_i^2) \tag{3.2a}$$

$$= A_{PL} \cdot B(T) \cdot (n_o + p_o + \Delta n) \cdot \Delta n \tag{3.2b}$$

$$= A_{PL} \cdot B(T) \cdot (n_o + p_o)^2 \cdot (1 + \eta) \cdot \eta \tag{3.2c}$$

While this equation is not new, I will demonstrate for the first time that by fitting TR-PLD (3.2c), the scaling coefficient $A_{PL}B(T)(n_o + p_o)^2$ can be decoupled from the initial injection level (η_o). Measurement of η_o from TR-PLD enables the measurement of $f(T)$ using the new model (3.26), which I will derive in Section 3.4.1. By measuring $A_{PL}B(T)(n_o + p_o)^2$, (3.2c) can rearranged to give $\eta(t)$, by solving the quadratic equation to obtain the injection-level decay (3.3).

$$\eta(t) = \sqrt{\frac{1}{4} + \frac{I_{PL}(t)}{A_{PL}(n_o + p_o)^2}} - \frac{1}{2} \tag{3.3}$$

3.2 Recombination Mechanisms

3.2.1 Radiative Recombination

Radiative recombination is typically modelled using the Van Roosbroeck and Shockley approach [73]; however, this model has been recently revisited [74] in order to address discrepancies between the predicted and measured rates of radiative recombination. In our situation, we do not need to predict the magnitude of the radiative lifetime (τ_r) and only require the temperature-dependence of the model.[1] In order to calculate the radiative recombination coefficient ($B(T)$), we need to solve the integral[2] (3.4) from

[1] I have not observed any freeze-out effects in our GaAs samples (i.e. the equilibrium carrier-density remains fixed with varied temperature), which is consistent with observations made by [75] on GaAs grown using MBE.

[2] This integral is derived in [74] from a generalization of Planck's law for non-thermal radiation by [76]. This is a momentum-conserving treatment that takes into account the presence of the energy

[74], in terms of the: photon energy (E), band-to-band absorption coefficient (α_{BB}), Planck constant ($\hbar$), speed of light (c), Boltzmann constant (k_B), and refractive index (n_{ref}).

$$B(T) = \frac{1}{n_i^2}\frac{1}{\pi^2\hbar^3c^2} \cdot \int_0^\infty n_{ref}^2 \cdot E^2 \cdot \alpha_{BB} \cdot e^{-E/k_BT}dE \tag{3.4}$$

Here, I neglect the temperature-dependence of n_{ref} and the bandgap (E_g), since they change slowly with temperature in relation to the effective densities of states ($N_C(T)$ and $N_V(T)$). This allows a first-order approximation to be made for the temperature dependence of τ_r. Under a Heaviside step-function assumption for α_{BB} (i.e. $\alpha_{BB} = U(E - E_g)$), the integral in (3.4) gives a factor proportional to $k_BTE_g^2e^{-E_g/k_BT}$. Expanding n_i in terms of the effective densities of states (i.e. $n_i^2 = N_C(T) \cdot N_V(T)e^{-Eg/k_BT}$), I have derived a new first-order approximation (3.5) for how τ_r changes with temperature.[3] Note that $N_{D/A}$ is the donor/acceptor density.

$$\tau_r = \frac{1}{B(T)N_{D/A}} = \frac{C_r \cdot N_C(T) \cdot N_V(T)}{T} \tag{3.5}$$

In GaAs at temperatures below 300K, the densities of states can be approximated (with less than 7% error)[4] using the parabolic-band approximation, yielding (3.6). For other semiconductors the parabolic band-approximation may be true at even higher temperatures, and (3.6) provides a simple model for fitting τ_r in these types of systems.

$$\tau_r = A_rT^2 \tag{3.6}$$

The parabolic-band approximation breaks down in GaAs above 300K, and a more accurate approximation is given by (3.7). See (C.1) for how I have approximated $N_{C/V}$

gap (E_g).

[3] I have absorbed all slowly changing factors (n_{ref}^2 and E_g^2) into a single scaling factor (A_r). A second-order modification to this model would be to include an exponential factor; however, I have observed no evidence of this in fitting experimental data.

[4] The error is less than 7% for temperatures below 300K, and less than 0.25% below 200K, as calculated using (C.1).

in GaAs. Using this new model (3.7) for τ_r in GaAs,[5] I will demonstrate that $f(T)$ can be measured from fits to τ_{bulk}.

$$\tau_r = A_r(1 + 52.39e^{-171.5\text{meV}/k_BT})T^2 \tag{3.7}$$

3.2.2 Defect-Assisted Nonradiative Recombination

I have modelled nonradiative recombination via defect energy-levels using the Shockley-Read-Hall (SRH) approach [35]. In the case of GaAs, defect-assisted recombination typically occurs via the multi-phonon emission (MPE) capture mechanism [9, 11, 39], where defects undergo an exponential increase in their carrier cross-section ($\sigma_{n/p}$) as temperature is increased, parametrized by E_∞.

$$\begin{aligned}\sigma_{n/p} &= \sigma_o + \sigma_\infty e^{-E_\infty/k_BT} \\ &= \sigma_o\left(1 + r_\sigma e^{-E_\infty/k_BT}\right)\end{aligned} \tag{3.8}$$

Defects that behave according to MPE-capture have similar values of σ_∞ (in the range of $(10^{-16} \leftrightarrow 10^{-14})cm^2$ in GaAs, [9, 11]), and so the shape of the cross-section (parametrized by E_∞ and the ratio of cross-sections: $r_\sigma \equiv \sigma_\infty/\sigma_o$) provides information about the lifetime-limiting defect that can allow for its identification (see the distinct DLTS-measured shapes of σ_n and σ_p in [8, 9, 11, 25]). The SRH-lifetime (τ_{SRH}) is a function (3.9) of η. Note the asymptotic behaviour of τ_{SRH}, where it approaches constant values (τ_{LLI} and τ_{HLI}) in the low-level injection (LLI) and high-level injection (HLI) regimes [17, 35].

$$\tau_{SRH} = \frac{\tau_{LLI} + \tau_{HLI}\cdot\eta}{1+\eta} \xrightarrow[\text{Levels}]{\text{Deep}} \tau_{min} + \left(\frac{\eta}{1+\eta}\right)\tau_{maj} \tag{3.9}$$

[5]The numerical coefficients have been optimized for 77-700K; however, the approach outlined in Appendix C of approximating $N_{C/V}$ can be applied over a broader temperature range to provide optimal coefficients for fitting with (3.7) using higher temperature.

For most deep levels [35], τ_{SRH} simplifies to give the minority-carrier lifetime (τ_{min}) in the LLI regime (i.e. $\tau_{LLI} \xrightarrow[\text{Levels}]{\text{Deep}} \tau_{min}$), and the sum of carrier lifetimes in the HLI regime ($\tau_{HLI} \xrightarrow[\text{Levels}]{\text{Deep}} \tau_{min} + \tau_{maj}$). The electron/hole lifetime ($\tau_{n/p}$) is inversely proportional (3.10) to the total trap density (N_t), the thermal velocity ($v_{th} = \sqrt{3k_BT/m^*}$, where m^* is the electron/hole effective mass) and the capture-cross section for electrons/holes ($\sigma_{n/p}$) defined in (3.8).

$$\tau_{n/p} = \frac{1}{N_t \sigma_{n/p} v_{th}} \tag{3.10}$$

Substituting the effective masses[6] for electrons and holes in GaAs, we get (3.11a) and (3.11b), respectively.

$$\tau_n = \frac{0.251}{N_t \sigma_n} \sqrt{\frac{m_o}{3k_BT}} = \frac{(645 ns K^{1/2} cm^{-1})}{N_t \sigma_n \sqrt{T}} \tag{3.11a}$$

$$\tau_p = \frac{0.198}{N_t \sigma_p} \sqrt{\frac{m_o}{3k_BT}} = \frac{(509 ns K^{1/2} cm^{-1})}{N_t \sigma_p \sqrt{T}} \tag{3.11b}$$

At sufficiently high-temperatures, the lifetime undergoes an Arrhenius increase due to thermal deactivation of the dominant defect. I have taken this into account with (3.12), where the T dependence corrects for the density of states of the unknown band, under the parabolic-band approximation [17].

$$\tau_{\text{nr}} = \tau_{n/p} + C_{nr} T e^{-E_a/k_BT} \tag{3.12}$$

In (3.12), the Arrhenius increase is parametrized by the activation energy (E_a); however, this is not equal to the defect energy-level depth (ΔE_t) as it is unknown

[6] In GaAs, there is a heavy- and light-hole band with $m_{lh} = 0.076 m_o$ and $m_{hh} = 0.50 m_o$, respectively (where m_o is the free electron rest-mass). The electron effective-mass used is $m_e = 0.063 m_o$ [77]. Assuming that recombination for light- and heavy-holes occurs in parallel and with the same capture cross-sections (direct transitions are near $k \approx 0$), the minority carrier lifetime must take this into account. This gives $\tau_p^{-1} = \tau_{\ell h}^{-1} + \tau_{hh}^{-1} = \sigma_p N_t \sqrt{3k_BT}(m_{\ell h}^{-1/2} + m_{hh}^{-1/2})$, and $\tau_p = \frac{0.198}{\sigma_p N_t}\sqrt{\frac{m_o}{3k_BT}}$ used in fitting.

whether the Arrhenius increase is caused by increase in electron (lower band-half defect) or hole (upper band-half defect) lifetimes [17]. This leaves two possible conclusions, either: $\Delta E_t = E_a + (E_\infty)_n$ (lower band-half) or $\Delta E_t = E_a + (E_\infty)_p$ (upper band-half).

3.2.3 Bulk Recombination and Radiative Efficiency

The bulk lifetime ($\tau_{bulk} \equiv \Delta n / U_{\text{total}}$) characterizes the total recombination rate (U_{total}) via radiative (U_{r}) and nonradiative (U_{nr}) pathways in the material. Since recombination rates add ($U_{\text{total}} = U_{\text{r}} + U_{\text{nr}}$), the bulk lifetime is given by (3.13). For GaAs,[7] (3.13) can be used with (3.7) and (3.11) to fit temperature-dependent lifetime data.

$$\frac{1}{\tau_{bulk}} = \frac{1}{\tau_r} + \frac{1}{\tau_{nr}} \tag{3.13}$$

$f(T)$ is the fraction (3.14) of all recombination that is radiative, and it can be measured by fitting temperature dependent τ_{bulk} with (3.13) using (3.7) and (3.11).

$$f(T) = \frac{U_{\text{rad}}}{U_{\text{total}}} = \frac{\tau_{bulk}}{\tau_r} = \frac{1}{1 + \tau_r/\tau_{nr}} \tag{3.14}$$

3.2.4 Intrinsic Nonradiative Recombination

Auger recombination (the inverse of impact ionization) is where the energy of recombination is transferred to the excess kinetic energy of an electron or hole. The Auger lifetime (τ_A) under HLI conditions is inversely proportional (3.15) to the squared excess carrier density via the ambipolar Auger coefficient (C_a), [17]. At room temperature (300K), C_a has been measured to be $7 \times 10^{-30} cm^6/s$, [78].

$$\tau_A^{HLI} = \frac{1}{C_a \Delta n^2} \tag{3.15}$$

From the experiments in [78], it was found that the Auger effect is insignificant for carrier densities below $10^{19} cm^{-3}$, and so we expect no influence of Auger recombination

[7] For any material, (3.5) or (3.6) can be used in place of the GaAs-specific (3.7).

in the CZ-GaAs sample. When our laser is operating at maximum pulse-energy, maximum carrier densities of about $10^{17} cm^{-3}$ are produced. Under these conditions, an initial τ_A^{HLI} of $14\mu s$ is expected in our HLI experiments with lightly doped MBE-GaAs films. As a result, the Auger lifetime is not expected to have a significant influence on the nanosecond-scale τ_{bulk} in any of our experiments.

3.3 Diffusion and Surface Recombination

3.3.1 Thick Materials: Solution to Diffusion Equation in Cylindrical Coordinates

In TR-PLD experiments on thick materials, diffusion and surface recombination can bias the measurement of τ_{bulk}. Following excitation, electrons and holes diffuse away from the surface following the initial laser-excitation. Since both carriers travel in the same direction, we must use the ambipolar diffusivity to account for the Coulombic attraction between the two charge-types during diffusion. The diffusion equation has been solved for the semi-infinite slab in one dimension by Vaitkus [3], and I have generalized this solution to three-dimensions in cylindrical coordinates (3.16).

$$\begin{aligned}
\Delta n &= A_{diff} \cdot R(\rho,t) \cdot Z(z,t) \cdot e^{-t/\tau_{bulk}} \\
A_{diff} &= \frac{\alpha N_T}{2\pi\sigma_\rho^2} \\
R(\rho,t) &= \frac{e^{-\rho^2/\left[2\sigma_\rho^2(1+t/\tau_\rho)\right]}}{1+t/\tau_\rho} \\
Z(z,t) &= e^{-(\alpha z)^2\tau_z/4t} \cdot (B_z(z,t) - C_z(z,t)) \\
B_z(z,t) &= \frac{1}{2}\left(\frac{\sqrt{\tau_{FS}}+\sqrt{\tau_z}}{\sqrt{\tau_{FS}}-\sqrt{\tau_z}}\text{erfce}\left(\sqrt{\frac{t}{\tau_z}}+\frac{\alpha z}{2}\sqrt{\frac{\tau_z}{t}}\right) + \text{erfce}\left(\sqrt{\frac{t}{\tau_z}}-\frac{\alpha z}{2}\sqrt{\frac{\tau_z}{t}}\right)\right) \\
C_z(z,t) &= \frac{\sqrt{\tau_z}}{\sqrt{\tau_{FS}}-\sqrt{\tau_z}}\text{erfce}\left(\sqrt{\frac{t}{\tau_{FS}}}+\frac{\alpha z}{2}\sqrt{\frac{\tau_z}{t}}\right)
\end{aligned} \tag{3.16}$$

Time constants of (3.16) associated with front-surface loss (FS), axial (z) diffusion, radial (ρ) diffusion, and transit-time (tr) are defined in (3.17). This solution is valid for $\tau_{bulk} \ll \tau_{tr}$. τ_{tr} can be thought of as the transit time constant for some thickness, W. This model is applicable for thicknesses of $W \gg \pi L_D$, where $L_D \equiv \sqrt{D_a \tau_{bulk}}$ is the diffusion length; however, I have extended its application to thinner materials ($W \sim L_D$) using a piecewise approximation with the Sproul [4] model, as discussed further in Section 3.3.2.

$$\tau_{FS} = \frac{D_a}{S^2}; \qquad \tau_z = \frac{1}{\alpha^2 D_a}; \qquad \tau_\rho = \frac{\sigma_\rho^2}{2D_a}; \qquad \tau_{tr} = \frac{(W/\pi)^2}{D_a} \tag{3.17}$$

The exponentially scaled complementary error function ($\mathrm{erfce}(x)$) in (3.16) is defined in (3.18) along with its asymptotic approximation.

$$\mathrm{erfce}(x) = e^{x^2}\mathrm{erfc}(x) \xrightarrow{x\to\infty} \frac{1}{x\sqrt{\pi}} \tag{3.18}$$

Using defocused excitation, we can establish conditions where $\tau \ll \tau_\rho$, which recovers the one-dimensional solution of Vaitkus [3]. By assuming a deep collection volume (in relation to the diffusion length, $\sqrt{D_a \tau_{bulk}}$), in the low-level injection regime where the excess carrier density is far below the equilibrium carrier density, the PL signal is proportional to the integral of the carrier density. This integral has an analytic solution (3.19) that was found by Vaitkus [3] and applied by Ahrenkiel et al. [79], where $C \propto N_T / 2\pi\sigma_\rho^2$ and the proportionality depends on the optical throughput of the apparatus, and number of experiment repetitions.

$$I_{PL} = C\left(\frac{\sqrt{\tau_z}\mathrm{erfce}\sqrt{t/\tau_z} - \sqrt{\tau_{FS}}\mathrm{erfce}\sqrt{t/\tau_{FS}}}{\sqrt{\tau_z} - \sqrt{\tau_{FS}}}\right) e^{-t/\tau_{bulk}} \tag{3.19}$$

I have characterized the asymptotic approximation for the exponentially scaled error function (3.18), and found that it has less than 1% relative error for $x \geq 7$ (the error continues to decrease as $x \to \infty$). Using (3.18), (3.19) simplifies for $\tau_{bulk} \gg \tau_z$ and $\tau_{bulk} \gg \tau_{FS}$ to give (3.20). This was originally proposed for $t > \tau_{bulk}$ by Ahrenkiel

et al. [79]; however, the applicability under strong absorption and surface-loss was not proposed. Here, we present explicit conditions ($\{\tau_z, \tau_{FS}\} \ll \tau_{bulk} \ll \{\tau_\rho, \tau_{tr}\}$) for which there is less than a 1% error associated with the use of this approximation (3.20), and prove that the approximation can be valid for $t \ll \tau_{bulk}$ as well. Note that the surface recombination velocity, diffusivity, and absorptivity have all become coupled in the scaling factor, $A \equiv C(\sqrt{\tau_z} + \sqrt{\tau_{FS}})/\sqrt{\pi}$, and cannot be resolved in this limit.

$$I_{PL} = A\frac{e^{-t/\tau_{bulk}}}{\sqrt{t}} \tag{3.20}$$

A good measure of the losses associated with a particular surface recombination velocity is the fraction of carriers lost to the surface. This fraction depends also on how strongly absorbed the excitation is. From (3.16), I have calculated the flux across the front surface, and integrated to obtain an analytical expression (3.21) for the fraction of carriers lost to front surface recombination, f_{loss}. Knowing the dependence of f_{loss} on absorption strength, surface-loss, bulk lifetime, and diffusivity provides deeper insight into front-surface losses in photodetectors and solar-cells.

$$f_{loss} = \frac{1}{\left(1 + \sqrt{\tau_z/\tau_{bulk}}\right)\left(1 + \sqrt{\tau_{FS}/\tau_{bulk}}\right)} \tag{3.21}$$

If focused excitation is used, and the lifetimes are sufficiently long, then linearization for highly focused excitation may be possible. For example, with a spot size of $\sigma_\rho \approx 1\mu m$ and $D_a \approx 20 cm^2/s$ [5], we calculate $\tau_\rho \approx 500 ps$. This leads to another approximation for maximally focused light, where radial diffusion can be accounted for by division of the signal by t. In this case, the shape of the signal becomes independent of the radial characteristics of the beam, as these parameters become absorbed into the scaling factor.

3.3.2 Thin Films: Unification of the Models of Vaitkus, Sproul, and Luke & Cheng

A closed-form solution has not yet been found for the two-surface case of the diffusion problem; however, Luke and Cheng [2] have found a series-solution. I have found that under typical experimental circumstances (i.e. values of α, and W), the model of Luke and Cheng (as well as the numerical solution to the diffusion equation) can be approximated at early times ($t < \tau_S/2$) by the Vaitkus [3] model (see (3.19) in Section 3.3.1), and by the Sproul effective-lifetime model [4] at later times. In fact, I have found that the Vaitkus [3] and Sproul [4] models provide a piecewise approximation of the true two-surface solution (e.g. [2]) if they are joined at the point where the derivative[8] of (3.19) is equal to the derivative of the monoexponential decay described by Sproul [4] (where the effective lifetime has been found for various cases of surface passivation). This can be calculated analytically for the unpassivated case, yielding a piecewise approximation (implicitly found to be valid for unpassivated samples with $W \geq 10\mu m$ and $\alpha \geq 8\mu m^{-1}$) given by (3.22a) in terms of the effective two-surface lifetime (3.22b) of Sproul [4]. Note that e is Euler's number here (3.22a) and *not* the elementary charge.

$$I_{PL} = Ae^{-t/\tau_{bulk}} \cdot \begin{cases} \frac{1}{\sqrt{t}} & t < \frac{\tau_S}{2} \\ \sqrt{\frac{2e}{\tau_S}} \cdot e^{-t/\tau_S} & t > \frac{\tau_S}{2} \end{cases} \tag{3.22a}$$

$$\tau_S = \frac{W}{2S} + \frac{(W/\pi)^2}{D_a} = \frac{W}{2S} + \tau_{tr} \tag{3.22b}$$

In the thin ($< 10\mu m$) case, the actual S becomes more influential (even in unpassivated samples) and the full Vaitkus model (3.19) is required to model the early decay. In this case (and for thicker materials with any S), the Vaitkus model (3.19) should

[8] This condition makes sense at a physical level as the lifetime is inversely proportional to the derivative of the excess carrier density, which is equivalent to assuming a continuous lifetime.

be patched with the Sproul [4] model at the time obtained by numerically solving the transcendental condition (3.23) for continuous derivative.

$$\sqrt{\tau_z}\left(\frac{1}{\tau_z}+\frac{1}{\tau_S}\right)\operatorname{erfce}\sqrt{\frac{t}{\tau_z}}=\sqrt{\tau_{FS}}\left(\frac{1}{\tau_{FS}}+\frac{1}{\tau_S}\right)\operatorname{erfce}\sqrt{\frac{t}{\tau_{FS}}} \tag{3.23}$$

With Monte-Carlo simulations using the Luke and Cheng [2] solution, I have found that (3.22) (and the approach using (3.23)) can be used to accurately fit TR-PLD. Fig. 3.1 shows the piecewise approximation (3.22) to the Luke and Cheng model, and demonstrates that accurate τ_{bulk} can be obtained up to about $1\mu s$ in unpassivated $100\mu m$ GaAs.

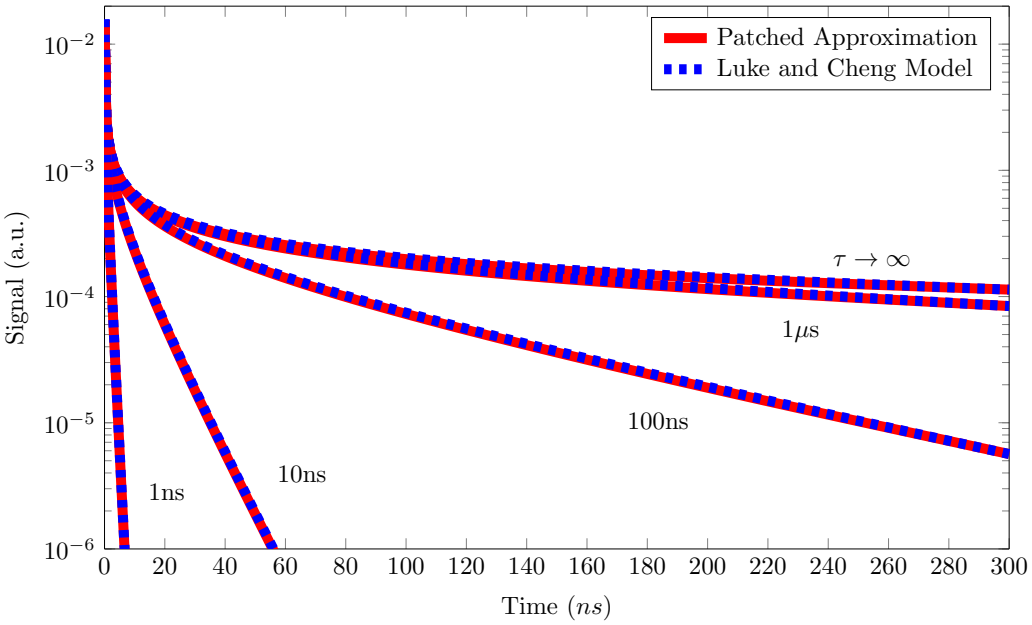

Figure 3.1: Piecewise approximation to the model of Luke and Cheng [2], comprised of a continuous derivative patching of the Vaitkus [3] model at early times, and the Sproul [4] model at later times. In this T=300K simulation of an unpassivated $100\mu m$ GaAs layer, $D_a = 20cm^2/s$ [5], $\alpha = 8\mu m^{-1}$ [6], and $S = 10^6 cm/s$.

The consistency of the unified models of Vaitkus and Sproul with the more general model of Luke and Cheng provides deeper insight into surface recombination in photodetectors and solar cells, and demonstrates that there is generally an abrupt transition (3.23) between the one- and two-surface behaviour.

3.4 Injection Level Variation

I have found experimentally that the measurement of the low-level injection (LLI) lifetime is screened by the emission of carriers from localized trap states at low laser pulse-energy (E_p); however, at high-E_p quasi-equilibrium is quickly reached and sustained, allowing for observation of the band-to-band dynamics. These two regimes occur when the dominant shallow localized states (parametrized by an effective energy depth, E_ℓ) in the minority band-half are either mostly empty or mostly full. Experimentally, I have also observed that τ_{nr} does not change significantly with variation of E_p in the n- and p-type MBE-GaAs DHs. First, I will derive (3.26) for use in the trap-saturated high-level injection (HLI) regime,[9] then (3.35) and (3.32) to use in the trapping dominated low-E_p (and in our case also LLI) regime.

3.4.1 High-Level Injection

I have found useful expressions for modelling recombination in direct bandgap materials where the τ_r and τ_{nr} are comparable. In the diffusion- and drift-free case where radiative and nonradiative (SRH model) recombination are competitive, the continuity equation (3.24) constrains decay of injection level following optical excitation.

$$\frac{d\eta}{dt} = -\left(\frac{1+\eta}{\tau_r} + \frac{1+\eta}{\tau_{LLI}+\tau_{HLI}\eta}\right)\eta \tag{3.24}$$

Using the method of partial fractions, I have solved (3.24) and obtained the implicit time-dependence of the carrier density (3.25) in terms of the LLI bulk lifetime ($\tau_{bulk} \equiv \tau_r||\tau_{LLI}$), the initial injection level (η_o), the ratio of HLI and LLI lifetimes ($r \equiv \tau_{HLI}/\tau_{LLI}$), and the radiative efficiency ($f \equiv \tau_{bulk}/\tau_r$).

[9] In Appendix A, I discuss an analytical model that I have derived to describe the injection-level dependence of the surface recombination velocity, in order to explore the possibility of extraction of these parameters from decay measurements with varied E_p.

$$-\frac{t}{\tau_{bulk}} = \ln\left(\frac{\eta}{\eta_o}\right) - \left(\frac{1-r}{1-rf}\right)\ln\left(\frac{1+\eta}{1+\eta_o}\right) - r\left(\frac{1-f}{1-rf}\right)\ln\left(\frac{1+rf\eta}{1+rf\eta_o}\right) \quad (3.25)$$

While (3.25) cannot be inverted, I have found a new approximate inversion (3.26) valid for all η in the case where $\tau_{LLI} \approx \tau_{HLI}$ (or for low doping-level where TR-PLD is entirely in HLI regime) and another new approximate inversion (3.27) valid (from $0 \leq \eta \leq 0.1$) for all τ_{LLI} and τ_{HLI}. The former case (3.26) is useful for low doping (sufficient that $\tau_{nr} \approx \tau_{HLI}$ throughout the TR-PLD), as well as a common class of deep-level defects described below. The latter case (3.27) should provide measurement of both τ_{HLI} and τ_{LLI} in systems where $\eta(t=0) \sim 0.1$ and $\tau_{HLI} \gg \tau_{LLI}$.

When nonradiative recombination occurs primarily via a deep-level, the LLI-lifetime is (to a very good[10] approximation) equal to the minority-carrier lifetime ($\tau_{LLI} = \tau_{min}$). For all levels, the HLI-lifetime is equal[11] to the sum of minority and majority lifetimes ($\tau_{HLI} = \tau_{min} + \tau_{maj}$). In the case where $\tau_{min} \gg \tau_{maj}$, decay is limited by minority-carrier capture through the entire decay ($\tau_{LLI} \approx \tau_{HLI}$). I have solved (3.24) to obtain an analytic solution (3.26) that is valid when the variation in τ_{nr} is sufficiently small (such that $\left|\frac{\Delta\tau_{nr}}{\tau_{nr}}\right| \ll \frac{\tau_{nr}}{\tau_r}$). This equation (3.26) is also valid if the entire decay is in the HLI, due to sufficiently low doping-level.

$$\eta(t) = \frac{\eta_o e^{-t/\tau_{bulk}}}{1 + \eta_o f(T)\left(1 - e^{-t/\tau_{bulk}}\right)} \quad (3.26)$$

Using (3.26) substituted into (3.2c), TR-PLD can be fit to yield estimates of τ_{bulk}, initial injection level (η_o) and $f(T)$. By substitution of τ_{bulk} (3.13) and $f(T)$ (3.14) into $\eta(t)$ (3.26) and then into $I_{PL}(t)$ (3.2c), TD-TR-PLD data can be fit with a surface to enforce consistency between time and temperature modelling.

[10] Use caution with this approximation when studying very lightly doped materials (where $N_C/n_o \gg 1$ or $N_V/p_o \gg 1$). See [17] for an in depth discussion about the SRH model.

[11] This equality ($\tau_{HLI} = \tau_{min} + \tau_{maj}$) is only true at temperatures below the Arrhenius onset temperature [17], which has been the case for in nearly all of our experiments (except for the small Arrhenius influence observed in the 550-700K temperature-range, see Fig. 5.26).

For the $\eta \leq 0.1$ case, I have found a first-order approximation (3.27) using the Lambert-W function ($W[\ ]$) that has less than 5% error for $\eta \leq 0.1$ in the defect-limited case ($f \to 0$, or $\{\tau_{LLI}, \tau_{HLI}\} \ll \tau_r$).

$$\eta(t) = \frac{1}{\gamma} W\left[\gamma(1+\eta_o)^{\gamma}\eta_o e^{-t/\tau_{bulk}}\right] \tag{3.27}$$

Where γ is a function (3.28) of the HLI and LLI lifetimes (τ_{HLI} and τ_{LLI}).

$$\gamma = \frac{\tau_{HLI}}{\tau_{LLI}} - 1 \tag{3.28}$$

The Lambert-W solution (3.27) is particularly effective in handling nonlinearity in cases where $\tau_{HLI} > \tau_{LLI}$ (which is always true for deep levels below the onset temperature of the Arrhenius increase [17]),[12] since it can take a long time to decay even at low injection levels below $\eta \sim 0.1$.

3.4.2 Trapping

Small-perturbation (low-E_p) approaches to measuring the LLI lifetime (especially in compound semiconductors, like GaAs [80]) often give rise to large and unpredictable systematic error associated with the screening of the decay process by trap-emission [17]. The emission of minority carriers from traps following excitation give rise to long-lived, monoexponential signals;[13] however, the time-constant measured in this regime has little to do with the recombination dynamics in the material. I will also show that high-E_p measurements can be used to ensure quasi-equilibrium between extended and localized states, providing decay that accurately reflects τ_{bulk} when fit with (3.26) and (3.2c).[14] It is easier to account for the nonlinearity associated with HLI effects, than it is to attempt to gauge the degree of contribution of trap-emission

[12] It is true that $\tau_{HLI} > \tau_{LLI}$ for deep levels; however, when the minority-carrier lifetime is much longer than the majority-carrier lifetime, the lifetime is approximately constant ($\tau_{HLI} \approx \tau_{LLI}$).

[13] See the background signals in low-E_p results from Figs. 5.14 and 5.15

[14] Careful biasing with sub-bandgap light has been shown [17] to minimize the systematic error. QSSPL is another approach that is less prone to trap screening [41].

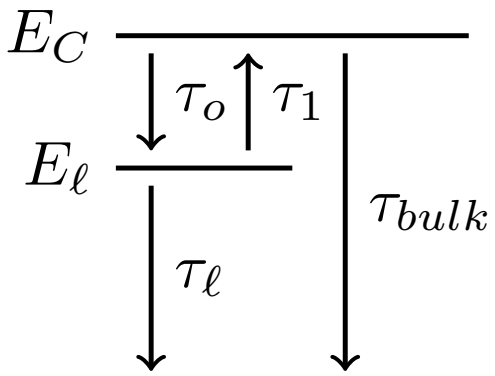

Figure 3.2: Definition of trapping time constants, with p-type example. Band to band recombination (τ_{bulk}), trap-capture (τ_o), trap-emission (τ_1) and trap-decay (τ_ℓ) were taken into account.

to the slope measured from a signal.

In this section, I derive a new analytical solution to the continuity equation (3.29) under non-equilibrium conditions for the one-level system depicted in Fig. 3.2, where p-type is used as an example.[15] This new model illustrates how τ_{bulk} becomes coupled with trap-capture (τ_o), trap-emission (τ_1), and trap-decay (τ_ℓ) time-constants, allowing for meaningful characterization of trapping dynamics from low-E_p TR-PLD.

$$\frac{d\Delta n}{dt} = \frac{\rho_1}{\tau_o} f_\ell - \left(\frac{1 - f_\ell}{\tau_o} + \frac{1}{\tau_{bulk}} \right) \Delta n \tag{3.29a}$$

$$= \left(\frac{\rho_1 + \Delta n}{\tau_o} \right) f_\ell - \frac{\Delta n}{\tau_o || \tau_{bulk}} \tag{3.29b}$$

$$= \left(\frac{f_\ell - f_Q}{\tau_o} \right) (\rho_1 + \Delta n) - \frac{\Delta n}{\tau_{bulk}} \tag{3.29c}$$

In (3.29), I have adopted the n_1 and p_1 notation from the SRH approach [35], using a single generalized minority-carrier variable (ρ_1) defined in (3.30).

[15] Thermal excitation from the valence band is neglected.

$$\rho_1 = \begin{cases} N_C e^{-(E_C - E_\ell)/k_B T} & \text{p-type} \\ N_V e^{-(E_\ell - E_V)/k_B T} & \text{n-type} \end{cases} \tag{3.30}$$

Also in (3.29), f_ℓ is the fraction of occupied shallow levels, and f_Q is the fraction occupied at quasi-equilibrium. Fermi-Dirac statistics (3.31) determine f_Q of a shallow level at E_ℓ, and can be rewritten in terms of Δn and ρ_1.

$$f_Q \equiv \frac{\Delta n}{\rho_1 + \Delta n} \tag{3.31}$$

The trap-capture lifetime is inversely proportional ($\tau_o = (\sigma_\ell v_{th} N_\ell)^{-1}$) to the localized-state density (N_ℓ) and the thermal velocity (v_{th}) via the trap minority-carrier-capture cross-section (σ_ℓ). The trap-emission lifetime is given by $\tau_1 = (\sigma v \rho_1)^{-1}$ based on the detailed-balance approach of assuming for the quasi-equilibrium conditions [17].

When low E_p is used, three time-domains are observed (Stages, I, II, and III) as shown in Fig. 3.3. Early transients associated with deep-level filling are observed before quasi-equilibrium is reached between extended and localized states (Stage I). Once quasi-equilibrium has been established (Stage II), the capture and emission processes from the trap balance out (3.29c) and decay follows τ_{bulk}. Following Stage II, there is a long-lived trap-emission process (Stage III) that occurs once the minority-carrier quasi-Fermi level (E_F^n) has fallen below the quasi-Fermi level of the localized state (E_F^ℓ) where quasi-equilibrium no longer exists between extended and localized states.

To model Stage I as well as the initial filling of deep-levels, I have assumed an exponentially saturating lifetime at early times. Under these assumptions, I have derived a new model (3.32), where $\tau_\times$ parametrizes the rate of the exponential saturation in early lifetime, δ corresponds to the relative change in the lifetime, and τ_t will be defined in (3.35).

$$I_{tr} = \left(1 + \delta\left(1 - e^{-t/\tau_\times}\right)\right)^{-\tau_\times/\tau_t} \tag{3.32}$$

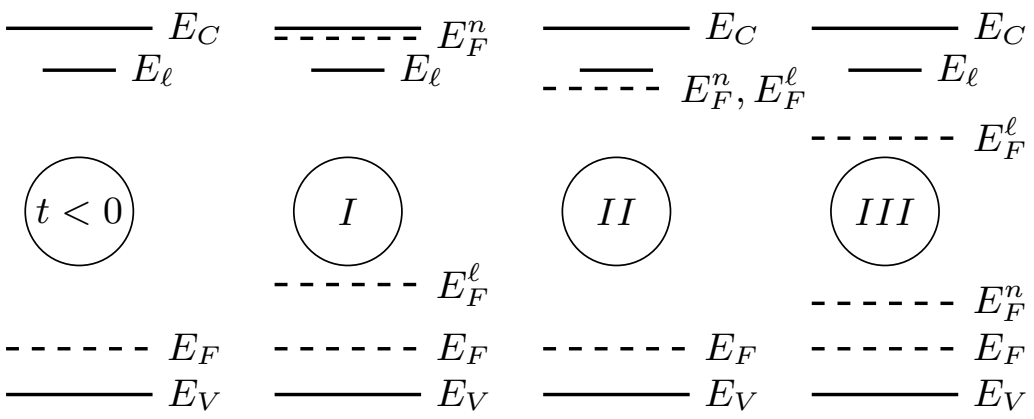

Figure 3.3: Energy levels (p-type example) for equilibrium ($t < 0$), and before, at, and after (I, II, and III) quasi-equilibrium (between E_C and E_ℓ). Subscripts indicate conduction band (C), valence band (V), effective localized energy level (ℓ), and Fermi level (F). Superscripts indicate a quasi-Fermi level for free (n) and trapped (ℓ) electrons. E_ℓ, E_F, and E_F^n are drawn to scale for: the measured $E_\ell = E_C - 160meV$, $E_F = 175meV$ for $10^{16}cm^{-3}$ doping ($300K$), and $E_F^n = E_C - 38meV$ for the measured $\Delta n_o = 10^{17}cm^{-3}$ at $E_p = 4\mu J$.

To model Stages II and III, I have derived an analytical solution to the diffusion- and drift-free continuity equation (3.29), in the limit where shallow levels are mostly empty. Mathematically, this corresponds to $\Delta n \ll \rho_1$. When the minority band is in quasi-equilibrium with its shallow levels (Stage II), both are populated according to Fermi-Dirac statistics parametrized by a common minority carrier quasi-Fermi level (i.e $E_F^n = E_F^\ell$). In general (and also when $\Delta n \gg \rho_1$), (3.29) is nonlinear[16] with no general solution [81]; however, however for trap-dominated conditions where most traps are empty ($\Delta n \ll \rho_1$), (3.29b) linearizes (with $\tau_1 = (\sigma v \rho_1)^{-1}$), and yields (3.33).

$$\lim_{\frac{\Delta n}{\rho_1} \to 0} \frac{d\Delta n}{dt} = \frac{N_\ell f_\ell}{\tau_1} - \frac{\Delta n}{\tau_o || \tau_{bulk}} \tag{3.33}$$

I have also taken the decay from the shallow states directly to the valence band into account, and characterized these transitions by a constant effective lifetime (τ_ℓ). Since we are dealing with doped materials, the equilibrium values of minority-carrier-density

[16]While the equation is still nonlinear, we observe TR-PLD with τ_{bulk} because $f_\ell \approx f_Q$ throughout the $\Delta n \gg \rho_1$ portion of the decay (Stage II).

and trap occupation can be neglected and Δn can be written (3.34) in terms of the initial minority-carrier-density (Δn_o), the density of occupied shallow traps ($N_\ell f_\ell$), and the total Δn lost via band-to-band ($\int_0^t(\Delta n/\tau_{bulk})dt$) and trap-assisted ($\int_0^t(N_\ell f_\ell/\tau_\ell)dt$) decay.

$$\Delta n = \Delta n_o - N_\ell f_\ell - \int_0^t \left(\frac{\Delta n}{\tau_{bulk}}\right) dt - \int_0^t \left(\frac{N_\ell f_\ell}{\tau_\ell}\right) dt \tag{3.34}$$

By taking the time-derivative of (3.34) and substituting $N_\ell f_\ell$ from (3.33), I have obtained a second-order, constant-coefficient, linear, ordinary differential equation and its analytical solution (3.35). Included in this new model (3.35) is the time dependence (I_{tr}, (3.32)) introduced by the filling of deep levels, which is discussed further below.

$$\begin{aligned}
\frac{\Delta n}{\Delta n_o} &= I_{tr} e^{-t/2\tau_t} \left(\cosh\left(\frac{\beta t}{2\tau_t}\right) + \frac{\alpha}{\beta}\sinh\left(\frac{\beta t}{2\tau_t}\right)\right) \\
\frac{1}{\tau_t} &= \frac{1}{\tau_o||\tau_{bulk}} + \frac{1}{\tau_1||\tau_\ell} \\
\beta &= \sqrt{1 - 4\tau_t^2\left(\frac{1}{(\tau_o||\tau_{bulk})(\tau_1||\tau_\ell)} - \frac{1}{\tau_o\tau_1}\right)} \\
\alpha &= \frac{\tau_o||\tau_{bulk} - \tau_1||\tau_\ell}{\tau_o||\tau_{bulk} + \tau_1||\tau_\ell}
\end{aligned} \tag{3.35}$$

Note that $0 \leq \beta \leq 1$ and $-1 \leq \alpha \leq 1$; however, I have found implicitly that $-\beta \leq \alpha \leq 1$. These parameters ($\alpha$ and β) provide stable fitting conditions with fixed and universal parameter-limits. The time constants can be calculated from α and β using the definitions in (3.35). From low-E_p ($\Delta n < \rho_1$) measurements, it is only possible to resolve the ρ_1 to N_ℓ ratio or to decouple any of the decay time constants in limiting cases of α and β directly. Since $f_\ell \approx f_Q$ during HLI measurements, accurate measurement of τ_{bulk} is possible using (3.26) and (3.2c), which enables decoupling of τ_o, τ_1, and τ_ℓ from the measured fit parameters (α, β and τ_t) using (3.36).

$$\begin{aligned} \tau_o||\tau_{bulk} &= \frac{2\tau_t}{1-\alpha} \\ \tau_1||\tau_\ell &= \frac{2\tau_t}{1+\alpha} \\ \frac{1}{\tau_o\tau_1} &= \frac{1}{(\tau_o||\tau_{bulk})(\tau_1||\tau_\ell)} + \frac{\beta^2-1}{4\tau_t^2} \end{aligned} \tag{3.36}$$

As E_p is increased to the point where $\Delta n > \rho_1$ and eventually to the HLI ($\Delta n > N_{D/A}$), the traps saturate very quickly (i.e. $I_{tr} \to 1$) with a negligible number of carriers lost to trap filling. Without any approximation, (3.29) can be substituted into (3.34) to obtain a nonlinear oscillator equation, yielding intuition about the system's behaviour. From (3.29c) we see a term that restores the system to quasi-equilibrium ($(f - f_Q)(\rho_1 + \Delta n)\sigma v N_\ell$), and the dependence of this term on carrier density leads to a stiffening of the oscillator with increased injection. Based on this intuition, we model the $\Delta n > \rho_1$ system as being at quasi-equilibrium throughout the decay, aside from the residual trap emission observed (only in the n-type material[17]) that is accounted for during fitting with a exponential background (superimposed on the carrier density). In Section 5.2.2, these equations are used to analyze data from experiments where the excitation intensity is varied over three orders of magnitude.

[17]The motivation for the exponential background (added to Δn) when fitting in the HLI (using (3.26)) comes from (3.35) being biexponential (once the hyperbolic functions have been expanded); however unlike the $\Delta n \ll \rho_1$ case where an analytical solution (3.35) exists, we cannot resolve any useful material parameters from the relative amplitudes when using this approximate method in the HLI domain. In our experiments, an exponential background time constant was only resolvable in n-type material. A constant background was used in p-type at and above 100nJ, while no background was required to fit the data at 5 and 10nJ.

3.5 High Temperature Photoluminescence Spectroscopy

In the n-type ($N_D = 2 \times 10^{18} cm^{-3}$) CZ-GaAs PL spectra, I have observed evidence of an exponential tail in the conduction band, consistent with the findings of [33, 82].[18] I have developed an alternative analytical model (3.39) that approximates exponential-tail in the conduction-band DOS while conserving the total number of quantum-states. This model was derived by stretching the states down into the bandgap by an energy proportional to the distance from the band edge. The motivation for this approach was to find the lowest-order solution that exhibits the exponential tail while conserving the total number of states (i.e. the integral of the density of states). Also, the model reflects that electrons near the bottom of the conduction band should have the strongest perturbation to their energy levels, as described by [33]. Defining primed coordinates in relation to the bandgap energy (i.e. $E' = E - E_{gap}$), we change basis to E'_{stretch} via (3.37).

$$E'_{\text{stretch}} = E' - \left(\frac{E_o^2}{E'}\right) \tag{3.37}$$

Rearranging (3.37), we can solve for E' to obtain (3.39b). This will later be substituted so that all functions are in terms of the new basis variable (E'_{stretch}). The basis change stretches the energy axis down into the bandgap, and the modified DOS must have reduced amplitude according to (3.38) in order to preserve area (m^* is the electron effective mass).

$$\rho_{tail}(E'_{\text{stretch}}) = \frac{1}{2\pi^2}\left(\frac{2m^*}{\hbar^2}\right)^{3/2}\left(\frac{dE'}{dE'_{\text{stretch}}}\right)\sqrt{E'} \tag{3.38}$$

[18] Because of the large asymmetry between electron and hole effective masses, we can approximate the valence band as being flat near the $k = 0$ (zero crystal momentum) point if we neglect indirect transitions [33]. Because of this, the PL spectrum only probes conduction band DOS (and the localized states above the valence band) [33].

Finally, substitution of dE'/dE'_{stretch} obtained from (3.37) yields the modified DOS with exponential tails (with E' defined by (3.39b)). Now that we have completed the change of basis, we can consider E'_{stretch} to be the new energy axis. I now complete the change of basis by writing the expression replacing E' with ξ and E'_{stretch} with $E - E_{gap}$ to simplify.[19]

$$\rho_{tail}(E) = \frac{1}{2\pi^2}\left(\frac{2m^*}{\hbar^2}\right)^{3/2}\left(\frac{\sqrt{\xi}}{1+\left(\frac{E_o}{\xi}\right)^2}\right) \tag{3.39a}$$

$$\text{where,} \quad \xi = \frac{E-E_{gap}}{2} + \sqrt{\left(\frac{E-E_{gap}}{2}\right)^2 + E_o^2} \tag{3.39b}$$

Through numerical integration, I have confirmed that the transformation is area-preserving. This DOS (3.39) exhibits the exponential tail below the bandgap, and follows the e^{E/E_o} behaviour described by [33] as shown in Fig. 3.4. By multiplying $\rho_{tail}(E - E_{gap})$ by the Fermi-Dirac occupation probability, we get the occupation number $n(E - E_{gap})$ shown in (3.40). The PL spectrum is expected to have the same shape as the conduction band occupation number [33], and fitting using (3.40) is demonstrated in Section 5.1.

$$n(E - E_{gap}) = \frac{\rho_{tail}(E - E_{gap})}{1 + e^{(E-E_F)/k_BT}} \tag{3.40}$$

[19] We no longer need symbols for two energy axes, as one was only used as an artificial basis to transform the parabolic DOS. The use of ξ is only required for notational simplicity (the equation looks unclear following its substitution), and so the introduction of ξ is intended only to clarify how (3.40) and (3.39) should be used for fitting experimental data.

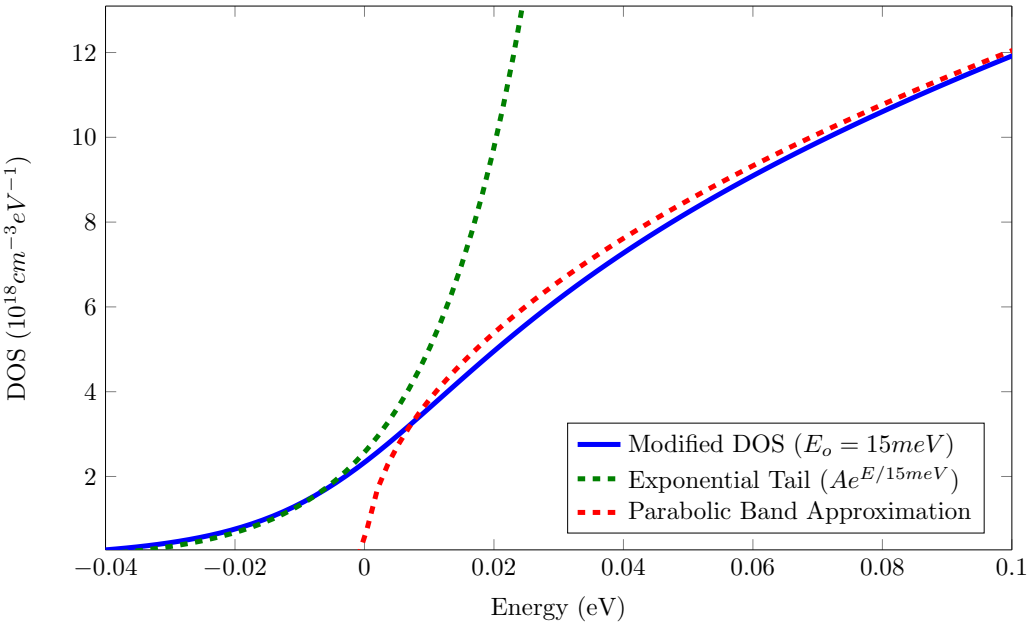

Figure 3.4: The approximate density of states (3.39) exhibits an exponential tail below the bandgap, approaches the parabolic-band approximation (proportional to $\sqrt{E - E_g}$) as temperature is increased, and conserves the number of states.

Chapter 4

Methodology

The TD-TR-PLD apparatus was designed to allow for manipulation of temperature (down to 77K) while maximizing collected PL. Fig. 4.1 shows a picture of the experimental apparatus, and Fig. 4.2 shows a schematic diagram. Excitation is provided at 532nm by a laser that provides exceptionally high instantaneous power, providing pulse energies as high as $4\mu J$ with durations of $\sim 35ps$, and this enables HLI and radially-homogeneous conditions. A monochromator provides selectivity of the PL wavelength and suppression of stray laser light and background emission. An avalanche photodiode (APD) and time-correlated single-photon counting (TCSPC) electronics are used to maximize the temporal resolution of the signal acquisition, such that it is limited by the laser and APD around 35ps. To allow for measurement of fast-decaying signals at high repetition rate, I designed and built an afterpulse filter.[1]

[1]See Appendix B and [83] for further discussion about the afterpulse filter.

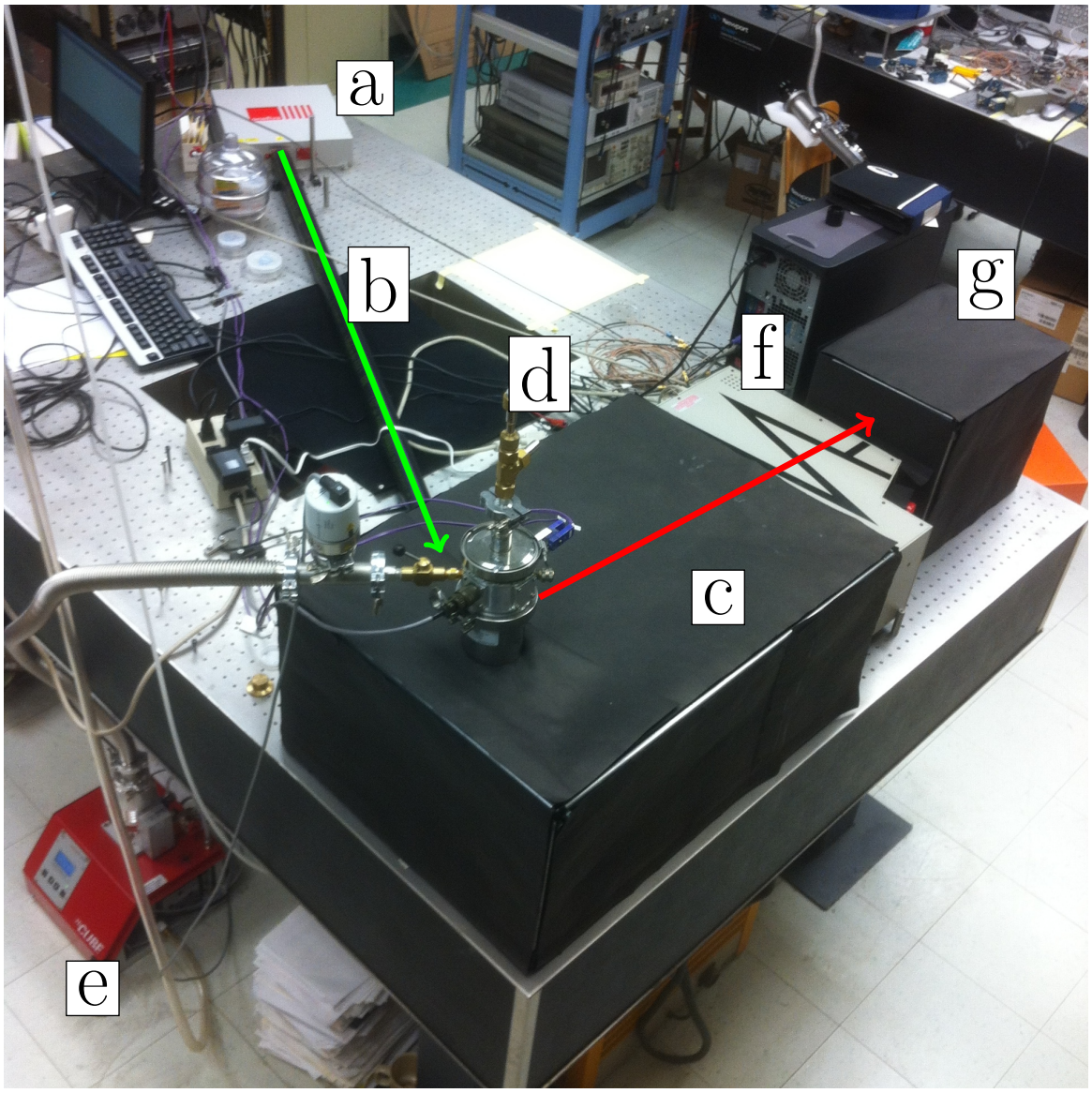

Figure 4.1: Optical bench containing experimental apparatus used in this work. The green arrow shows the 532nm excitation beam path, while the red arrow roughly shows the photoluminescence beam path. The laser (a) beam diverges while contained in the black tube (b), and enters the laser confinement box (c) which absorbs diffuse reflections. The cryostat (d) protrudes from the laser-confinement box, and is connected to the vacuum pumping station (e). The monochromator (f) can be seen between the laser-confinement box, and the detector dark box (g).

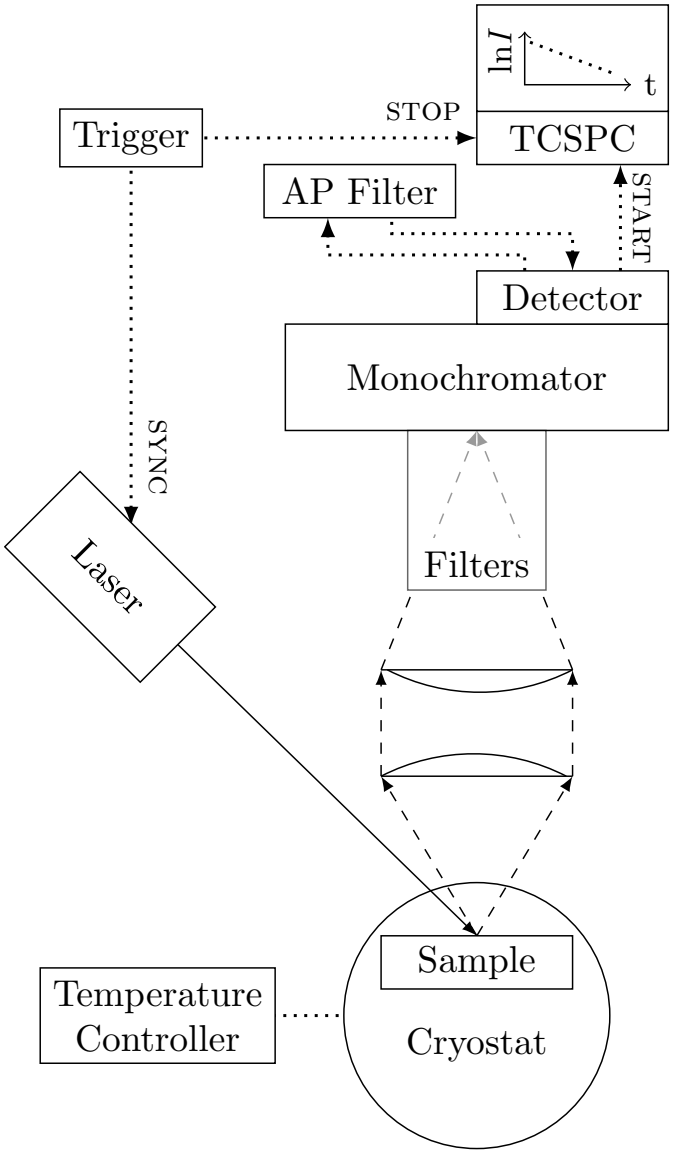

Figure 4.2: Experimental schematic showing 532nm (solid line) excitation from the Katana-05HP (Laser). Samples are mounted in the VPF-800 (Cryostat), which is controlled (dotted line) by the LakeShore-335 (Temperature Controller). PL (dashed line) is collimated by EO-86-916 and refocused by Newport-KPX232AR.16 plano-convex lenses. The PL enters a Newport-LT20-EX lens tube (Filters) containing EO-86-130 and EO-84-760 filters, before reaching the MS257 (Monochromator). A focusing lens (Newport-KBX046AR.16) is used to couple the PL into the PDM APD (Detector). The analog detector output provides the START signal for the SPC-130 (TCSPC) electronics, while the Keysight-33552B (Trigger) provides phase control between the STOP and SYNC signals (dotted lines). To prevent afterpulses from being recorded, the TTL output of the PDM (Detector) is sent to a monostable multivibrator (AP Filter) which provides a TTL signal that is sent back to the gate input of the PDM (Detector) to block afterpulses.

4.1 Sample Descriptions

GaAs samples grown using CZ and MBE were studied using TD-TR-PLD. The CZ-GaAs wafer was n-type, and was doped to a donor density of $N_D = 2 \times 10^{18} cm^{-3}$. The 500nm GaAs films of both doping types ($10^{16} cm^{-3}$) were grown by Dr. Shahram Tavakoli using the MBE system at McMaster University. On each side of the GaAs layer, 25nm of undoped $In_{0.485}Ga_{0.515}P$ was grown to confine the carriers to the epitaxial GaAs layer and provide passivation of surface defects. This structure is called a double heterostructure (DH). Doping was accomplished by introducing silicon (n-type) and beryllium (p-type) impurities during growth. The doping type and level were confirmed using Hall effect measurements with the van der Pauw method [84], and corrections for depletion according to the methods of Chandra et al. [13]. These structures were simulated using wxAMPS, and this is discussed further in Chapter 6.

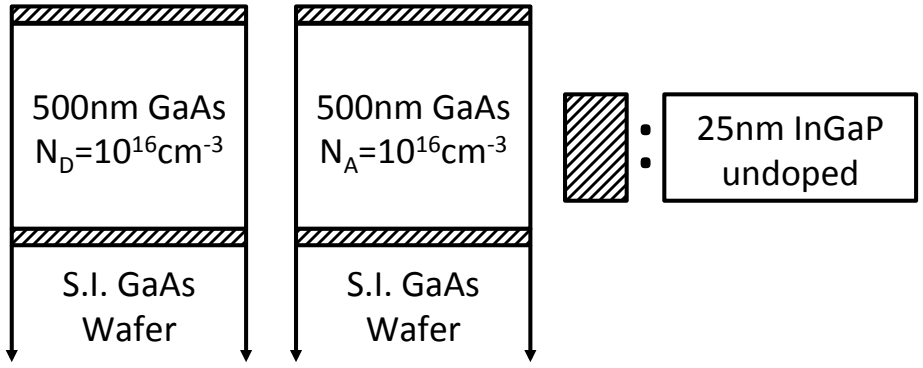

Figure 4.3: Schematic drawings of the $10^{16} cm^{-3}$ 500nm GaAs double-heterostructure (DH) samples grown for this project using MBE.

4.2 Excitation Conditions

Excitation at 532nm was performed using a pulsed laser (Onefive GmbH, Katana 05HP) with high pulse energy (up to a 4 μJ) and short pulse duration (35ps, full-width at half-maximum). Given the remarkably short pulse duration provided by this laser at these pulse energies, there is sufficient instantaneous power to provide initial excess-carrier-densities on the order of $10^{16} - 10^{17} cm^{-3}$ with the beam defocused to a Gaussian breadth of $\sigma_r = 2mm$. Defocused excitation provides radial Δn-homogeneity, and allows us to neglect radial diffusion in the study of thin and thick materials. The exceptionally high instantaneous power of this laser has enabled my work with HLI initial-conditions in the MBE samples, and has provided conditions under which the nonlinearity associated with my new HLI model can be isolated. Focusing the laser can provide higher injection levels (up to $10^{19} - 10^{20} cm^{-3}$) to allow for the HLI study of samples with higher doping; however, care should be taken when focusing this laser as it is powerful enough ablate and ignite materials.

4.3 Temperature Control and Vacuum Equipment

A Janis cryostat (VPF-800) was used as the sample chamber for this experiment, and the temperature was varied from 77K to 700K with a Lake Shore temperature controller (Model 335). To mount the samples, the cryostat opens and the interior can be removed so that the sample stage can be accessed.[2]

The cryostat was customized to have an enlarged window to allow the sample holder to extend up to the window. This customization allows us to collect light with the full solid-angle of the F/#=1 lens. High-temperature epoxy has been applied (in place of the standard O-rings) to hold the windows in place, allowing us to still bring

[2]Take care here when changing samples. Support the cryostat (e.g. with foam, as in Fig. D.7), and secure the sample with some vacuum grease as an added precaution to prevent sample breakage. An acetone/methanol rub can remove this grease. Be sure to also clean the sample holder to avoid front-surface contamination.

the temperature up to 700K with a fan blowing on the window block.[3]

4.4 Collection Optics and Filters

The ultimate throughput of a PL system is limited by the solid angle of the first collection lens, and by the losses in the monochromator.[4] I have minimized solid angle losses using a low f-number (F/#=1) lens from Edmund Optics (EO, 86-916). A 75mm diameter lens was selected to allow for maximum focal length, and make room for the cryostat window and laser beam.

MS257 is a high throughput Oriel monochromator. Before the monochromator, excitation (532nm) and background (IR) wavelengths are suppressed using an OD6 (optical-density)[5] notch filter (EO, 86-130) and OD4 700nm long-pass filter (EO, 84-760), respectively. A motorized turret allows selection between four Newport diffraction gratings (77753, 77752, 77767, and 77745), which I selected for gap free coverage with >70% reflection from 400-1700nm, and >20% from 300-2200nm. This wide bandwidth enables characterization of a variety of semiconductors in future research.[6]

4.5 Time-Correlated Single-Photon Counting

To measure TR-PLD, I have applied the method of time-correlated single-photon counting[7] (TCSPC), using an avalanche photodiode (APD) from Micro Photon Devices

[3]With the sample holder extended so close to the window, the window is held at a higher temperature. There was a risk of the O-rings failing at these temperatures, and so epoxy was used instead. This is a result of the customization, and the fan is a precaution.

[4]Reflective losses also play a role, and these have been minimized by suitable choice of optical materials and coatings.

[5]The OD number of a filter gives the (base-10) logarithm of the degree of attenuation.

[6]Currently the silicon APD limits the maximum observable wavelength to just above 1100nm (signals become barely resolvable around $\sim 1200nm$), and emission only occurs below the laser wavelength of 532nm; however, there is a secondary detector port where a NIR-APD or photomultiplier tube could be placed (likely extending the long wavelength to ∼1700nm) and alternate lasers can be easily aligned with the system to allow for excitation at any wavelength.

[7]I have used TCSPC since we are dealing with low light levels (small signals), and short (nanosecond-scale) lifetimes. For a general introduction to TCSPC, see [85]

($50\mu m$ PDM) as our single-photon detector. I have selected an APD since it provides better temporal resolution (35ps) relative to the transit-time-spread in photomultiplier tubes (>300ps). In TCSPC, the detector (a μm-scale silicon diode operating near its breakdown voltage) absorbs a single photon, causing a cascade of impact ionization in the depletion region and delivering a pulse of around one million electrons. The basic task of the TCSPC electronics is to time the arrival of each of these detector pulses.

Inside our TCSPC card (Becker & Hickl, SPC-130), there are two fundamental units at work: the constant fraction discriminator (CFD), and the time-to-amplitude converter (TAC). The CFD is like a conventional discriminator,[8] except that instead of setting a threshold *level*, a threshold *fraction* is set. Using a CFD protects against the effect that fluctuations in APD pulse-amplitude have on the measured time.[9] In our system,[10] an electron pulse from the APD sends a START signal to the TAC and the next laser trigger signal that arrives provides the STOP signal that instructs the TCSPC card to digitize the voltage-amplitude[11] on the TAC. By repeatedly measuring arrival times of photons, the TR-PLD signal is accumulated.

To maximize the temporal resolution, phase control of the STOP signal reaching the TCSPC electronics in relation to the SYNC signal that triggers the laser (see Fig. 4.2) is provided by the Keysight signal generator (33552B). The Keysight provides two outputs with excellent phase-control, allowing us to quickly select optimal sampling conditions to maximize the resolution of the TCSPC electronics.

Only one event is recorded per repetition by the TCSPC electronics as the system becomes dead until the next repetition, and so the repetition rate must be kept sufficiently low so that a negligible number of photons are missed due to this so-called

[8] A discriminator gives a binary output that changes depending on whether the input is above or below some threshold.

[9] Note that the pulses are usually (ideally Gaussian) shaped by pulse shaping electronics before reaching the CFD [85].

[10] The SPC-130 operates in "reversed START-STOP" mode [85].

[11] Essentially, a current source is turned on and charges a capacitor, yielding a linearly increasing voltage amplitude. The voltage-amplitude to time characteristics of the TAC have been calibrated, and are controlled with the provided software.

photon-pileup effect [85]. To ensure that a negligible amount of photon-pileup occurs, the detection-rate was kept below 10% of the laser-repetition-rate by control of the monochromator slit-width.[12] The effects of photon-pileup were assessed by detection rate variation, and I verified that no systematic error was introduced at a detection rate of 10% of the repetition rate in my experiments. The dark count rate (i.e. the count-rate from thermal noise) of the APD is accounted for during nonlinear fitting; however, the background arising from APD afterpulses was filtered out using a gate circuit (monostable multivibrator) that I built (see Appendix B).

One advantage of TCSPC is that it offers superior temporal resolution (5ps) to state-of-the-art sampling oscilloscopes. The temporal resolution of sampling oscilloscopes used to be significantly lower than TCSPC. While this gap has narrowed, the fastest sampling oscilloscopes currently available are still ten times lower in time-resolution than our TCSPC electronics. This ensures that the TCSPC electronics are not limiting, and that the APD and the laser both limit the time-resolution of this system to 35ps. The high temporal resolution of the TCSPC electronics also allows us to measure the instrumental response function with higher resolution, for the case of experiments with sufficiently short lifetimes to require reconvolution-fitting. The high temporal resolution of this system enables the study of highly-doped, defective, and nanostructured materials, all of which may have sub-nanosecond lifetimes.

[12] If the count-rate exceeds 10% of the repetition rate then the second photon is not recorded, which results in a systematic underestimation of the lifetime. This effect is known as photon pileup [85].

Chapter 5

Experimental Results and Discussion

5.1 Photoluminescence Spectroscopy

PL spectra were measured (from the $N_D = 2\times10^{18}cm^{-3}$ CZ-GaAs wafer) from 77-600K. Fig. 5.1 show Gaussian fits to the spectra measured from 77-150K. Three peaks are present in these spectra, and the predominance of the lower-energy peak indicates that recombination is occurring primarily via the localized states. The spectra measured at 200-300K are shown in Fig. 5.2. At and above 200K, there was sufficient asymmetry in the higher-energy peak to enable fitting with (3.40), allowing for measurement of the bandgap energy. Localization is still evident at and below 300K, preventing estimation of the doping level from these fits. It is clear from the PL spectra that a shift in occupation from localized states to extended states occurs between 150K and 300K.

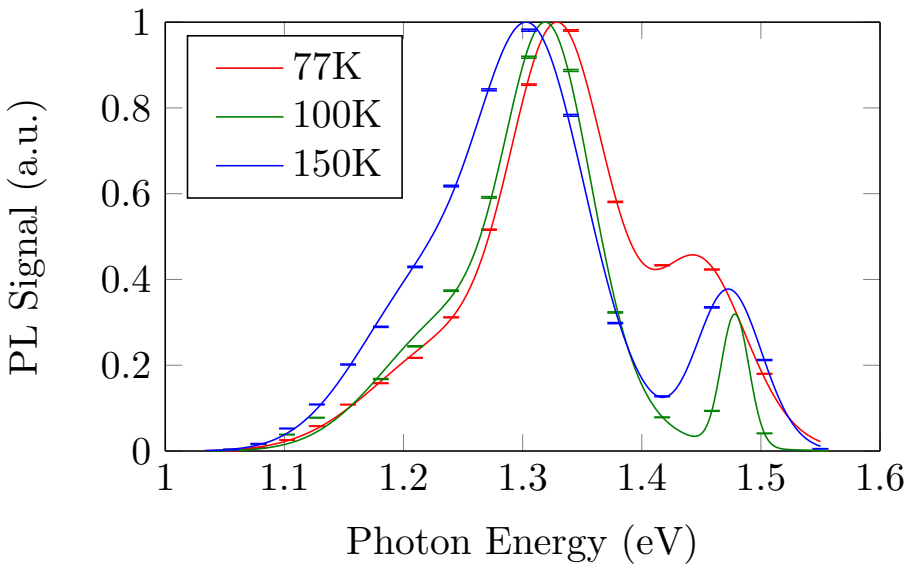

Figure 5.1: PL spectra taken below 150K, shown with 3 gaussian peak fits. Excitation was at 532nm, and the wavelength resolution is $\Delta\lambda = 25nm$.

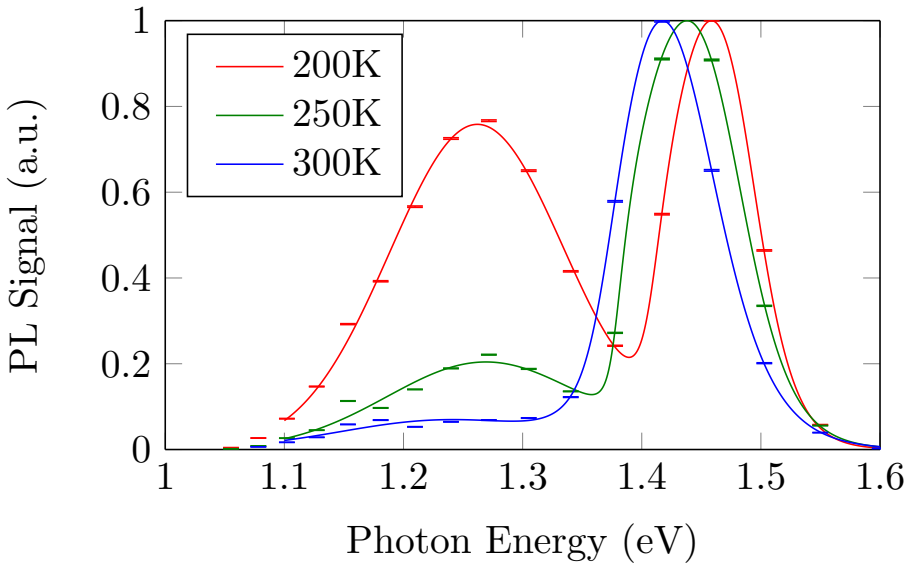

Figure 5.2: PL spectra above 200K, where fitting with (3.40) was possible and the bandgap (Fig. 5.7) was measured. A superimposed Gaussian function accounted for the localized PL signal, and this screens measurement of the Fermi level. While band-to-band recombination becomes dominant at 300K, localization is still evident. Excitation was at 532nm, and the wavelength resolution is $\Delta\lambda = 25nm$.

Spectra measured above room temperature were fit with (3.40), and are shown from 350-550K in Fig. 5.3 and 600K in Fig. 5.4. Fitting with this new model has allowed measurement of $E_g = (1262 \pm 1) meV$, $E_F = (1240 \pm 4) meV$, and $E_o = (14.5 \pm 0.3) meV$ from the results at 600K. The doping-level is high enough that the Boltzmann approximation is no longer accurate, as shown in Fig. 5.5. This is what provides information from which the Fermi-level position can be estimated. To calculate n_o from E_F, nonparabolicity of the direct valley and contributions of indirect valleys must be taken into account through use of the appropriate effective density of states (C.1) for the GaAs conduction band. The electron density calculated from the 600K results is $n_o = N_C(600K) e^{-(E_g - E_F)/k_B T} = (2.3 \pm 0.2) \times 10^{18} cm^{-3}$. Using the same calculation, n_o was measured from 350-550K fits, and these results are shown in Fig. 5.6. Additional fit parameters extracted from the 77-600K spectra are plotted in Fig. 5.7, and are shown with results using fits with fixed and variable temperature.

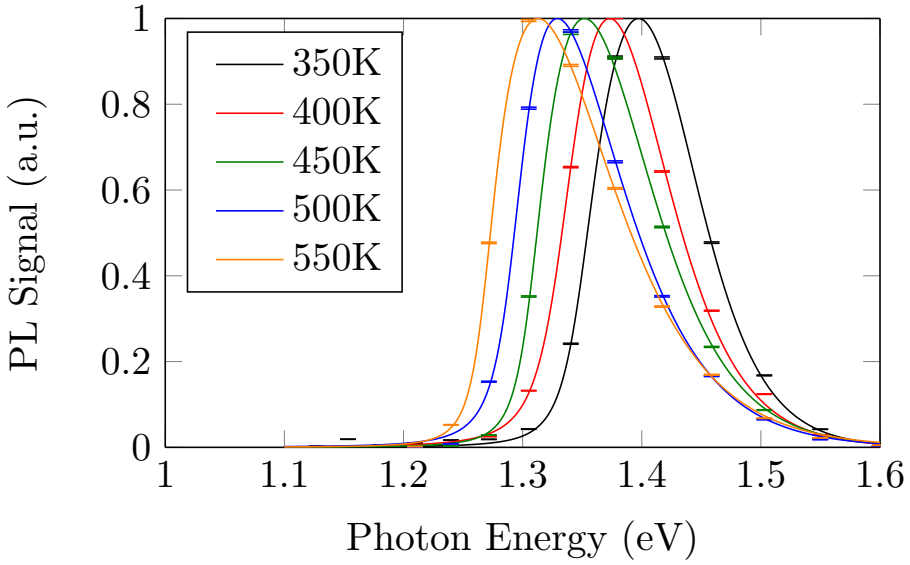

Figure 5.3: PL spectra taken above 350K, where fitting with (3.40) was possible and the bandgap (Fig. 5.7) and doping density (Fig. 5.6) were measured. Excitation was at 532nm, and the wavelength resolution is $\Delta\lambda = 25nm$.

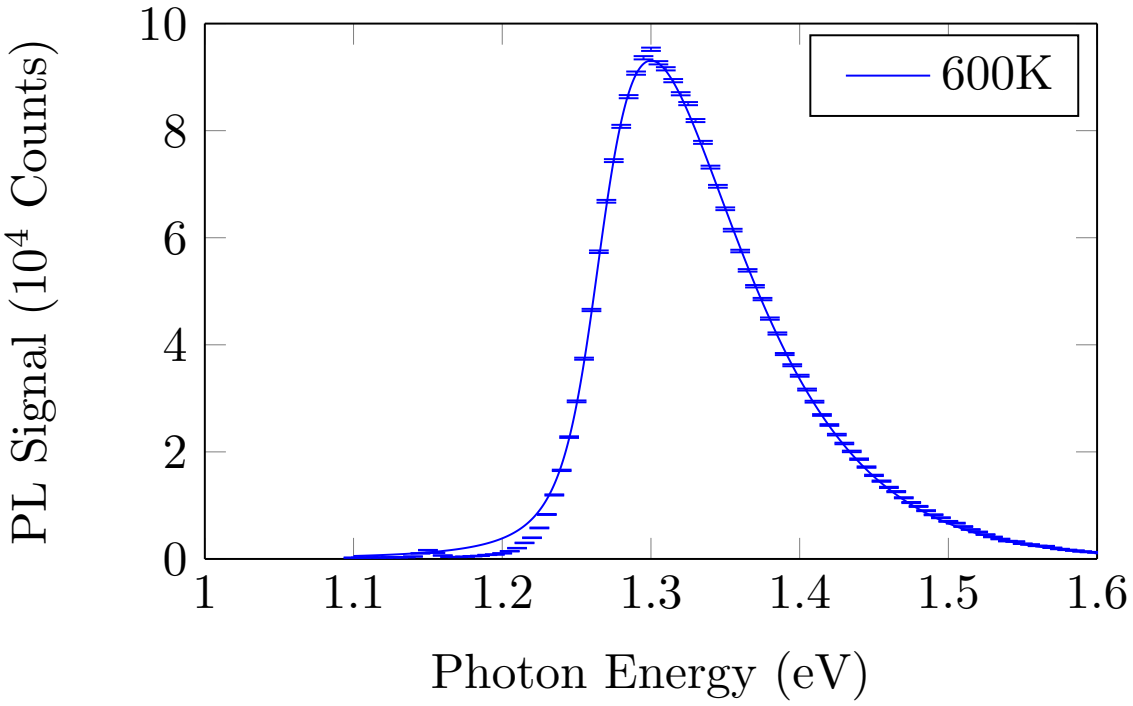

Figure 5.4: Fit to PL spectrum at 600K with (3.40). The Fermi-level ($E_F = (1240 \pm 4)meV$), bandgap ($E_{gap}(600K) = (1262 \pm 1)meV$), and $E_o = (14.5 \pm 0.3)meV$ were measured as fit parameters. The energy resolution is $\Delta E = 5meV$.

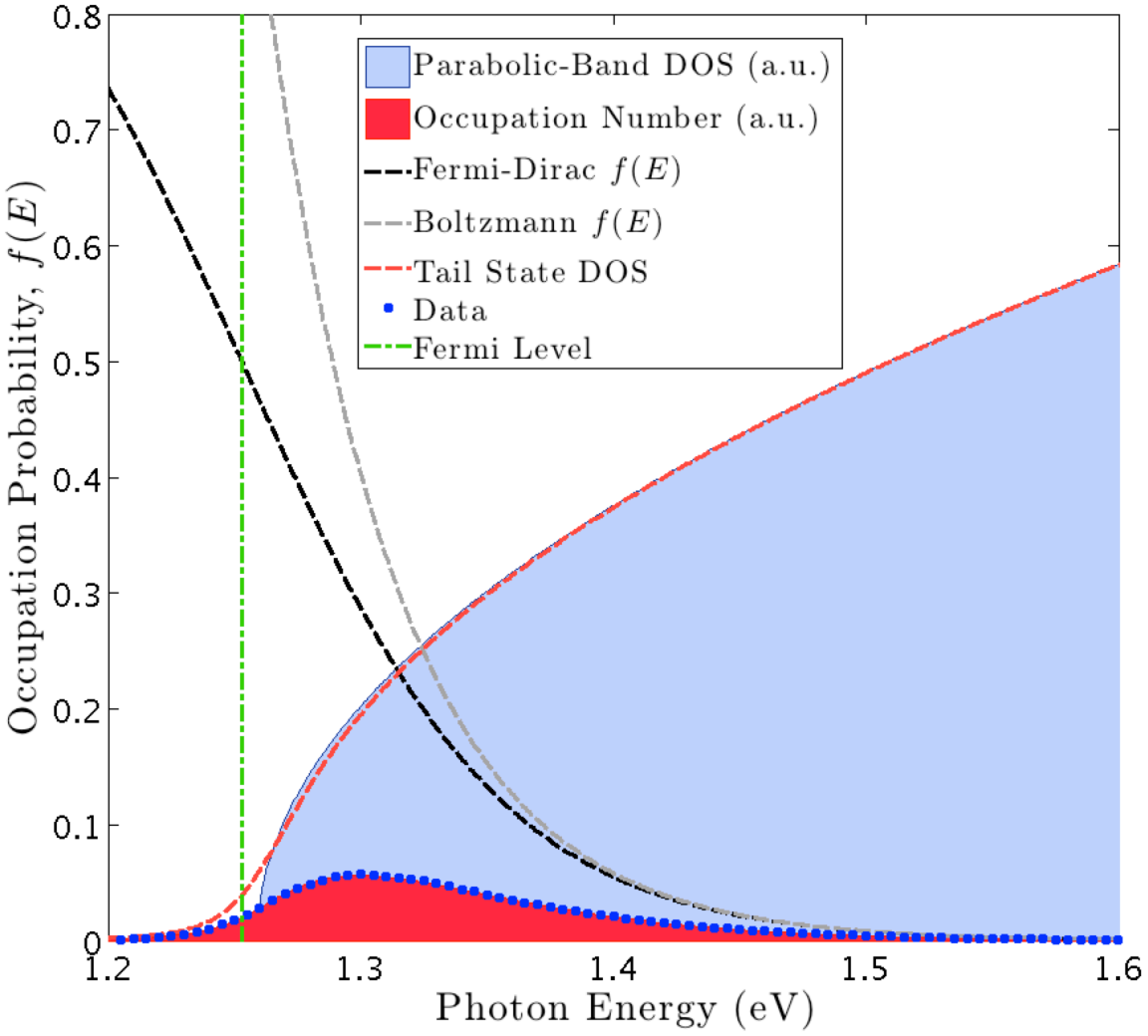

Figure 5.5: Density of states measured from fitting PL spectrum with (3.40) (also shown in Fig. 5.4), shown with the Boltzmann approximation to highlight the origin of the Fermi-level information.

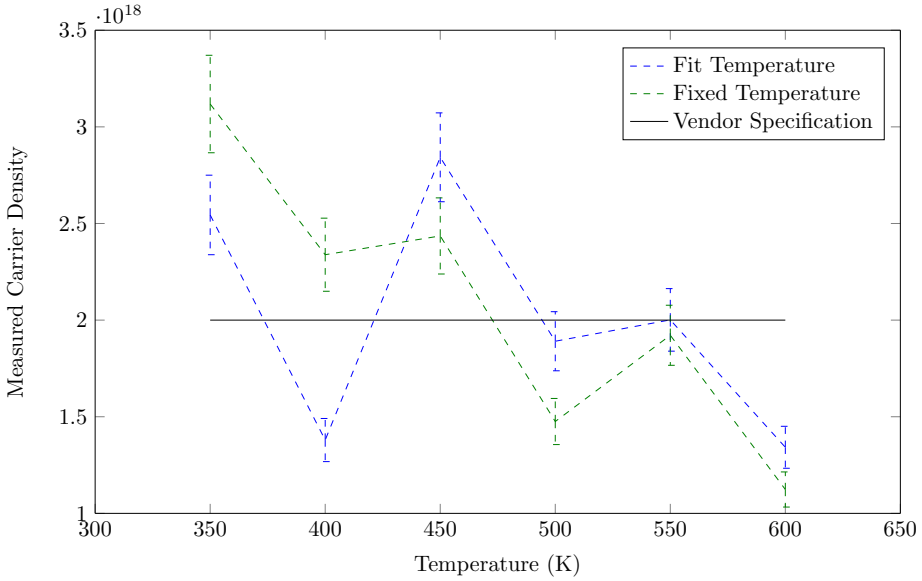

Figure 5.6: Electron density calculated using $N_C(T)$ from (C.1), with E_g and E_F measured from fitting PL spectra with (3.40).

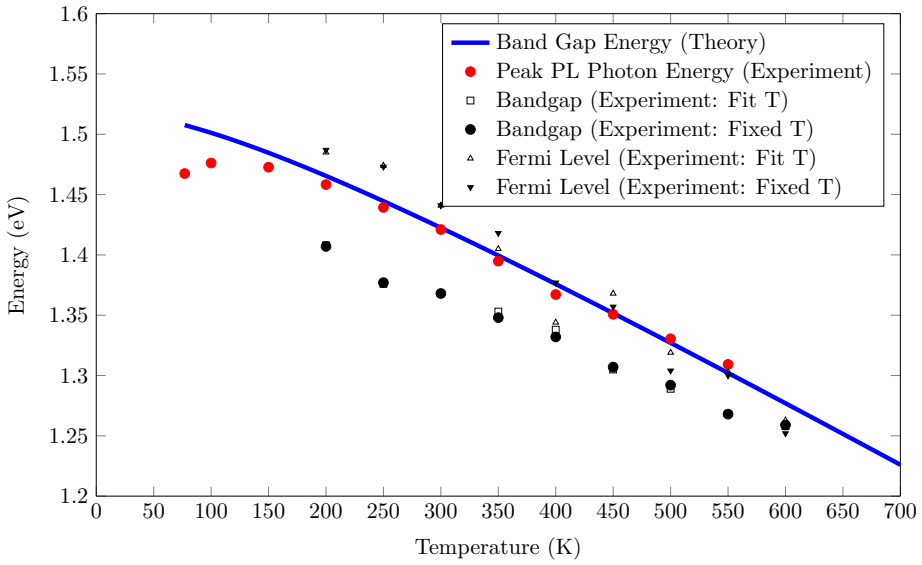

Figure 5.7: Fit parameters measured from PL spectra. Data from 77-150K was fit with three Gaussian functions. Spectra from 200-600K were fit with (3.40), allowing bandgap measurement. A Gaussian peak was superimposed on the 200-300K results to account for additional localization at these temperatures. Fermi-level measurement was possible with (3.40) for 350-600K.

Observation of conduction-band exponential tail-states is consistent with behaviour previously found above doping-levels of $10^{17}cm^{-3}$ in n- and p-type GaAs [33]. Fig. 5.7 shows indication of bandgap shrinkage. The slope of the exponential tail was found to remain constant with temperature from the 250-600K fits, and the measured average value of $E_o = (13 \pm 2)meV$ agrees with IR-absorption observations of E_o in n-GaAs between 5 and $18meV$, and is consistent with the value of $13.6meV$ measured at $N_D = 3 \times 10^{18}cm^{-3}$ [82]. The observed average reduction in the bandgap ($E_{gap}^{theory} - E_{gap}^{measured} = (45 \pm 5)meV$) is reasonably close to the theoretical expectation of $28meV$ calculated using n-type bandgap shrinkage theory from [86].

Determining the PL peak wavelength is an important step in resolving $\tau_{bulk}(T)$, as the measured lifetime depends on the observed emission wavelength [80] (especially in LLI measurements). I have found that the PL peak closely tracks the bandgap energy (Fig. 5.7) in this moderately doped sample, and so the theoretical bandgap provides a good starting point for peak searching during measurements. To check the calibration between the sample temperature and thermocouple reading, fits were performed with both fixed and variable temperature.[1] Fig. 5.8 shows that the measured sample temperatures match quite closely the thermocouple temperature, indicating that this technique can also serve as a sample-temperature probe above 200K (as well as verifying the calibration of the thermocouple).

[1] All fits shown in Figs. 5.1-5.4 were performed with fixed-temperature.

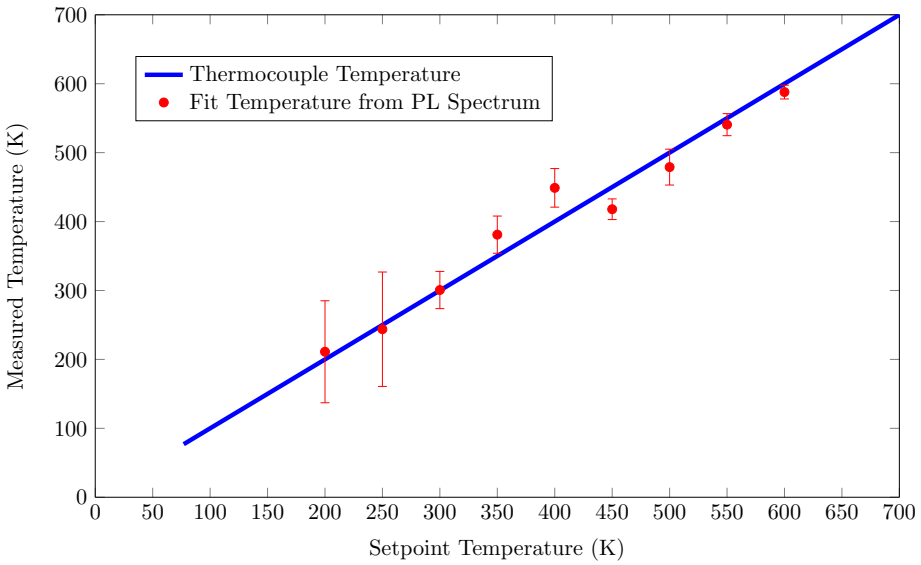

Figure 5.8: Temperature measured from fits of PL spectra from 200-600K with (3.40) using floating-temperature, compared with the temperature monitored by thermocouple.

5.2 Analysis of Time-Resolved Photoluminescence

5.2.1 Thick GaAs: Decoupling Diffusion and Surface Recombination

With TR-PLD experiments using CZ-GaAs, I have found that approximation (3.20) gives equivalent results to the model of Vaitkus (3.19) from 77-600K. Under these conditions, the shape of TR-PLD is independent of the surface recombination velocity, absorptivity, and diffusivity. This asymptotic limit of the equation of Vaitkus [3] was proposed for $t > \tau_{bulk}$ by Ahrenkiel et al. [79]; however, no connection was made to the high surface-loss limit with strong absorption. Here, I will provide experimental evidence that the approximation is also valid for $t \ll \tau_{bulk}$ if absorption is strong and surface loss is high. I will present lifetime measurements from 77-600K that

demonstrate that no loss in accuracy is associated with the asymptotic approximation for systems with large front-surface loss ($\tau_{FS} \ll \tau_{bulk}$), negligible rear-surface loss ($\tau_{tr} \gg \tau_{bulk}$), and strong absorption ($\tau_z \ll \tau_{bulk}$).[2]

Figs. 5.9-5.11 show TR-PLD from 77-300K, fit with the Vaitkus model (5.1) and the new approximation (5.2). In modelling the system this way, I have assumed that carriers diffuse in the extended states before they transition into localized states deeper in the material, giving rise to two independent lifetimes associated with decay from extended- (τ_A) and localized- (τ_B) states. Adding two signals from the Vaitkus model (3.19) gives (5.1).

$$I_{PL}(t) = \left(\frac{\sqrt{\tau_z}\text{erfce}\sqrt{t/\tau_z} - \sqrt{\tau_{FS}}\text{erfce}\sqrt{t/\tau_{FS}}}{\sqrt{\tau_z} - \sqrt{\tau_{FS}}} \right) \left(Ae^{-t/\tau_A} + Be^{-t/\tau_B} \right) \tag{5.1}$$

Using approximation (3.18), I have shown that (3.19) can be approximated by (3.20). Adding two (3.20) signals together results in (5.2).

$$I_{PL}(t) = A\frac{e^{-t/\tau_A}}{\sqrt{t}} + B\frac{e^{-t/\tau_B}}{\sqrt{t}} \tag{5.2}$$

[2]Note that this method is not restricted to direct bandgap semiconductors. For instance, Si absorbs ultraviolet light more readily than GaAs does 532nm [6].

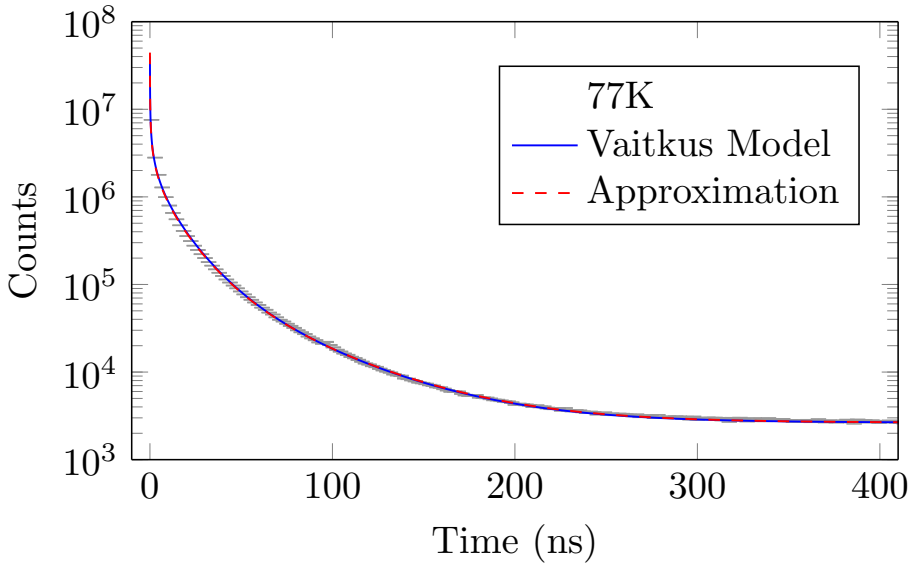

Figure 5.9: Biexponential fits to TR-PLD (grey) at 77K using (5.1) (blue solid line) and (5.2) (red dashed line). This measurement was performed with a 532nm laser, at a repetition rate of 1MHz, and pulse energy of 0.3nJ (defocused to σ=2mm). The emission was monitored at 870nm with 2mm slits. The bin width is 2.0ns.

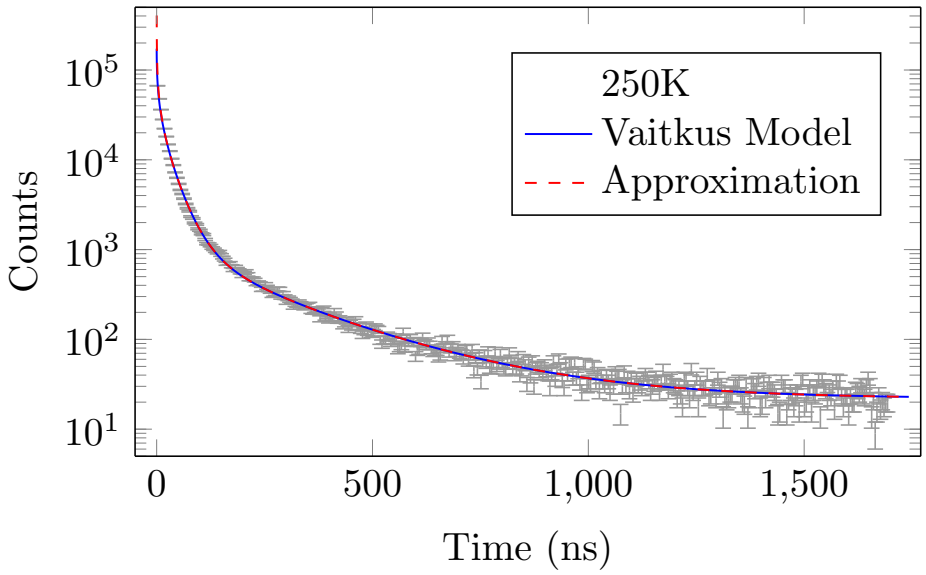

Figure 5.10: Biexponential fits to TR-PLD (grey) at 250K using (5.1) (blue solid line) and (5.2) (red dashed line). This measurement was performed with a 532nm laser, at a repetition rate of 500kHz, and pulse energy of 24nJ (defocused to σ=2mm). The emission was monitored at 1050nm with 2mm slits. The bin width is 4.1ns.

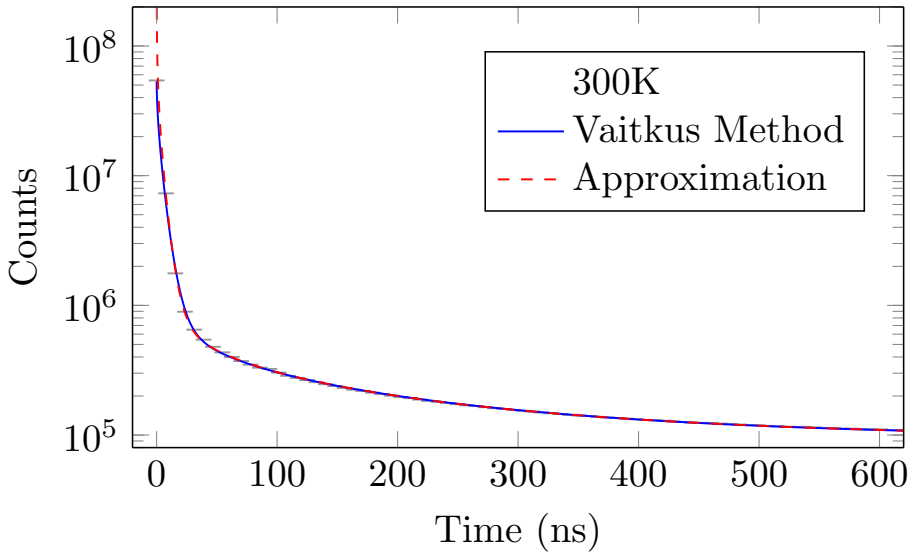

Figure 5.11: Biexponential fits to TR-PLD (grey) at 300K using (5.1) (blue solid line) and (5.2) (red dashed line). This measurement was performed with a 532nm laser, at a repetition rate of 500kHz, and pulse energy of 4.7nJ (defocused to σ=2mm). The emission was monitored at 870nm with 2mm slits. The bin width is 7.8ns.

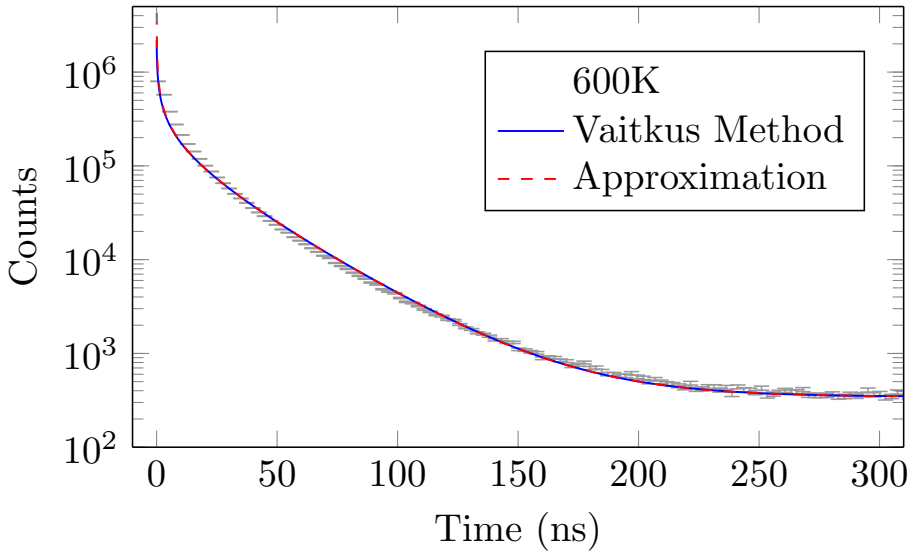

Figure 5.12: Fits to TR-PLD at 600K using (3.19) (blue solid line) and (3.20) (red dashed line). This measurement was performed with a 532nm laser, at a repetition rate of 50kHz, and pulse energy of 1nJ (defocused to σ=2mm). The emission was monitored at 955nm with 2mm slits. The bin width is 2.5ns.

For the data where trap-emission was observed (77-300K), I have compared fits

Model	Lifetime (ns)			
	77K	250K	300K	600K
Vaitkus Model	17.1±0.8 55.2±1.3	36±5 310±20	6.6±0.3 293±10	34.3±5
Approximation	17.2±0.6 56.1±1	36±4 310±20	5.7±0.1 294±5	34.3±0.4
Simple Exponentials	8.2±0.5 40±1	26±2 220±10	5.8±0.4 151±10	25.9±0.4

Table 5.1: Extended-state (τ_A) and localized-state (τ_B, and τ_{bulk}) time constants measured with varied I_∞ and temperature. Biexponential fitting with the Vaitkus model (5.1) and approximation (5.2) was used when localization was observed (77-300K). Fits at 600K were performed using the Vaitkus model (3.19) and approximation (3.20).

of the data using (5.1), (5.2), and simple biexponential exponential decay. At 600K, only a single exponential was needed to fit the data, as localization effects are no longer observed. The TR-PLD results from 600K are fit with (3.19), (3.20), and simple monoexponential decay. Fig. 5.12 shows TR-PLD taken at 600K, comparing fits with (3.19) and (3.20). The fits from 77-600K all demonstrate the equivalence of the Vaitkus model (3.19) and approximation (3.20) under these circumstances, as seen visually in the fits and numerically in the measured lifetimes, shown in Table 5.1.

The applicability of this new approximation (3.20) greatly simplifies accurate τ_{bulk} measurement using TR-PLD from thick unpassivated materials. As long as a strongly absorbed excitation wavelength is used and there is large ($\tau_{FS} \ll \tau_{bulk}$) surface loss, the information about diffusivity, surface loss, and absorptivity only influence the scaling factor of the decay and not the shape. As a result, fits to TR-PLD in this regime cannot be used to obtain an accurate measure of any of these parameters.

An important finding is that the surface recombination velocity contributes less than 1% to the shape of the decay for $t \geq 49\tau_{FS}$, and that this is true regardless of whether or not the material is a strong absorber. In our experiments at 77K we observe no difference between fits using (3.19) and (3.20) at early times. Estimating that $D_a(77K) = 100cm^2/s$ [5], no difference would be observed with this time resolution for

S	f_{loss}			
	77K	250K	300K	600K
∞	0.995	0.996	0.995	0.959
$10^6 cm/s$	0.955	0.986	0.987	0.951

Table 5.2: Upper and lower limits on the fraction of carriers lost to front surface recombination (f_{loss}).

$S > 10^6 cm/s$ [7], as $\tau_{FS} < 100ps$. This indicates that there is no freezing out of surface recombination at 77K. Using (3.21) and estimating $D_a = \left(169e^{-T/143K}\right) cm^2/s$ from an exponential fit to [5], we can quantify the maximum ($S \to \infty$) possible surface losses (using (3.20)), while $S = 10^6 cm/s$ is the maximum S that I have found resolvable, and so it gives a minimum bound on the measured f_{loss}, as well as a value representative for conditions typical of naturally oxidized GaAs [7]. These values of f_{loss} have been calculated, and are summarized in Table 5.2. From (3.21), it would appear that by increasing τ_z (by decreasing α), the losses could be reduced and the bulk lifetime measured; however, in this limit the back surface generally needs to be considered using the methods of Luke and Cheng [2]. For further discussion on modelling the two-surface diffusion problem, see Section 3.3.2.

The measurements from 250K exhibited the biexponential behaviour most clearly, and so these fits were repeated from 800-1050nm with ($\Delta\lambda = 25nm$). The resulting lifetimes are plotted in Fig. 5.13, along with their weighted average. At 169K and 199K, Redfield, Wittke, and Pankove [80] measured lifetimes that changed by a factor of 3 times as PL wavelength was varied from 880-970nm, by measuring the slope of the initial decay with a monoexponential fit. At 250K, I have demonstrated that the measured lifetimes remain relatively constant ($\pm 25\%$) with respect to wavelength from 800-1050nm when two lifetimes are resolved using (5.2) to fit the data. The error bars in the measured lifetime spectrum show which source is dominant at short and long wavelengths. The shorter lived contribution is dominant at shorter wavelengths, while the longer lifetime component becomes more prominent at longer wavelengths. This suggests that the band-to-band (short wavelength) signal is decaying also due to

the transition of carriers into the localized states, where they take a longer time to decay. The short-wavelength time-constant (τ_A) then characterizes the parallel rates of localization and band-to-band recombination in the material, while the long-wavelength time constant (τ_B) characterizes the rate decay from the localized states (either via trap-emission, or trap-assisted recombination).

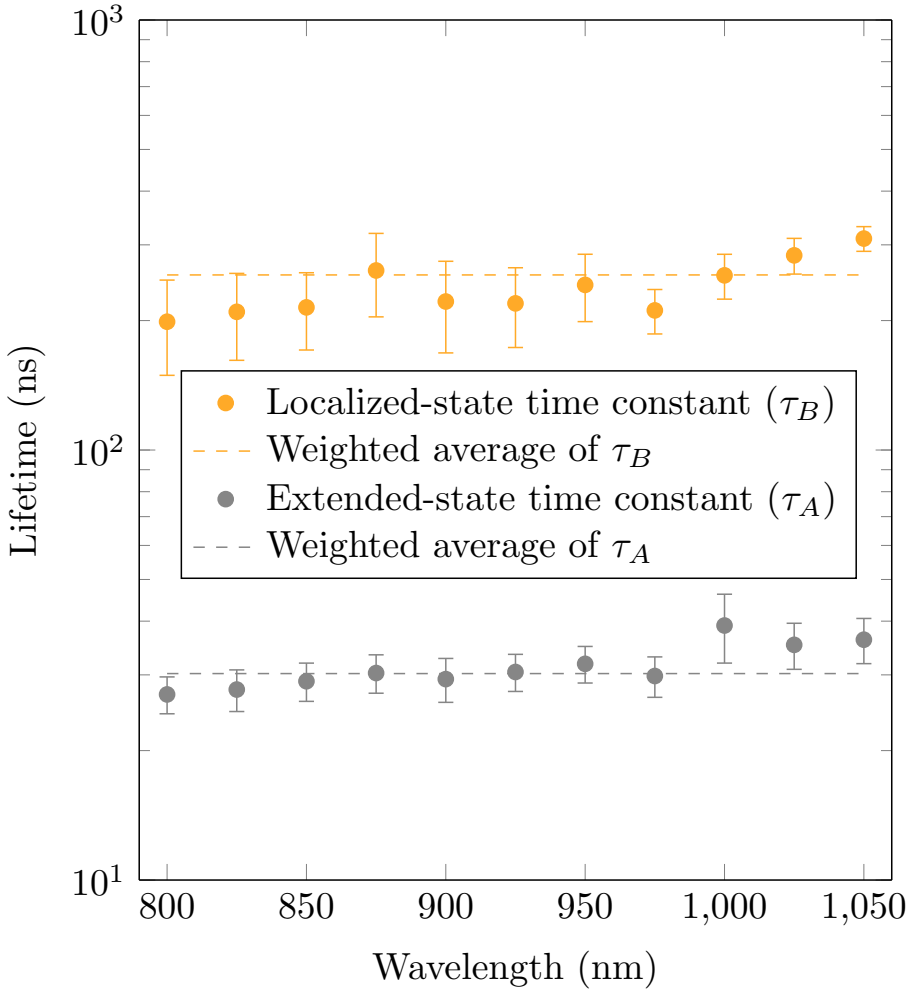

Figure 5.13: Time constants measured at 250K using varied emission wavelength. Biexponential fits using (5.2) were performed to resolve the time constants associated with decay from both localized-states (orange) and extended-states (grey).

I have shown that accurate bulk lifetime measurements can be made by fitting with (3.20) in thick unpassivated materials. Our experimental TR-PLD results from CZ-

GaAs are consistent with the assumption of a deep (diffusion-length limited) collection volume, and I have demonstrated (from 77K-600K) that fitting with (3.19) or the new approximation (3.20) yield equivalent results. This provides deeper understanding of TR-PLD from unpassivated materials, and illustrates that τ_{bulk} measurement is possible in the presence of high surface-recombination velocity.

5.2.2 Thin Films: Decoupling Recombination Dynamics, Radiative Recombination, and Trapping Processes

I have developed a new model (3.26) that enables decoupling radiative and nonradiative contributions to the lifetime by analyzing the nonlinearity in the HLI-regime, and another (3.35) that allows for measurement of trapping time constants in the LLI-regime. I will provide examples (in the GaAs system at a doping level of $10^{16}cm^{-3}$) from TR-PLD experiments with a broad range of initial carrier densities (around 10^{14} to $10^{17}cm^{-3}$). When the pulse-energy (E_p) is very high, the system quickly reaches quasi-equilibrium with negligible carrier density lost to population of the localized states. Under these high-E_p conditions, the system maintains quasi-equilibrium throughout most of the observable decay, and τ_{bulk} has been measured from these experiments. When E_p is reduced, the initial loss of minority carriers becomes observable, as well as the later trap-emission phase of the decay. The analytical models are fit to TR-PLD data taken with both LLI and HLI as initial conditions.

The TR-PLD measurements (solid black and grey lines) are shown in Figs. 5.14 and 5.15, along with plots of the fits (solid orange and broken black lines) for n-type and p-type, respectively. The fitting methods used for each E_p are outlined in Table 5.3, along with the resulting parameters of the fit, calculated from α, β, and τ_t of (3.35) using (3.36). The data taken at lower E_p have been multiplied by scaling factors for visual clarity, and these factors are indicated in the legend.

I have performed TR-PLD measurements on the n- and p-type ($10^{16}cm^{-3}$) MBE DHs. From the HLI regime (where $\Delta n > \rho_1$, defined in (3.30)) I have measured

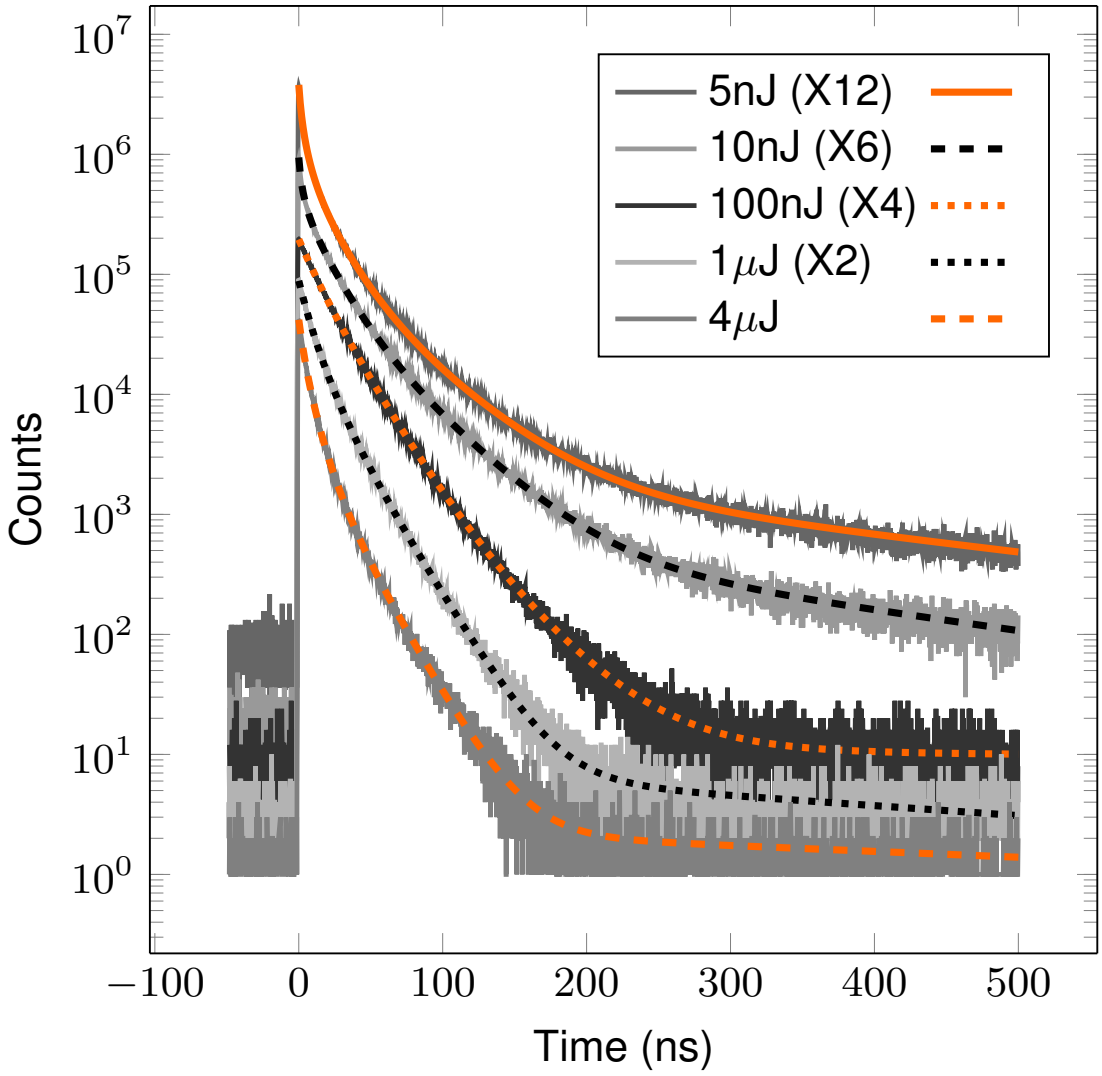

Figure 5.14: n-type 500nm GaAs DH TR-PLD measurements (solid black and grey lines) and fits (orange and broken black lines) with models described in Table 5.3. Scaling factors (applied for visual clarity) are indicated in legend. Pulse energy is varied (see legend), and the excitation wavelength was 532nm. The time-resolution was 150ps, and the emission wavelength was 885nm.

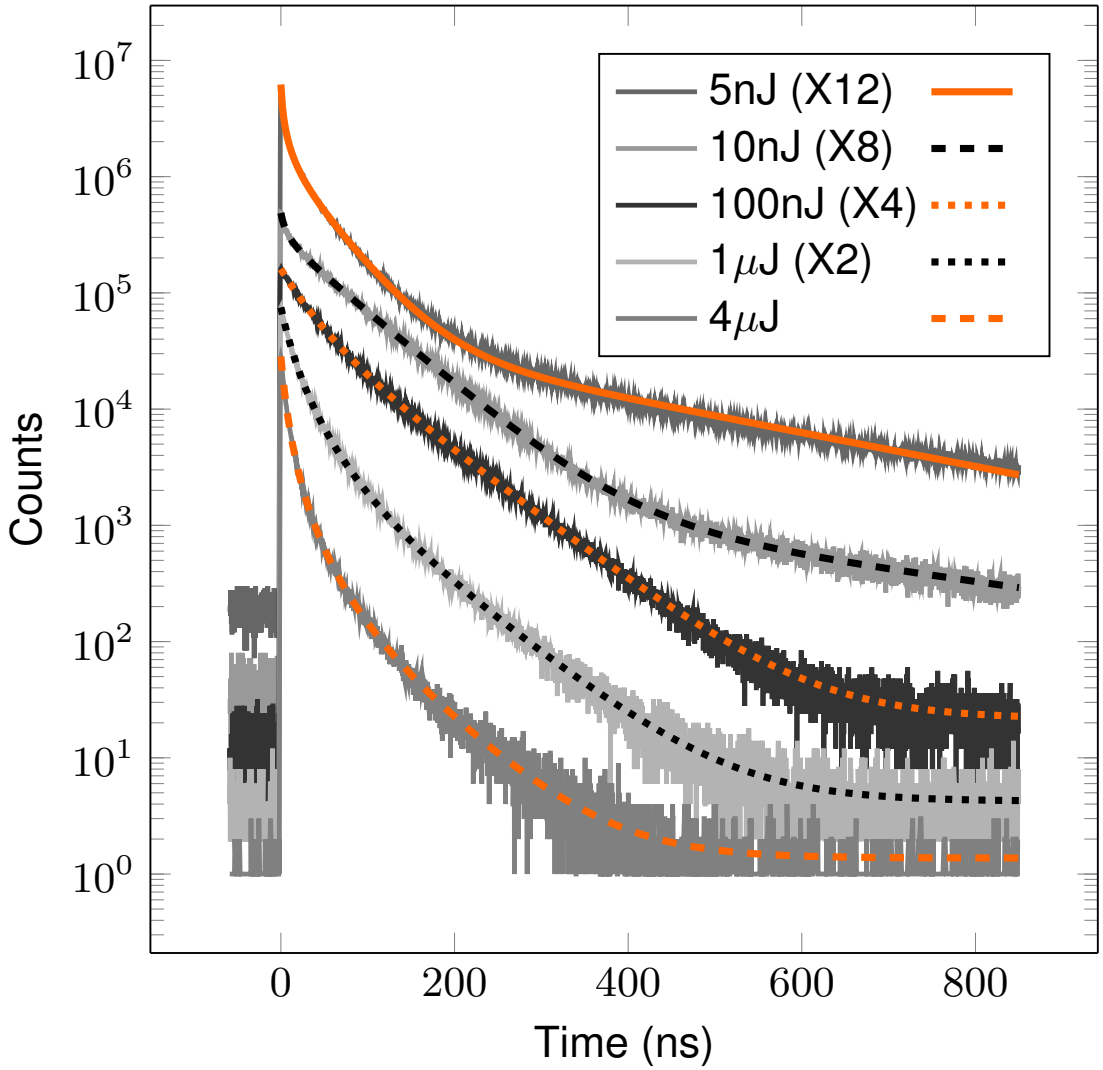

Figure 5.15: p-type 500nm GaAs DH TR-PLD measurements (solid black and grey lines) and fits (orange and broken black lines) with models described in Table 5.3. Scaling factors (applied for visual clarity) are indicated in legend. Pulse energy is varied (see legend), and the excitation wavelength was 532nm. The time-resolution was 240ps, and the emission wavelength was 885nm.

	$E_p(nJ)$	Model	η_o	τ_{bulk}	f	$\tau_\times$	δ	$\tau_o \| \tau_{bulk}$	$\tau_1 \| \tau_\ell$	$\frac{\tau_o \tau_1}{1000}$	τ_{BG}
n	4000	(3.26) & (3.2c)	4.2±0.2	21.5±0.2	0.36±0.01	–	($\delta \to 0$)	–	–	–	900±300
	1000	(3.26) & (3.2c)	2.16±0.07	22.3±0.1	0.23±0.01	–		–	–	–	520±90
	100	(3.35); $I_{tr} = 1$	0.45±0.05	–	–	–		21.5±0.9	39±2	42±3	∼5000
	10	(3.35)	–	–	–	6.3±0.1	4.85±0.07	18.1±0.2	29.7±0.3	4.6±0.1	260±10
	5	(3.35)	–	–	–	11.5±0.3	5.38±0.08	19.0±0.3	33.1±0.6	5.5±0.2	300±10
p	4000	(3.26) & (3.2c)	10.8±0.6	69±2	0.57±0.02	–	($\delta \to 0$)	–	–	–	($\tau_{BG} \to \infty$)
	1000	(3.26) & (3.2c)	5.03±0.2	76.7±0.7	0.46±0.01	–		–	–	–	
	100	(3.26) & (3.2c)	1.16±0.04	79.5±0.3	0.41±0.02	–		–	–	–	
	10	(3.35)	–	–	–	16.9±0.2	5.8±0.2	68.6±0.3	407±2	900±7	No Background
	5	(3.35)	–	–	–	21.9±0.2	14.5±0.2	46.4±0.2	252±1	87±1	

Table 5.3: Time constants (ns units) measured in n- and p-type MBE-GaAs DHs using TR-PLD with varied laser pulse-energy (E_p). The fitting functions are specified under the Model column. In the p-type samples, a constant background was used ($\tau_{BG} \to \infty$) with (3.26), and no background was required when fitting with (3.35).

Doping	E_p (nJ)	τ_o	τ_1	τ_ℓ
n-type	100	1180±20	36±3	250±30
	10	104±2	44±1	
	5	143±3	39±2	
p-type	10	790±30	1130±40	640±20
	5	121±5	720±30	390±20

Table 5.4: Lifetimes calculated using the mean HLI $\overline{\tau_{bulk}}$ for n-type ($21.9 \pm 0.4ns$) and p-type ($75 \pm 3ns$). n-type τ_ℓ was calculated using $\overline{\tau_1} = (39 \pm 2)ns$ and $\overline{\tau_1 || \tau_\ell} = (34 \pm 3)ns$ (see text for details). All lifetimes are reported in ns units.

Type	$E_p(nJ)$	τ_r	τ_{nr}
n-type	4000	60±1	33.5±0.5
	1000	96±1	29.0±0.3
p-type	4000	121±4	161±5
	1000	165±2	143±2
	100	196±4	134±3

Table 5.5: Radiative (τ_r) and nonradiative (τ_{nr}) lifetimes measured (ns units) from fits of the data in Figs. 5.14 and 5.15 using (3.2c) with (3.26).

approximately constant lifetimes, with average values of $\overline{\tau_{bulk}} = (21.9 \pm 0.4)ns$ for n-type and $\overline{\tau_{bulk}} = (75 \pm 3)ns$ for p-type. We assume that τ_{bulk} remains constant, and that the access to dilute defects varies with the Fermi-level position giving rise to a variable τ_o [81]. Under this assumption of constant τ_{bulk}, the trap-related time constants (τ_o, τ_1, and τ_ℓ) that become apparent at low-E_p (where $\Delta n < \rho_1$) can be decoupled from the measured $\tau_o || \tau_{bulk}$, $\tau_1 || \tau_\ell$, and $\tau_o \tau_1$ to give Table 5.4. In the n-type sample, the trap-emission rate was approximately constant with $\overline{\tau_1} = (39 \pm 2)ns$, and $\overline{\tau_1}$ was used to estimate $\overline{\tau_\ell} = (250 \pm 30)ns$. In the p-type sample, τ_1 is still undergoing some change, which is indicative of a broader density of states in the conduction band.

The cross-over from the trap-saturated domain ($\Delta n > \rho_1$, (3.26)) and the trap-dominated regime ($\Delta n < \rho_1$, (3.35)) gives us information about ρ_1, from which the effective energy level of the localized states (E_ℓ) can be calculated via the effective densities of states using (3.30). Both samples require fitting with (3.35) at $E_p = 10nJ$ and below, and I have used the estimated carrier densities at $10nJ$ to estimate ρ_1. In

the case of our n-type sample ($\rho_1 \rightarrow p_1$), we estimate that $\eta_o(10nJ) = \eta_o(100nJ)/10$, yielding $p_1 \sim 5 \times 10^{14} cm^{-3}$. For our p-type sample ($\rho_1 \rightarrow n_1$), the same assumptions yield $n_1 \sim 10^{15} cm^{-3}$. These two values give $(E_C - E_\ell) = (160 \pm 60) meV$ and $(E_\ell - E_V) = (250 \pm 60) meV$ in our p- and n-type samples, respectively. I have used $10\times\eta_o$ and $\eta_o/10$ as the range for our injection level estimates at E_p =10nJ to calculate generous uncertainties for E_ℓ.

Candidate intrinsic defect levels are EL11 ($(E_C - E_\ell) = 170meV$, [9]) in p-type and HL14 ($(E_\ell - E_V) = 250meV$, [9]) in n-type; however, incorporation of copper or nickel impurities ($(E_\ell - E_V) \sim 240meV$ and 210meV, respectively [87]) during growth is more probable in n-type, since HL14 was only observed after bombardment of GaAs with 1MeV electrons [9]. In contrast to the single level of nickel, copper impurities have four associated levels (at 23, 150, 240, and 510 meV above E_V, [87]), which could also explain why the low-E_p n-type results (Fig. 5.14) are less biexponential than the p-type (Fig. 5.15); however, this is not sufficient evidence to rule out nickel as the dominant localization level as other impurities and intrinsic defects can also play a role in localization. Identification arguments should not be pushed too far using E_ℓ, as it is a single effective parameter used to characterize a potentially broad density of localized-states associated with multiple defects.

The early transient observed in the low-E_p measurements is associated with the filling of traps, and is taken into account with an exponentially saturating lifetime characterized by $\tau_\times$. Measurement of $\tau_\times$ is only possible when a significant fraction of the initial minority carrier population is lost to the initial filling of localized states, which I have only observed in our 5 and 10nJ results. We observe the decrease of δ that we expect with increased E_p based on there being a smaller fraction of Δn_o being lost to initial trap-filling. The measured $\tau_\times$ suggest that the rate of initial trap filling increases with increased E_p.

At high E_p, fitting with (3.2c) and the new HLI model for $\eta(t)$ (3.26), I have measured $f(300K)$ in both samples allowing me to decouple τ_{nr} and τ_r from τ_{bulk} using

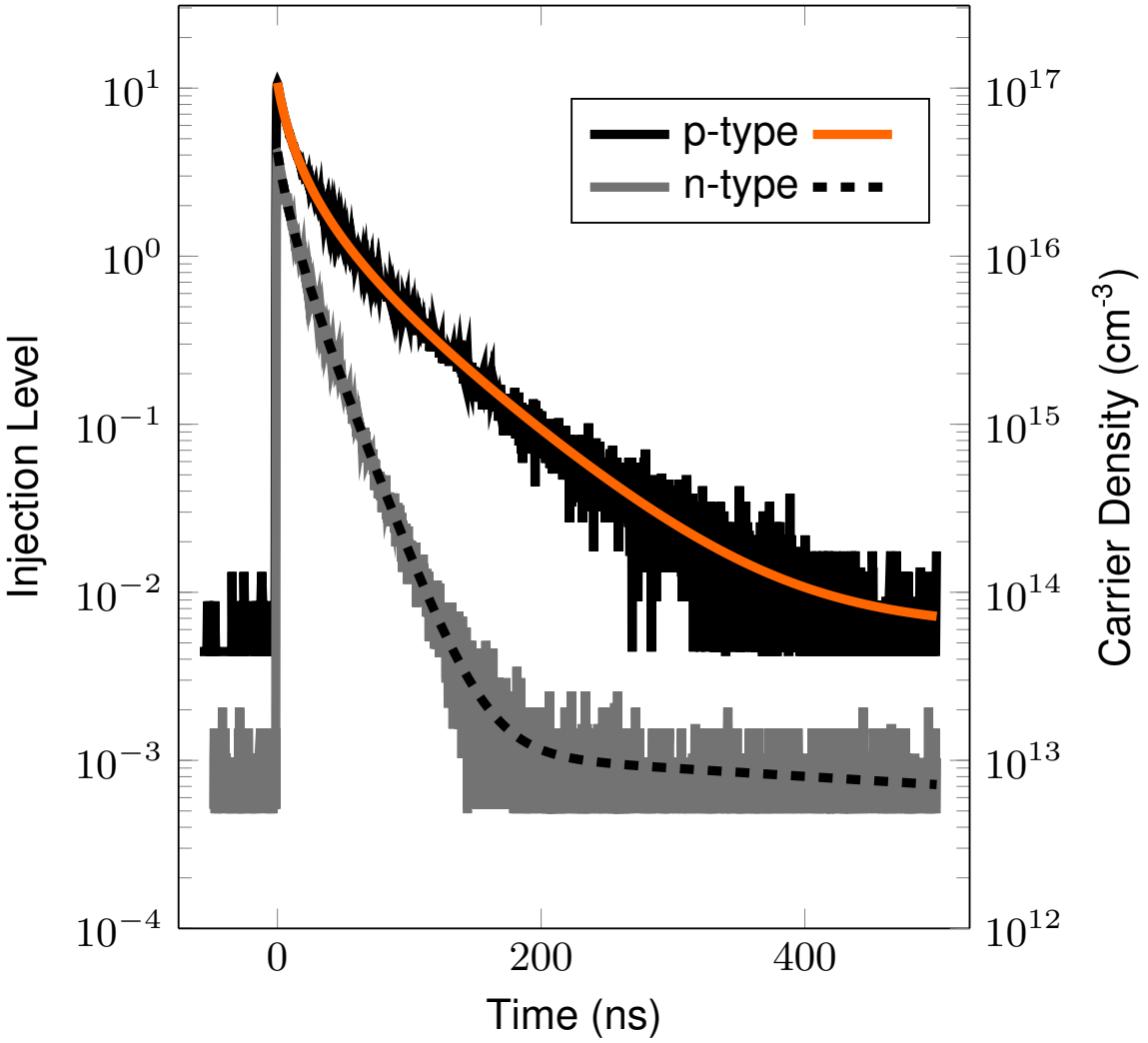

Figure 5.16: Injection level (carrier density) decay obtained by transforming TR-PLD using (3.3) and the measured $A_{PL}(n_o + p_o)^2$ for 500nm p- and n-type MBE-GaAs DH (InGaP passivated), doped to $10^{16}cm^{-3}$. Both experiments were performed at 300K using $4\mu J$ excitation pulses with 532nm wavelength. The time-resolution was 150ps (n-type) and 240ps (p-type), and the emission wavelength was 885nm. Lines (solid orange, and broken black) show fits using (3.26), where the nonlinearity provides estimation of the radiative efficiency ($f(T)$).

(3.13), and these results are shown in Table 5.5. I interpret the deviation in τ_{nr} as systematic error associated with assuming a constant SRH lifetime ($\tau_{LLI} \approx \tau_{HLI}$). For deep levels $\tau_{HLI}/\tau_{LLI} \to 1 + \sigma_{min}/\sigma_{maj} > 1$ [17], which is consistent with the observed increase in τ_{nr} with E_p. We should not be surprised to find that the measured radiative efficiency depends on the carrier-density conditions, since Shockley and Queisser [14] mention that only when a material is ideal (in the context of following the ideal diode equation exactly) will f remain constant.

A significant finding in this work is that even at these low doping levels ($10^{16} cm^{-3}$) the nonlinearity associated with recombination mechanisms (3.26) and emission-rate (3.2c) occur in a different Δn domain than the nonlinearity associated with localization effects ((3.35) with (3.32)), and so the two domains can be modelled independently to perform a full characterization. I have characterized the localized states near the minority bands, finding a larger localization energy near the valence band ($E_\ell - E_V = (250 \pm 60)$meV) than the conduction band ($E_C - E_\ell = (160 \pm 60)$meV). Of the intrinsic [9] and impurity [87] energy levels in GaAs, only E11 (an intrinsic defect, at $E_C - 0.17eV$ [9]) falls in the range of our experimental uncertainty for E_ℓ. The shallow level near the valence band suggests copper or nickel impurities, as discussed above. Neither defect identification is made with confidence, as we have no reason to assume dominant localization from a discrete energy level, and so E_ℓ should only be considered an effective parameter.

Experiments with strong excitation allow decoupling of η_o from the scaling parameter ($A_{PL}B(T)(n_o + p_o)^2$) in (3.2c), providing the missing calibration factor required to transform the arbitrary units of the TR-PLD signal into injection level units using (3.3), as shown in Fig. 5.16. Note that this a contactless, time-resolved measurement of injection level. The signal can also be multiplied by the doping level to provide carrier density decay. Experiments in the trap-dominated regime ($\Delta n < \rho_1$) are often biased by localization effects [80], leading to systematic error that is not present at high-E_p. Systematic overestimation of τ_{bulk} also arises in the commonly practiced

small-perturbation approach because of delayed trap-state emission. Careful bias-light optimization can be used to deactivate trap-states [17]; however, this requires additional experimental complexity, and has been shown to only reduce the influence of trap-emission [41]. By using models that accurately describe the injection level dependence of the lifetime (in our case, (3.2c) with (3.26)), bulk-lifetime measurements can be made with faster acquisition time (stronger signal in HLI) and increased accuracy of measured recombination characteristics relevant to quasi-equilibrium operating conditions (less prone to trap-emission bias). The τ_{bulk} measured under HLI conditions using (3.26) can be used to decouple the trap-parameters (τ_o, τ_1, and τ_ℓ) measured from fits using (3.35) with (3.32).

Using the high-power laser and new models ((3.26), (3.35) and (3.32)), I have shown that TR-PLD is independent of trapping for sufficiently high E_p ($\Delta n > \rho_1$) while low-E_p dynamics are heavily influenced by traps ($\Delta n < \rho_1$). Results that I have obtained from 500nm p- and n-type ($10^{16} cm^{-3}$) GaAs DHs grown using MBE demonstrate robust fitting results using our analytical models in both $\Delta n > \rho_1$ ((3.2c) with (3.26)) and $\Delta n < \rho_1$ (3.35) domains. For applications that operate near equilibrium (low-power logic, low-noise amplifiers, etc.), (3.35) can be used to parametrize trapping processes. In applications with high excess carrier density, the HLI model (3.26) is often valid for direct bandgap semiconductors with deep-level defects. Of particular importance to the field of photovoltaics, (3.26) allows for the measurement of the radiative efficiency that is required for calculation of the maximum Shockley and Queisser solar cell efficiency [14] possible for a given material quality.

5.3 Temperature-Dependent Lifetime Analysis

5.3.1 CZ-GaAs (n-type)

In this section, I apply approximation (3.20) to measure the temperature-resolved bulk-lifetime spectrum ($\tau_{bulk}(T)$) in an unpassivated n-type ($2 \times 10^{18} cm^{-3}$) CZ-GaAs

wafer. I will demonstrate that the radiative efficiency ($f(T)$), and E_∞ of the lifetime-limiting defect can be measured by analyzing $\tau_{bulk}(T)$, and that (3.20) facilitates this analysis and gives confidence in the measured bulk lifetimes being independent of the surface recombination velocity.

To test the accuracy of (3.20) with variation in temperature, TR-PLD experiments were performed at temperatures ranging from 77K to 700K. The TR-PLD data is shown in Figs. 5.17-5.20, along with fits using both (3.19) and (3.20) to account for surface-recombination and axial-diffusion. The solid lines show the results of the nonlinear least-squares (trust-region) fit of (3.19) to the measured data. The same data was also linearized through multiplication by the square root of time (i.e. $y \rightarrow \ln(I_{PL}\sqrt{t})$), and fit with a simple two-parameter linear least squares fit. The results of the linear fit were substituted into (3.20), and the results are plotted as dotted lines.

Table 5.6 shows the lifetimes measured at each temperature using both (3.19) and (3.20), indicating that the lifetimes extracted using either method agree to within the 95% confidence intervals of the fit. To further illustrate this, a histogram of 350 lifetimes obtained using both methods is shown for 300K in Fig. 5.21. The fits, histograms and measured lifetimes show excellent agreement between the results obtained using (3.19) and (3.20).

$T(K)$	$\tau_{nonlinear}(ns)$	$\tau_{linear}(ns)$
77	45 ± 8	44 ± 3
100	77 ± 3	76 ± 2
200	180 ± 2	181 ± 2
300	302 ± 8	302 ± 7
400	104.5 ± 0.7	105.1 ± 0.7
500	48.2 ± 1.6	48.3 ± 0.9
600	28.3 ± 1.9	28.4 ± 1.0
700	15 ± 11	15 ± 2

Table 5.6: Lifetimes (with 95% confidence intervals) measured from data in Figs. 5.17-5.20 using non-linear (3.19) and linear (3.20) fits.

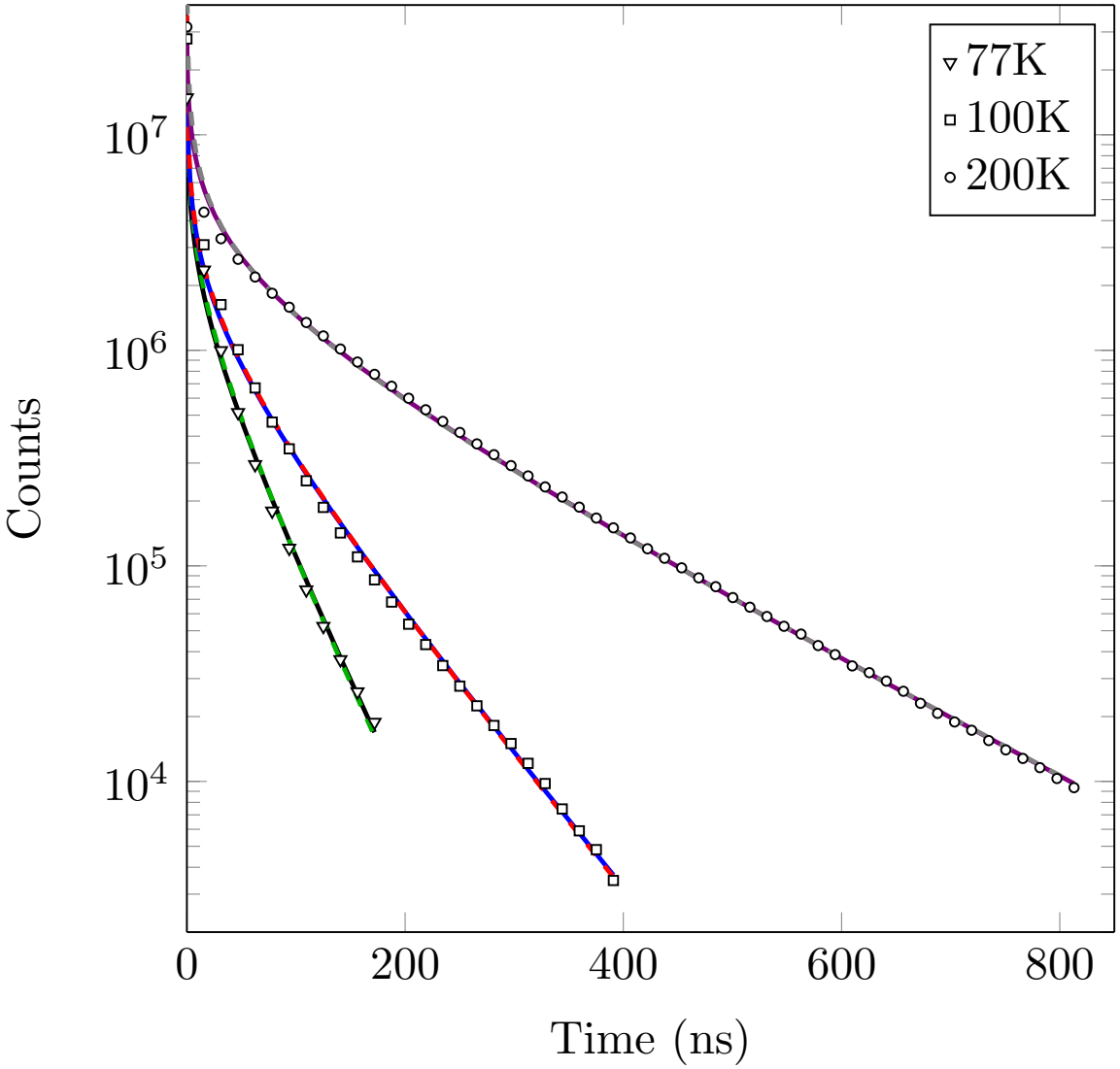

Figure 5.17: TR-PLD measurements with n-CZ-GaAs. Solid lines (black, blue, purple) show nonlinear fits (3.19), and dotted lines (green, red, and yellow) show linear fits (signal multiplied by $\sqrt{t}$ and linearly fit on log-scale) for 77K, 100K, and 200K (respectively). The bin-width was 15.6ns, the emission wavelengths were 870nm, and excitation was at 532nm.

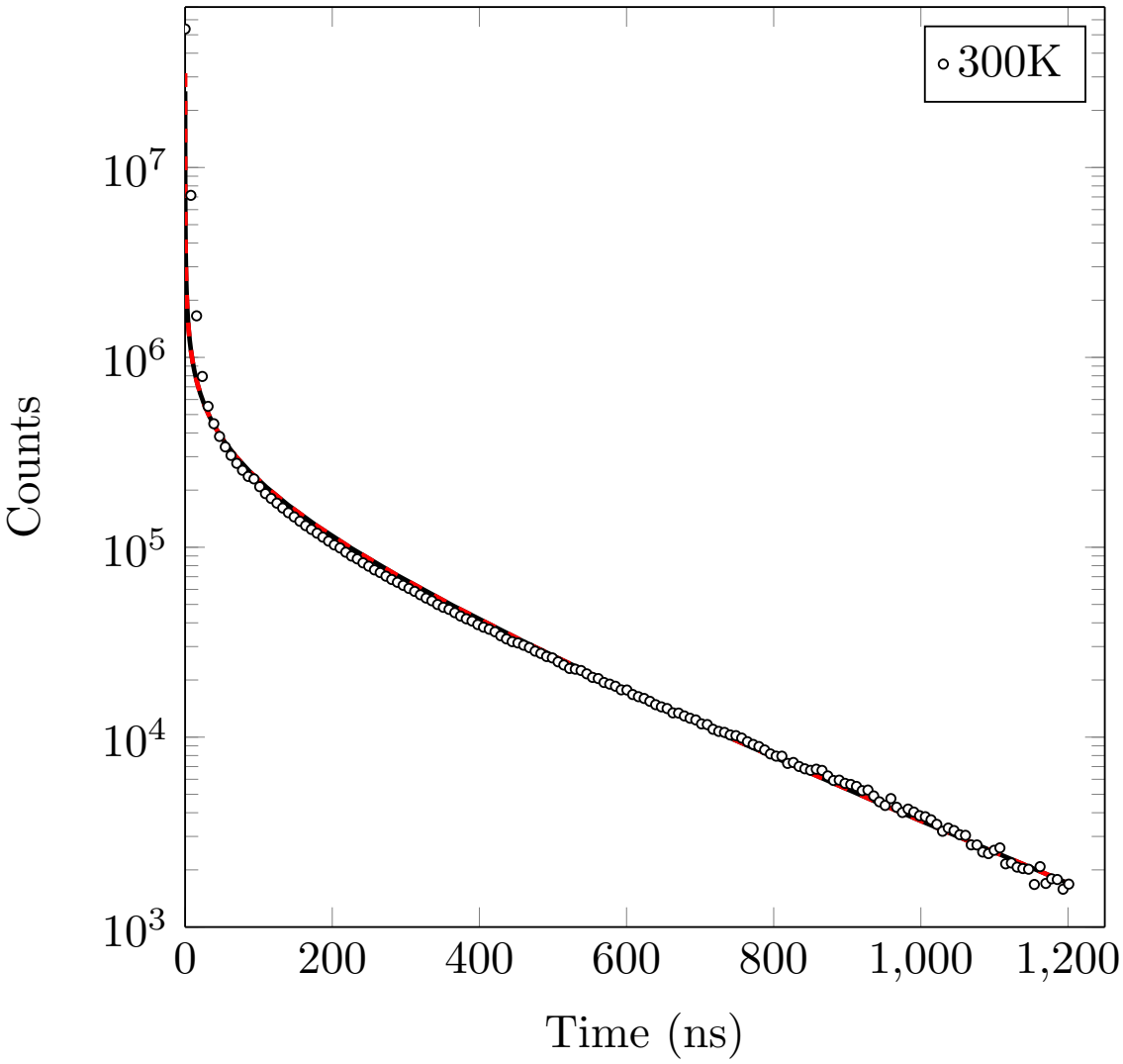

Figure 5.18: TR-PLD measurement with n-CZ-GaAs. The solid black line show nonlinear fits (3.19), and dotted lines (green, red, and yellow) show linear fits (signal multiplied by $\sqrt{t}$ and linearly fit on log-scale) for 300K. The bin-width was 15.6ns, the emission wavelength was 870nm, and excitation was at 532nm.

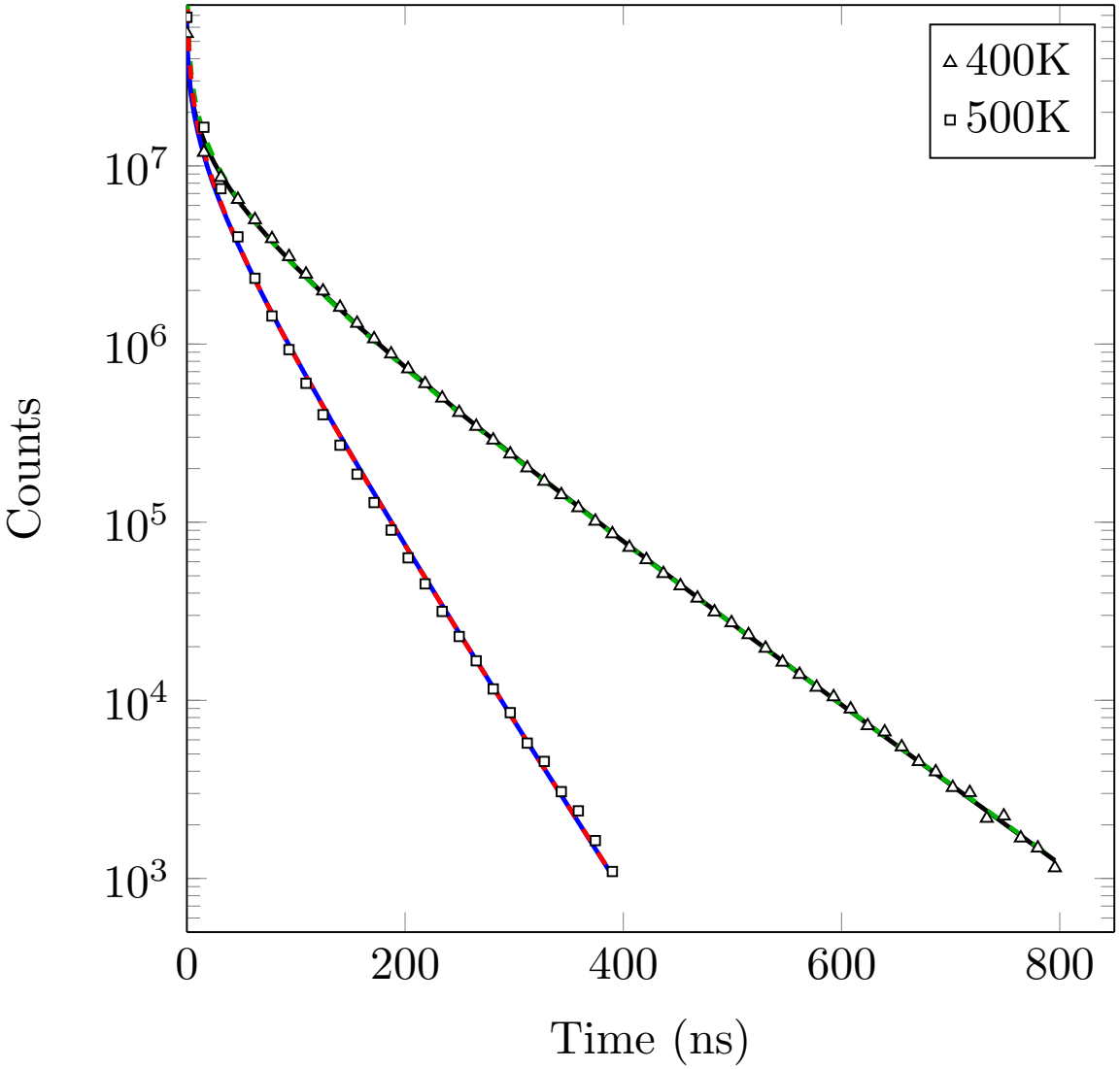

Figure 5.19: TR-PLD measurement with n-CZ-GaAs. Solid lines (black and blue) show nonlinear fits (3.19), and dotted lines (green, red, and yellow) show linear fits (signal multiplied by $\sqrt{t}$ and linearly fit on log-scale) for 400K and 500K (respectively). The bin-width was 15.6ns, the emission wavelengths were 870nm (400K) and 900nm (500K), and excitation was at 532nm.

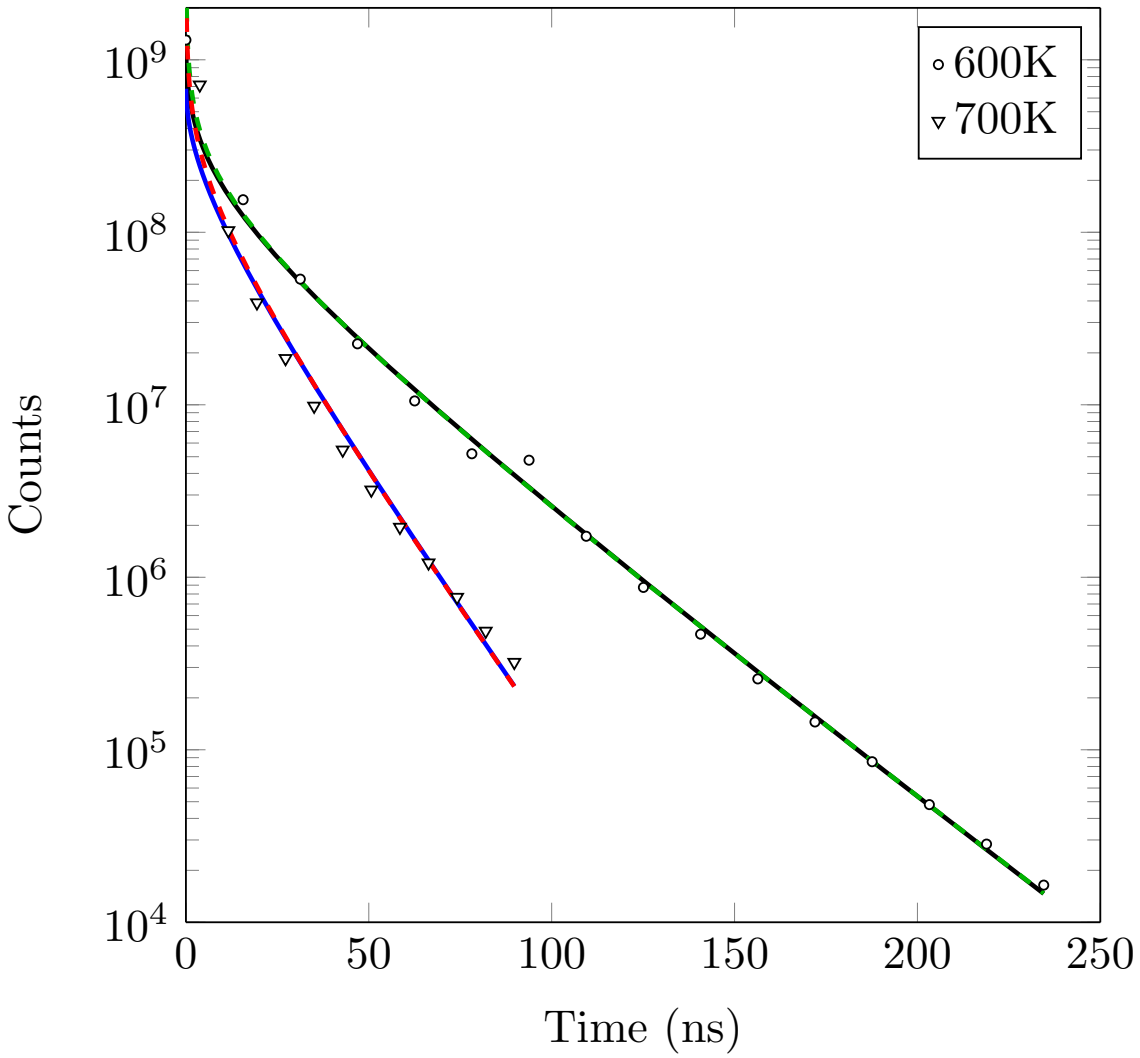

Figure 5.20: TR-PLD measurement with n-CZ-GaAs. Solid lines (black and blue) show linear fits (signal multiplied by $\sqrt{t}$ and linearly fit on log-scale) for 600K and 700K (respectively). The bin-width was 15.6ns, the emission wavelengths were 950nm (600K) and 970nm (700K), and excitation was at 532nm.

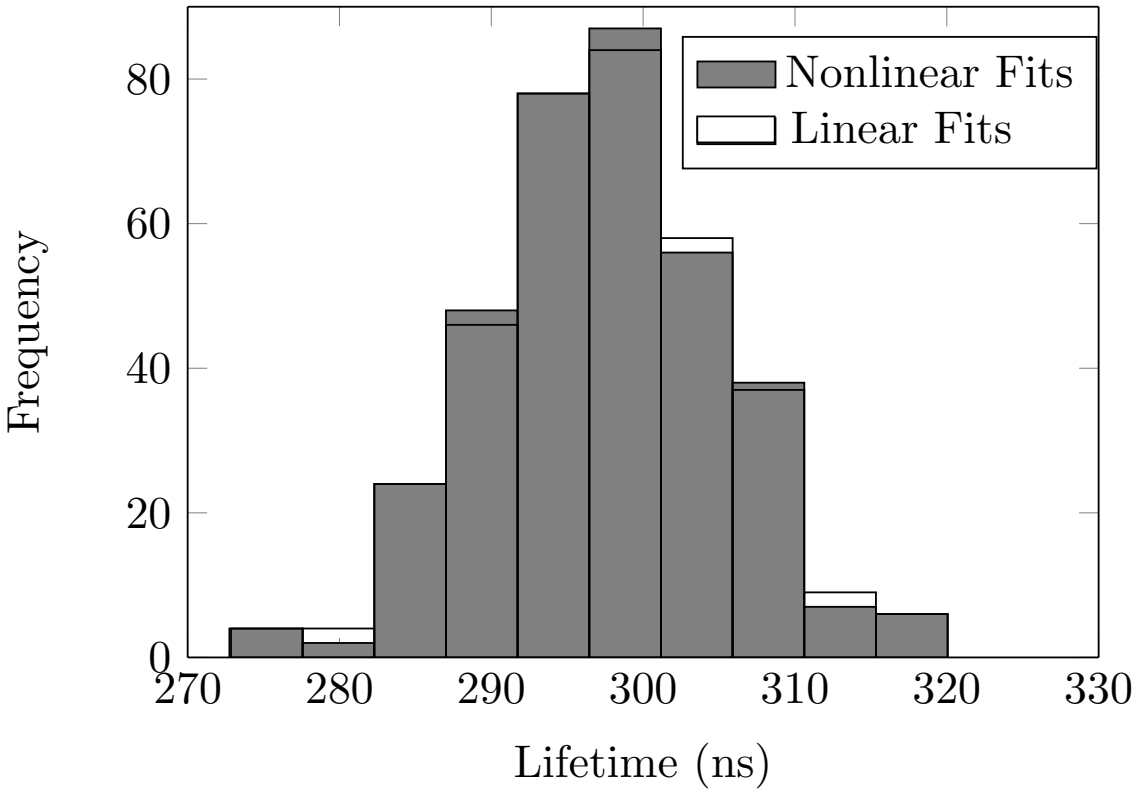

Figure 5.21: Histogram of 350 lifetimes measured in a 800ns window with ∼200,000 photons. The hollow boxes show the lifetimes obtained using the linear fit (3.20) on uncropped linearized data, while the grey boxes show fits using (3.19). The mean of lifetimes measured using either technique was $298ns$ with a standard deviation of $8ns$. These samples were summed to form the data shown in Fig. 5.18.

A_r (cm^6Kns^{-1})	E_∞ (meV)	$N_T\sigma_o$ (cm^{-1})	$r_\sigma = \frac{\sigma_\infty}{\sigma_o}$
$(5 \pm 2) \times 10^{-26}$	160 ± 40	0.08 ± 0.07	180 ± 100

Table 5.7: Defect parameters (with %95 confidence intervals) measured from a weighted fit of the results in Table 5.6 using (3.13) with (3.7) and (3.11b).

The measured $\tau_{bulk}(T)$ are plotted in Fig. 5.22, along with the fit using (3.13) with (3.7) and (3.11b). Since this is an n-type material with moderate doping, LLI conditions are assumed where capture of minority carriers (holes) limits nonradiative recombination ($\tau_{nr} = \tau_p$). The estimated values of τ_z, τ_{FS}, and τ_ρ are also plotted, illustrating that the required $\{\tau_z, \tau_{FS}\} \ll \tau_{bulk} \ll \tau_\rho$ conditions of approximation (3.20) are satisfied from 77-700K. The results of the fit to $\tau_{bulk}(T)$ are shown in Table 5.7. The wide temperature sweep with $\Delta T = 100K$ resolution allows estimation of the radiative efficiency ($f(T)$) from the fits. Calculations of $f(T)$ with 95% confidence intervals using (3.14) with the measured τ_{nr} and τ_r are plotted in Fig. 5.23.

To improve the accuracy and precision in E_∞, a measurement with $\Delta T = 10K$ resolution was made from 500-600K. By multiplying the lifetime by $\sqrt{T}$, the effects of the changing thermal velocity ($v_{th} = \sqrt{3k_BT/m^*}$) can be decoupled from the temperature-dependence of (3.11). The resulting $\ln(\tau_{bulk}\sqrt{T})$ data is linearly fit (with respect to $1000/T$) in Fig. 5.24, resulting in $E_\infty = (261 \pm 7)meV$. The measured E_∞ is within the range (0 to $560meV$) expected for MPE capture [11].

The lifetime-limiting defect must have a low value of σ_o for hole-capture, in order to have such high E_∞. Data from [8, 9, 11] indicate hole-capture via EL2 could yield such a large E_∞ value. The high E_∞ value rules out all other defects in GaAs, since the σ_p of these defects measured using DLTS cannot undergo this large exponential increase [8, 9, 11]. Using $\overline{\sigma}_{o,p} = (0.93 \pm 0.07) \times 10^{-18}cm^2$ from [8] and the measured σ_o/σ_∞ ratio (Table 5.7), we estimate $\sigma_\infty = (1.7 \pm 0.9) \times 10^{-16}cm^2$. This measured σ_∞ is close to the observed range of $\sigma_\infty = (10^{-16} - 10^{-14})cm^2$ for defects in GaAs [9, 11]. Using $\overline{\sigma}_{o,p}$ and $N_t\sigma_o$, the estimated trap density is $N_t = (9 \pm 8) \times 10^{16}cm^{-3}$, which is

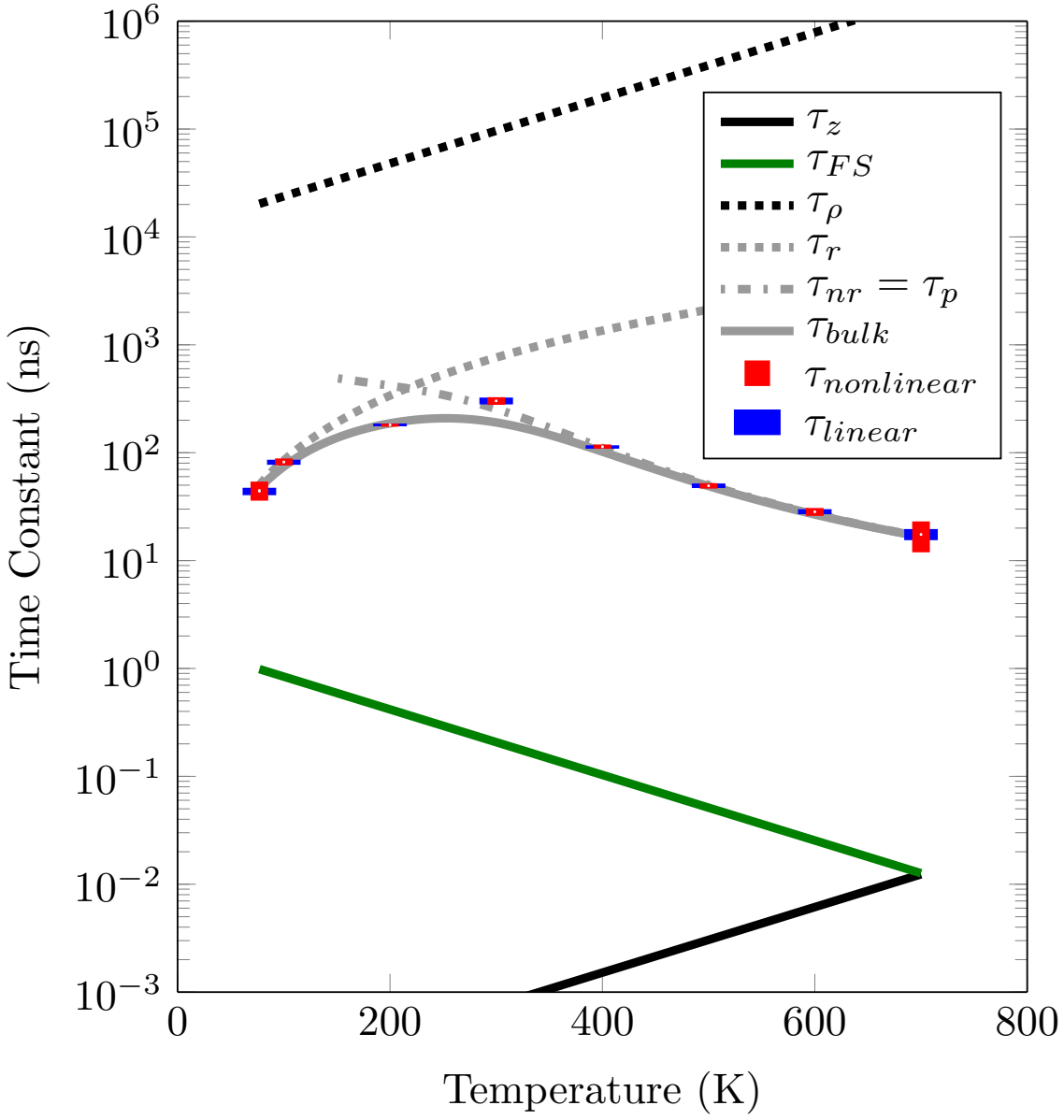

Figure 5.22: Lifetimes are plotted with rectangles of heights that correspond to their 95% confidence intervals. Also shown are the estimated time constants for the diffusive and surface recombination processes in this experiment (τ_z, τ_ρ, and τ_{FS}). The surface recombination velocity and absorption coefficient were assumed constant with respect to temperature, using 300K literature values of $S = 10^6 cm/s$ [7] and $\alpha = 80000 cm^{-1}$ [6]. The temperature-independent 532nm excitation beam width was $\sigma_r = 2mm$. The bulk lifetime shown (τ_{bulk}) is the fit using (3.7) and (3.12), shown with radiative (τ_r) and nonradiative ($\tau_{nr} = \tau_p$) contributions.

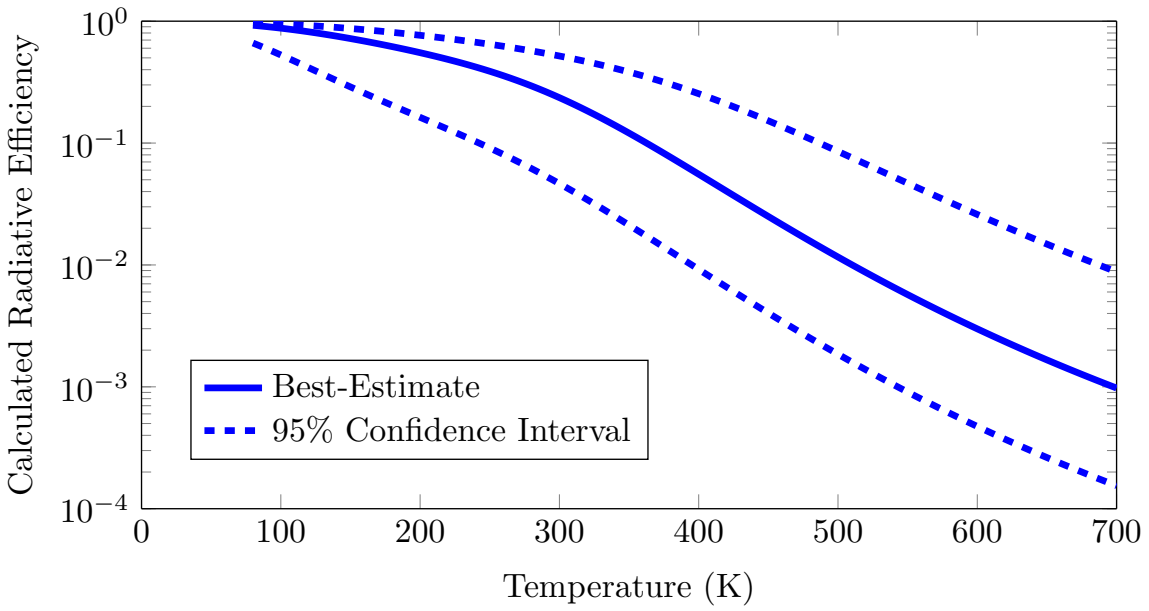

Figure 5.23: The radiative efficiency ($f(T)$) has been calculated using (3.14) and the $\tau_{nr} = \tau_p$ and τ_r measured from the fits to TR-PLD from 77-700K. The dotted lines show the 95% confidence interval of this estimate.

consistent EL2 densities observed in CZ-grown GaAs on the order of $10^{16} cm^{-3}$ [56].

By analyzing TR-PLD from 77-700K, I have demonstrated that diffusion and surface recombination in thick unpassivated materials can be decoupled from using approximation (3.20). This is the first time that this model has been proposed to be valid at all times for TR-PLD from thick, unpassivated materials, and I have shown experimentally that accurate τ_{bulk} results are obtained in comparison with those obtained by fitting with (3.19). This allows the use of above bandgap excitation (i.e. one-photon absorption) to study thick unpassivated materials, and has facilitated these temperature-dependent lifetime measurements. With accurate bulk-lifetime measurement, the radiative efficiency was measured, and $E_\infty = (261 \pm 7) meV$ was measured for σ_p of lifetime-limiting defect in the bulk. The high E_∞ value rules out all characterized σ_p, except for that of EL2 [8, 9, 11]. Evidence supporting identification of EL2 as the lifetime-limiting defect in n-CZ-GaAs is discussed further in Section 6.2.

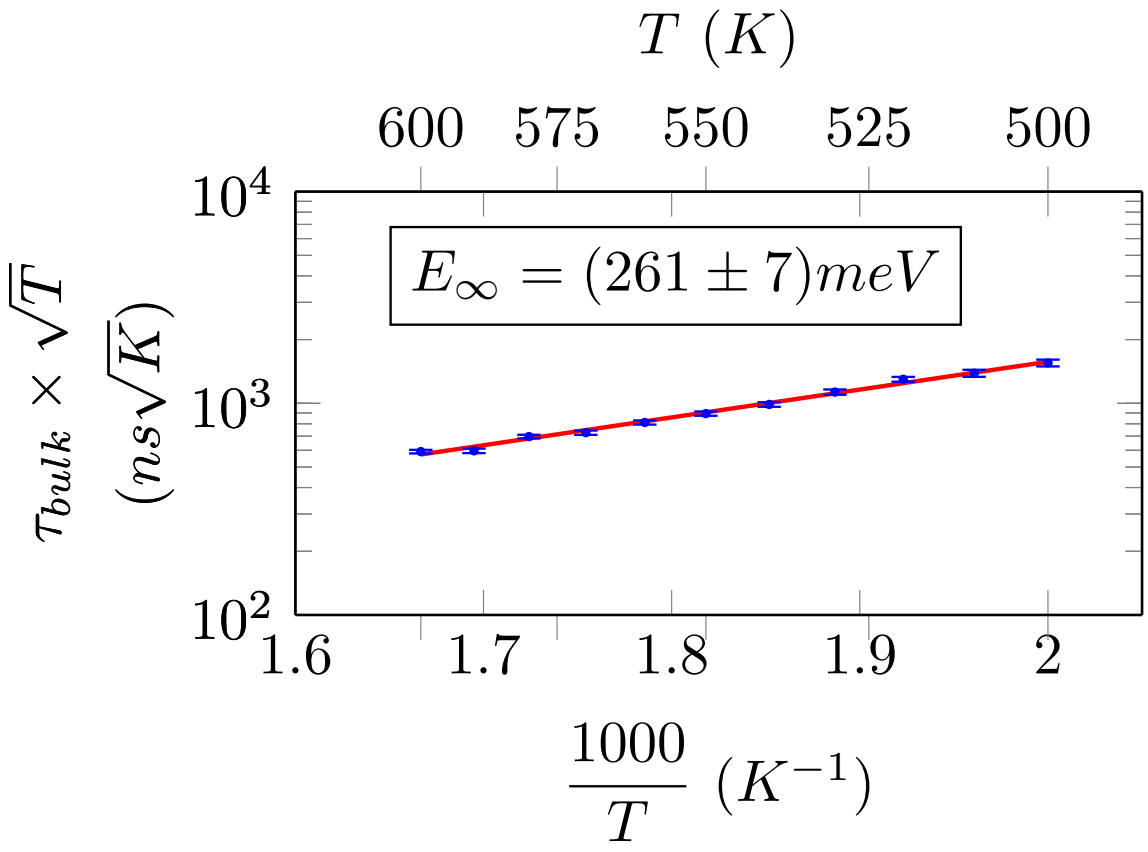

Figure 5.24: Measurement of E_∞ in $2 \times 10^{18} cm^{-3}$ n-type CZ-GaAs with $\Delta T = 10K$ resolution from 500-600K. The measured τ_{bulk} were obtained by fitting TR-PLD with (5.2) to account for trap-emission, axial-diffusion, and surface-recombination. The longer lifetime associated with trap-emission remained constant at $(1.2 \pm 0.1)\mu s$ for these fits. The pulse energy was 40nJ, and PL was observed at the peak emission wavelength.

5.3.2 MBE-GaAs

I have performed TR-PLD measurements on n- and p-type ($10^{16}cm^{-3}$) MBE-GaAs DHs in order to measure the radiative efficiency ($f(T)$) from temperature-dependent τ_{bulk} fit using (3.13) with (3.7) and (3.12). Fig. 5.25 shows examples of fits to TR-PLD data using (3.2c) with (3.26) from 100-700K. The TR-PLD data clearly shows that the nonlinearity associated with radiative recombination (3.26) is most prominent at 100K, indicating high $f(T)$ at these low temperatures. As both samples are heated the TR-PLD becomes more linear and τ_{bulk} increases. The increase in lifetime is consistent with the behaviour (3.7) of the τ_r, and the increased linearity indicates a reduction in $f(T)$ resulting from the decrease in τ_{nr}. Above 300K, we observe that the lifetime begins to decrease, indicating that nonradiative recombination has become dominant.

Fig. 5.26 shows the lifetimes measured from TR-PLD using the above method (with $\Delta T = 5K$), as well as the fits to τ_{bulk} obtained using (3.13) with τ_r from (3.7) and τ_{nr} (3.12). Note that the lifetime undergoes an abrupt exponential drop in both samples, and that the lifetimes drop at a similar rate with temperature. This drop due to the exponential increase in σ, parametrized by E_∞. Parameters measured from these fits are shown in Table 5.8, and the E_∞ measured in both samples falls in the range of $(255 \pm 5)meV$. The common E_∞ indicates that both samples are limited by nonradiative recombination assisted by a common defect.

From the τ_{nr} and τ_r measured in the fit, the radiative efficiency has been calculated, and is plotted with 95% confidence intervals in Fig. 5.27. The lifetimes are radiatively

	$A_r \cdot 10^{32}$ $(cm^6 K n s^{-1})$	$N_t\sigma_o \cdot 10^3$ (cm^{-1})	E_∞ (meV)	r_σ
n	1.9±0.3	1030±60	260±10	700±200
p	3.0±0.6	300±50	250±10	1700±200

Table 5.8: Parameters measured from fits shown in Fig. 5.26. $N_t\sigma_o$ have been calculated assuming hole-limited capture. To convert to electron-limited values, $N_t\sigma_o$ should be multiplied by 0.789.

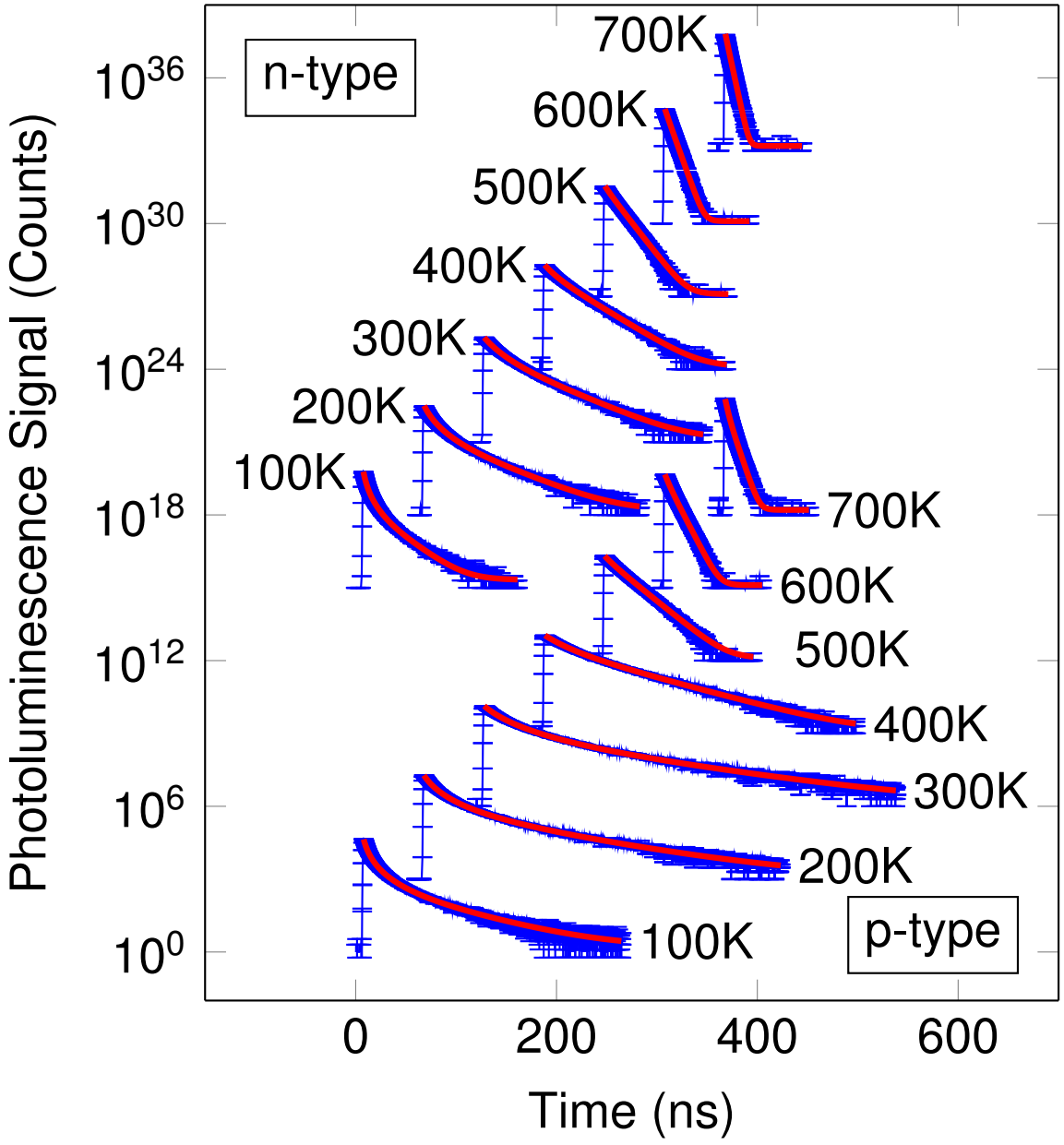

Figure 5.25: Example TD-TR-PLD raw data (10^6 total counted photons) is shown (blue) with fits (red) used to obtain τ_{bulk} plotted in Fig. 5.26. The 100K p-type example is shown in counts, while the other examples have been multiplied by scaling factors (powers of 10^4) and shifted (by 60ns increments) for visual clarity. The fit-period was 900ns; however, data has been cropped 50ns after the data first reaches 1 count. Poisson counting statistics provide error bar length equal to the square root of the number of counts. The time resolution was 240ps, and the emission was observed at the peak wavelength. Excitation was at 532nm.

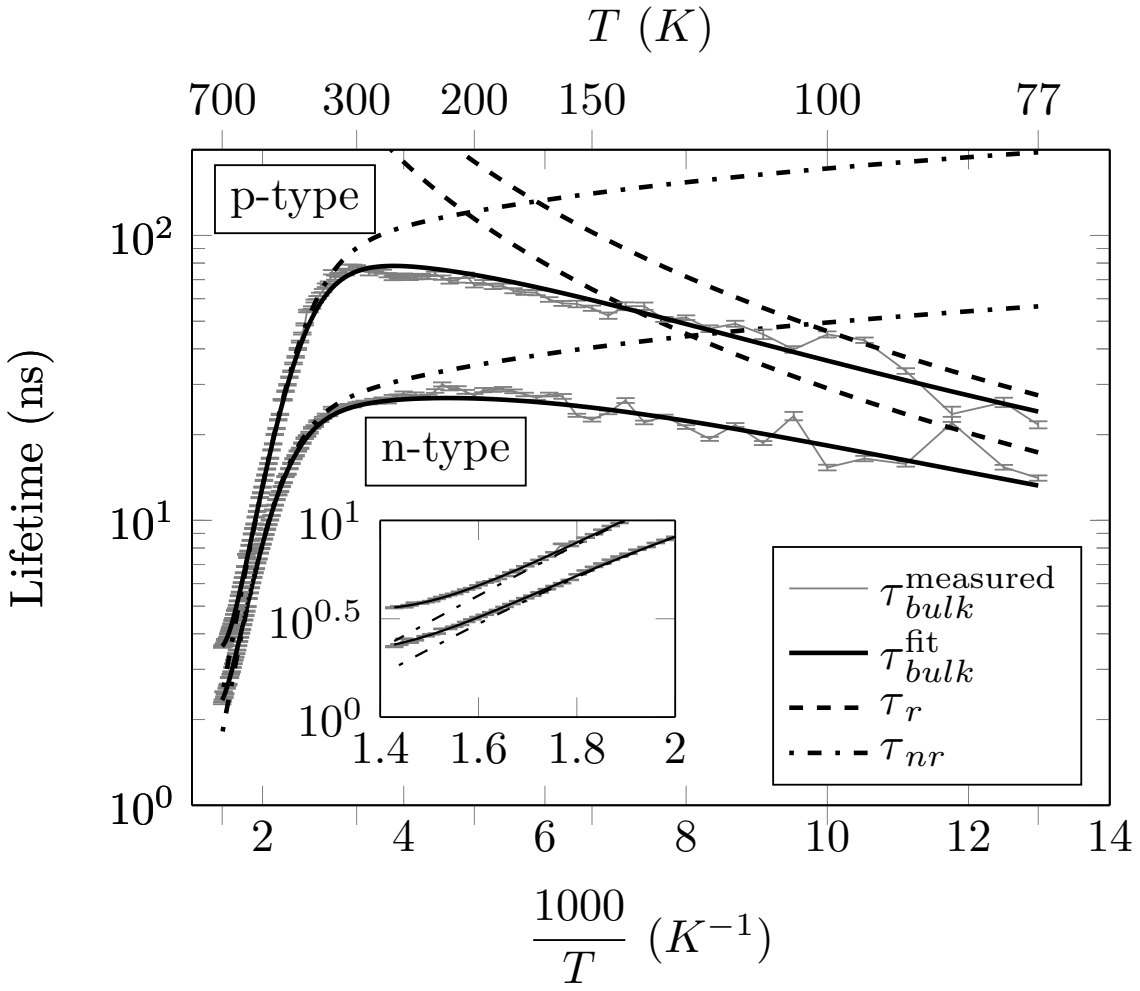

Figure 5.26: The temperature-dependence of τ_{bulk} measured by fitting TR-PLD with $I_{PL}(t)$ from (3.2c) and $\eta(t)$ from (3.26) is fit using (3.13) with τ_r from (3.7) and τ_{nr} from (3.12). Measured fit parameters are listed in Table 5.8. The inset shows a magnified view of the Arrhenius increase onset for 500-700K.

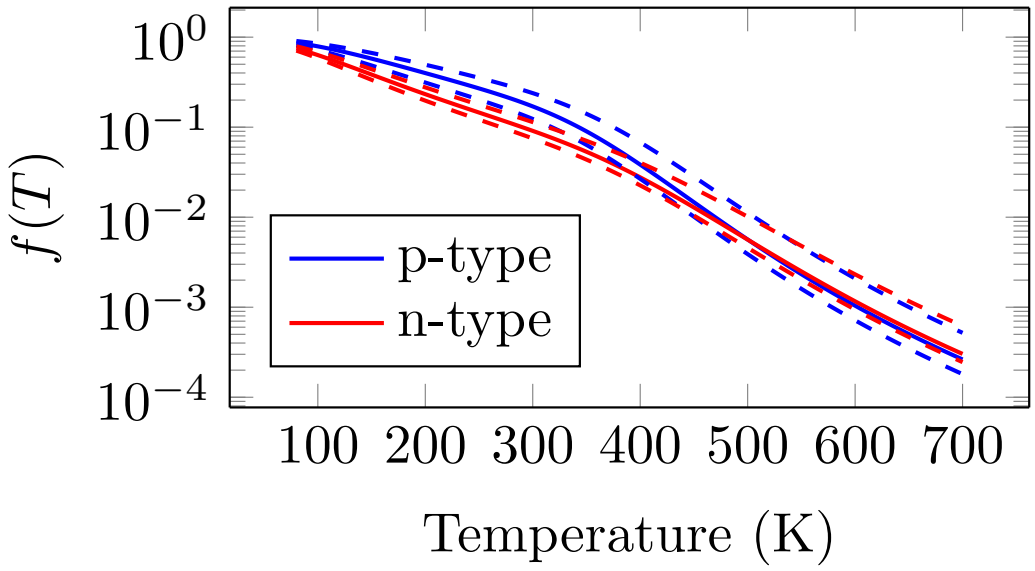

Figure 5.27: From the temperature-dependent lifetime fits to τ_{bulk} obtained by fitting TR-PLD with (3.2c) and $\eta(t)$ from (3.26), the radiative efficiency ($f(T)$) has been calculated. The dashed lines show the 95% confidence interval.

limited at low temperature, but nonradiative recombination is competitive at room temperature in both n-type ($f(300K) = (9 \pm 2)\%$) and p-type ($f(300K) = (17 \pm 6)\%$).

Since both τ_{bulk} and $f(T)$ are temperature-dependent, the time-and temperature-dependence of TD-TR-PLD data can analyzed in parallel using a surface fit. To fit TD-TR-PLD, (3.2c) is used with $\eta(t)$ from (3.26), $f(T)$ from (3.14), $\tau_{bulk}(T)$ from (3.13), $\tau_r(T)$ from (3.7) and $\tau_{nr}(T)$ from (3.11b). Substitution of these equations into (3.2c) results in a fitting function that depends only on time, temperature, η_o, A_r, $N_t\sigma_o$, E_∞, and r_σ. These surface fits to TD-TR-PLD are shown in Figs. 5.28 and 5.29. The fit-parameters obtained from the surface fits are shown in Table 5.9, demonstrating good agreement with the parameters obtained from fitting the time-dependence ((3.2c) with (3.26)) and temperature-dependence (using (3.13) with (3.7) and (3.12)) in series. Since the parallel fitting method of TD-TR-PLD provides consistent results with higher precision, I report the final values from the surface-fitting while presenting the results from serial fitting in order to provide deeper intuition. Fig. 5.30 shows τ_{bulk}, τ_r, and τ_{nr} calculated from the surface fits to TD-TR-PLD.

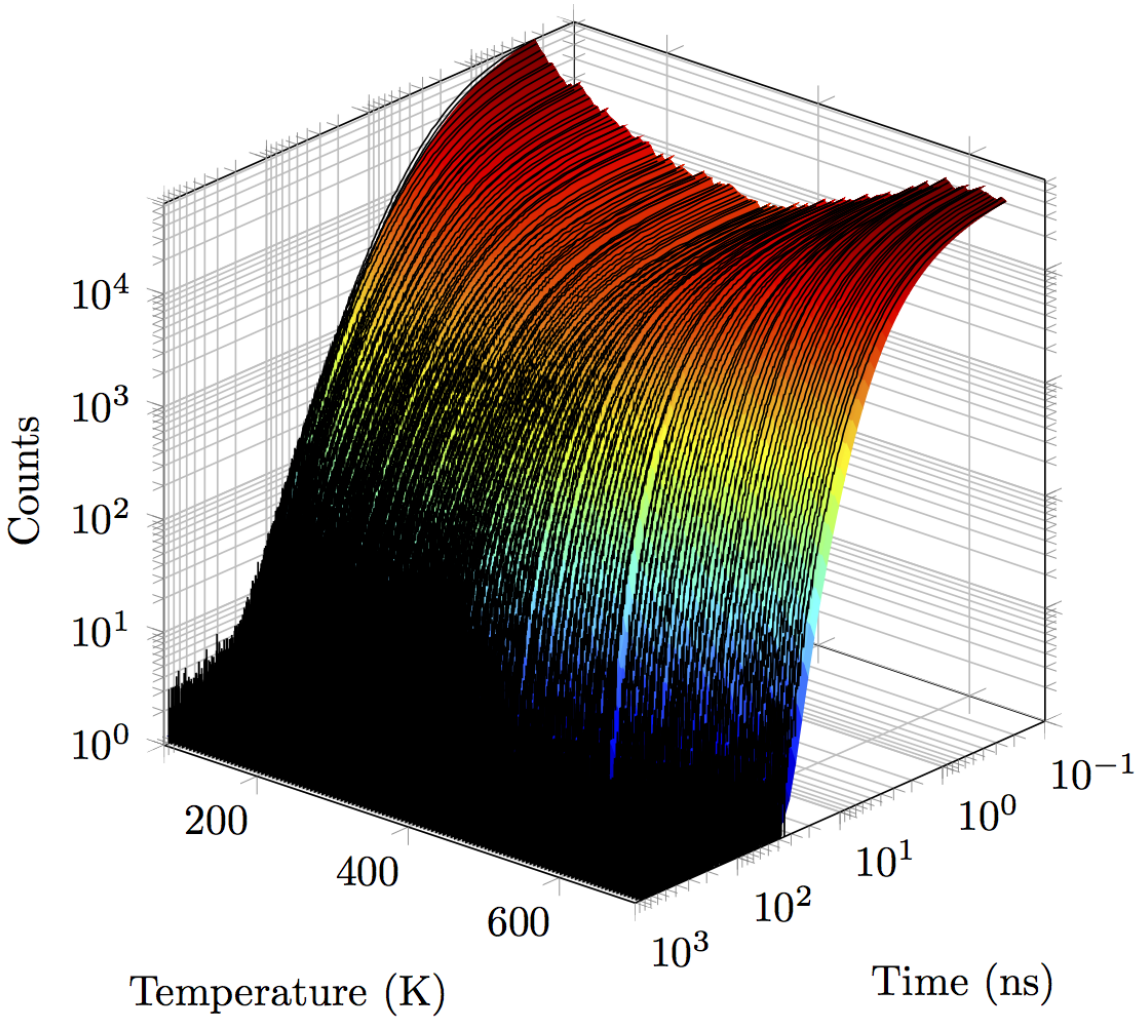

Figure 5.28: Measured (p-type) TD-TR-PLD (black lines) with (unweighted) nonlinear surface fit (coloured surface) using (3.2c) with $\eta(t)$ from (3.26), $f(T)$ from (3.14), $\tau_{bulk}(T)$ from (3.13), $\tau_r(T)$ from (3.7) and $\tau_{nr}(T)$ from (3.11b).

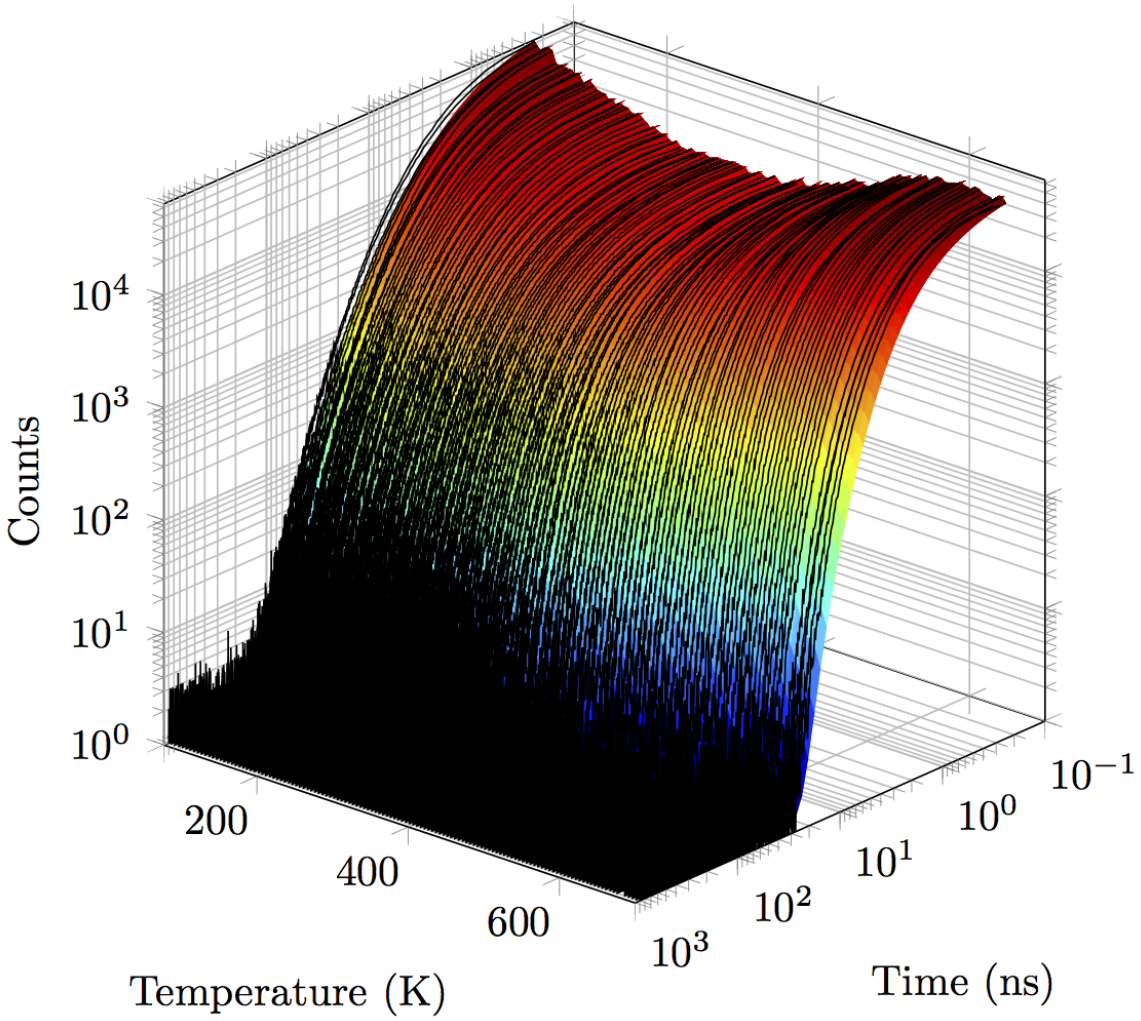

Figure 5.29: Measured (n-type) TD-TR-PLD (black lines) with (unweighted) nonlinear surface fit (coloured surface) using (3.2c) with $\eta(t)$ from (3.26), $f(T)$ from (3.14), $\tau_{bulk}(T)$ from (3.13), $\tau_r(T)$ from (3.7) and $\tau_{nr}(T)$ from (3.11b).

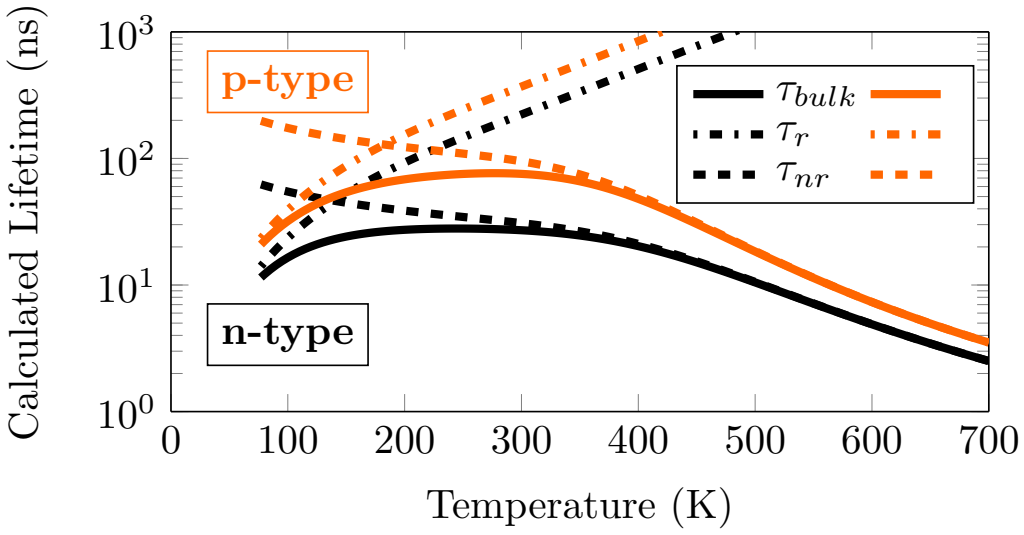

Figure 5.30: Plot of the bulk-lifetime (solid lines) calculated from the fit parameters extracted from the surface fits to TD-TR-PLD using (3.2c) with $\eta(t)$ from (3.26), $f(T)$ from (3.14), $\tau_{bulk}(T)$ from (3.13), $\tau_r(T)$ from (3.7) and $\tau_{nr}(T)$ from (3.11b). Calculated lifetimes are shown with radiative and non-radiative contributions (broken lines) for p-type (orange) and n-type (black).

From these surface-fits to TD-TR-PLD, $f(T)$ has been calculatedusing (3.14) from the measured τ_{nr} and τ_r with higher precision (<5% for 77-700K, and <1% for T <325K), and is plotted in Fig. 5.31. The $f(300K)$ measured using this fitting method is (12.2±0.2)% in n-type, and (20.5±0.2)%. This improved precision highlights the value of fitting TD-TR-PLD as a surface, as challenging as its results may be to illustrate. The measured values of A_r from these fits yield room-temperature radiative-recombination coefficients (B(300K)) of $(4.48 \pm 0.01) \times 10^{-10} cm^3/s$ (n-type) and $(2.71 \pm 0.01) \times 10^{-10} cm^3/s$ (p-type), which are consistent with literature values in the range of $(1 \sim 5) \times 10^{-10} cm^3/s$ [47, 51]. The consistency in $B(300K)$ provides confidence in the room-temperature estimation of τ_r and $f(300K)$. The low radiative-efficiency in these samples reflects the long τ_r that results from the low ($< 10^{17} cm^{-3}$) doping-level, and should not be interpreted as being a result of poor material quality as the measured $f(T)$ are consistent with those expected based on literature results at $10^{16} cm^{-3}$ doping level in both p-type [88] and n-type [89] GaAs.

	$A_r \cdot 10^{32}$ $(cm^6 K n s^{-1})$	$N_t \sigma_o \cdot 10^3$ (cm^{-1})	E_∞ (meV)	r_σ	η_o
n	1.53±0.01	930±2	257.5±0.9	517±8	4.60±0.05
p	2.53±0.01	292±1	259.3±0.6	1320±10	7.74±0.06

Table 5.9: Parameters from surface-fitting of TD-TR-PLD using models for τ_{bulk} (3.13) with τ_r (3.7) and τ_{nr} (3.12) substituted into $I_{PL}(t)$ (3.2c) using $\eta(t)$ from (3.26). Higher-precision results are consistent with those (Table 5.8) obtained from fitting $I_{PL}(t)$ and $\tau_{bulk}(T)$ in series (Figs. 5.25 and 5.26). $N_t\sigma_o$ have been calculated assuming hole-limited capture. To convert to electron-limited values, $N_t\sigma_o$ should be multiplied by 0.789.

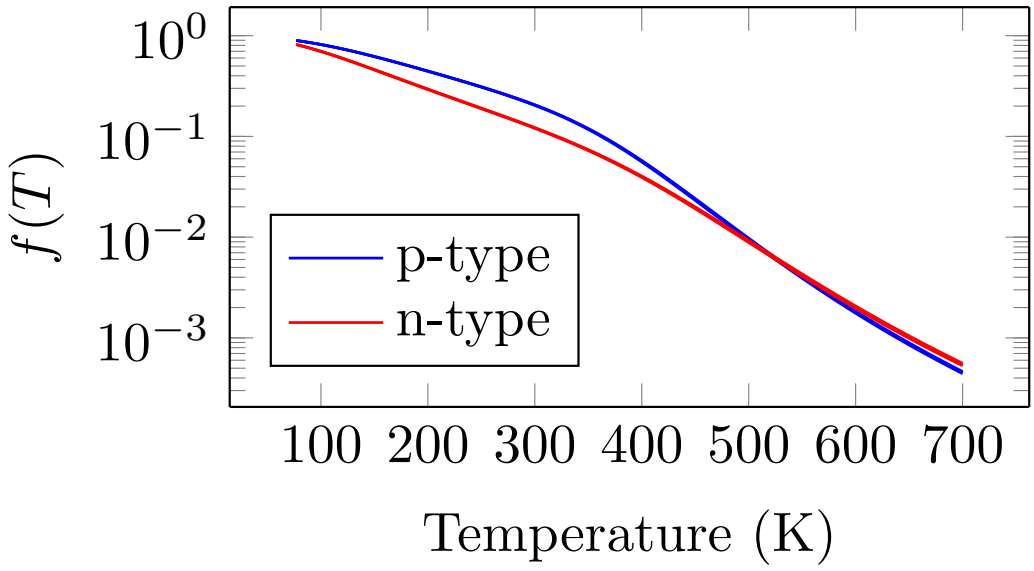

Figure 5.31: Radiative efficiency ($f(T)$) calculated from surface-fitting of TD-TR-PLD using models for τ_{bulk} (3.13) with τ_r (3.7) and τ_{nr} (3.12) substituted into $I_{PL}(t)$ (3.2c) using $\eta(t)$ from (3.26). Note that the dashed lines that show the 95% confidence interval are no longer visible (see Fig. 5.27), as the uncertainty is less than 5% of $f(T)$ from 77 to 700K, and below 1% for $T \leq$325K.

The common value of E_∞ value implies that HLI-recombination is limited above 300K by the capture of a single carrier-type (i.e. either electrons or holes) in our MBE-GaAs DHs with both doping-types, which is possible in the HLI regime where τ_{nr} is always equal to the sum of electron and hole lifetimes.[3] The lifetime-limiting defect observed in our materials exhibits a steep ($E_\infty = (258 \pm 1)meV$) increase in capture cross-section. In light of available DLTS evidence [8, 9, 11, 19] we can rule out most intrinsic-defects and impurities, since they would have much smaller E_∞.[4] The measured E_∞ is close to the 0.25eV values observed for the σ_n of Level B by DLTS [11]; however, the consistency with the CZ-GaAs results suggest that this signature is due to a change in σ_p and not σ_n. The EL2 defect has the only known σ_p low-enough to give rise to a large E_∞ value during its exponential increase to $\sigma_\infty \approx (6 \times 10^{-15})cm^2$ associated with MPE capture [11], and this is discussed further in Section 6.2. Since the LLI work done to characterize σ_p using n-CZ-GaAs was consistent with this E_∞ value, it is likely that the lifetime of all samples are limited by hole-capture via EL2.

The common decrease in lifetime above 300K does not explain the variation in lifetime observed at (and just below) room temperature between the doping types, where the lifetime is lower in the n-type material. This difference is parametrized by the variation in r_σ. Without further experimentation, it is not possible to distinguish whether this variation in r_σ comes from a secondary defect, or from a variation in σ_o of the common defect. Cross-sections are often considered to be constant (at a given temperature); however, it has been shown [8] that the EL2 hole-capture σ_o increases by 5 to 6 orders of magnitude in the presence of a strong ($10kV/cm$) electric field. Electric fields of this magnitude are found in the depletion region at the surface of GaAs [90], and also at the InGaP/GaAs interface [91]. A difference in electric field strength could provide different degrees of recombination-enhancement in the depletion regions of

[3] In the case where the low-level injection (LLI) lifetime (the minority-carrier lifetime) is much less than the HLI-lifetime, the system rapidly transitions from the HLI to a trap-limited regime, screening the measurement of the LLI-lifetime.

[4] Chromium is an important impurity in CZ-GaAs; however, its E_∞ for electron- ($117meV$) and hole-capture ($20meV$) [19] are too low in comparison to our measured $E_\infty = (258 \pm 1)meV$.

the n-type and p-type MBE DH samples and account for the observed variation of σ_o. Simulations of the electric-field strength in the DH samples are discussed in Section 6.3. The variation of σ_o with electric-field strength means that limitation of the lifetime by a single common defect remains as a viable conclusion.

A relatively recent study by Bourgoin and De Angelis has also found EL2 to be the lifetime-limiting defect in $p^+ - n$ junctions grown using CZ and MOCVD GaAs [31]. The junction that they have studied is abrupt and so the recombination occurs primarily in the depleted n-type side, which reflects a similar system to our observed surface-depletion-enhanced recombination. The conclusions of [31] were based on the observation that both the recombination current and the EL2 density varied by about three orders of magnitude between their MOCVD and CZ samples.

It is possible for defects below the detection limits of DLTS to still limit the lifetime, as was shown to be the case in Si with the metastable boron-oxygen defect. While it was known that this defect limited the lifetime in Si, the density was below the limit of DLTS and its electronic properties could only be characterized with LS [92]. The presence of a lifetime-limiting defect too dilute to observe with DLTS ($N_t < 10^{12} cm^{-3}$) is especially possible in MBE-GaAs, where densities of all defects are below $10^{14} cm^{-3}$ [57]. While EL2 can be readily produced in MBE with low growth-temperature [28, 66] or As-excess [93], it is generally not observed in as-grown MBE-GaAs (i.e. its density falls below $10^{12} cm^{-3}$) [57]. In light of the narrow relevant sensitivity range of DLTS for MBE-GaAs, conclusions based purely on DLTS densities and cross-sections [9] should be interpreted with caution, and alternative hypotheses still explored. Given that EL2 has played such a significant role in GaAs from every other growth method [25, 57, 58], and that we are observing common E_∞ between CZ and MBE, it is worth not ruling out its participation in recombination based on limited DLTS results [57].

By performing TD-TR-PLD experiments on our thin-film MBE-GaAs samples, I have measured $f(T)$ and τ_{bulk} from 77-700K using a new HLI model (3.26) for $\eta(t)$, and characterized the lifetime-limiting defect. The evidence strongly suggests EL2

as the dominant recombination centre, as the measured $E_\infty = (258 \pm 1)meV$ that is common between both n- and p-type MBE-DHs is consistent with $E_\infty = (261 \pm 7)meV$ measured from the hole-lifetime observed using LLI TR-PLD with the n-type CZ-GaAs sample. Consistency with LLI CZ results indicate limitation by an intrinsic (As- or Ga-related) defect, and that recombination is limited by hole-capture in the HLI MBE-GaAs experiments. Currently, there is no characterization of the EL2 hole-capture cross-section in GaAs above 340K [8, 9], and these results from TD-TR-PLD provide a signature that can be tested using DLTS above room-temeperature. If EL2 is not found to exhibit a high-E_∞ increase, then motivation is provided for further measurement of uncharacterized σ_p for other defects in GaAs.

Chapter 6

Conclusion and Future Work

6.1 Summary of New Models

Design of the TD-TR-PLD system was guided by my new solution to the diffusion equation in three-dimensions (3.16), which provides explicit defocusing conditions for excitation under which radial-diffusion can be safely neglected. From this modelling of diffusion and surface recombination, I have found theoretically and demonstrated experimentally that TR-PLD in thick,[1] unpassivated materials follows time-dependence of $e^{-t/\tau_{bulk}}/\sqrt{t}$. This new model (3.20) provides deeper intuition into nonlinear decay observed from unpassivated materials, as well as confidence in τ_{bulk} measured under these circumstances. In thick materials, axial homogeneity can only be attained using sub-bandgap two-photon absorption [94]. By using (3.20), axial diffusion is taken into account without need for additional fit parameters, or sub-bandgap two-photon absorption capabilities. I have derived another analytical expression (3.21) that quantifies the total fraction of carriers lost to front-surface recombination (f_{loss}) in terms of the absorptivity, diffusivity, lifetime, and surface-recombination-velocity. This new equation (3.21) is elegant, and provides intuition into the dependence of f_{loss}

[1] Thick is defined here in relation to the diffusion length, $\sqrt{D_a \tau_{bulk}}$.

on excitation-wavelength, temperature, and surface-recombination-velocity.

To further support understanding of localization in our materials, temperature-resolved ($\Delta T = 50K$) PL spectra were measured for the n-type ($N_D = 2 \times 10^{18} cm^{-3}$) CZ-GaAs sample. Results demonstrated significant localization below room-temperature, with residual localization still observed at 300K. Above 350K localized states are no longer significantly occupied, and measured PL spectra show the exponential tail in the conduction band density of states (DOS) expected for doping levels above $10^{17} cm^{-3}$ [33]. The problem of band tailing has been addressed with rigour by Halperin and Lax [34]; however, no clear method of fitting experimental data was provided. Using a method (3.39) of approximating the true DOS, I have been able to measure the doping level ($(2.3 \pm 0.2) \times 10^{18} cm^{-3}$) and an exponential band-tail (e^{E/E_o}, [33]) characterized by $E_o = (14.5 \pm 0.3) meV$ from fitting the PL spectra at 600K with (3.40). These parameters, including E_g, have also been measured from PL spectra above 350K using (3.40), yielding consistent results from 350-600K. The measured E_o is within the range of 5 to $18 meV$, observed (with IR-absorption) to increase with doping in n-GaAs in the $4 \times 10^{16} - 6.8 \times 10^{18} cm^{-3}$ range [82]. Our measured E_o agrees with the value of $13.6 meV$ measured at $N_D = 3 \times 10^{18} cm^{-3}$ [82]. The slope of the exponential tail and the measured donor density demonstrate the accuracy of this new model (3.40), and provide new contactless means by which doping-level can be estimated.

To parametrize localization dynamics, I have derived new analytical models to account for deep-level filling (3.32), as well as shallow-trap capture and emission (3.35). By fitting with these models as laser power is increased, I have shown that quasi-equilibrium conditions between the extended and localized energy levels can be attained, giving rise to decay that reflects the true τ_{bulk} in the material. This finding provided confidence in the interpretation of nonlinearity from observed TR-PLD, and has motivated the experiments performed at high laser-power.

I have developed a new model (3.26) for use with high laser power that enables TR-PLD results to reflect bulk recombination, and not be influenced by trap-emission.

This model takes into account both nonradiative and radiative recombination, and allows for the measurement of the radiative efficiency ($f(T)$) from the nonlinearity. Fitting TR-PLD data from 77-700K, I have demonstrated that (3.26) can be used to provide measurement of both τ_{bulk} and $f(T)$. This new analytical model describes how $f(T)$ and the initial injection level (η_o) influence the nonlinearity observed in our TR-PLD experiments, enabling the accurate resolution of the temperature-dependence of τ_{bulk} and providing greater intuition into the source of this nonlinearity at high laser-power. Analysis of the measured τ_{bulk} has provided measurement of $f(T)$ and characterization of the lifetime-limiting defect in our CZ- and MBE-GaAs samples.

In order to measure $f(T)$ from the temperature dependence of τ_{bulk}, I needed to develop a new model (3.7) to describe the temperature-dependence of τ_r. By solving the integral for τ_r under approximations described in Section 3.2.1, I have shown that τ_r increases with temperature in proportion to $N_C(T) \cdot N_V(T)/T$. This simple expression should be applicable to any direct bandgap semiconductor, and for those that satisfy the parabolic-band approximation for the effective densities of states (3.7) shows that $\tau_r \propto T^2$. In GaAs, this T^2 dependence is true at low temperature[2] where τ_r limits τ_{bulk}. This new model for τ_r, combined with the MPE capture model (3.8) for σ [11] have allowed for fitting the temperature-dependent τ_{bulk} measured using TD-TR-PLD. Using surface fits of TD-TR-PLD data with a single function containing a new models for $\tau_r(T)$ (3.7) and $\eta(t)$ (3.26), I measured the room-temperature radiative efficiency to be $f(300K) = (12.2 \pm 0.2)\%$ in n-type and $f(300K) = (20.5 \pm 0.2)\%$ in p-type. The $B(300K)$ of $(4.48 \pm 0.01) \times 10^{-10} cm^3/s$ (n-type) and $(2.71 \pm 0.01) \times 10^{-10} cm^3/s$ (p-type) measured in MBE-GaAs using TD-TR-PLD agree with literature values [47, 51], and the measured $f(300K)$ are consistent with those expected based on literature results at $10^{16} cm^{-3}$ doping level in both p-type [88] and n-type [89] GaAs.

[2]See (C.1) for the correction to the parabolic-band approximation density of states in GaAs, where the parabolic-band approximation yields less than 7% error below 300K, and less than 0.25% error below 200K.

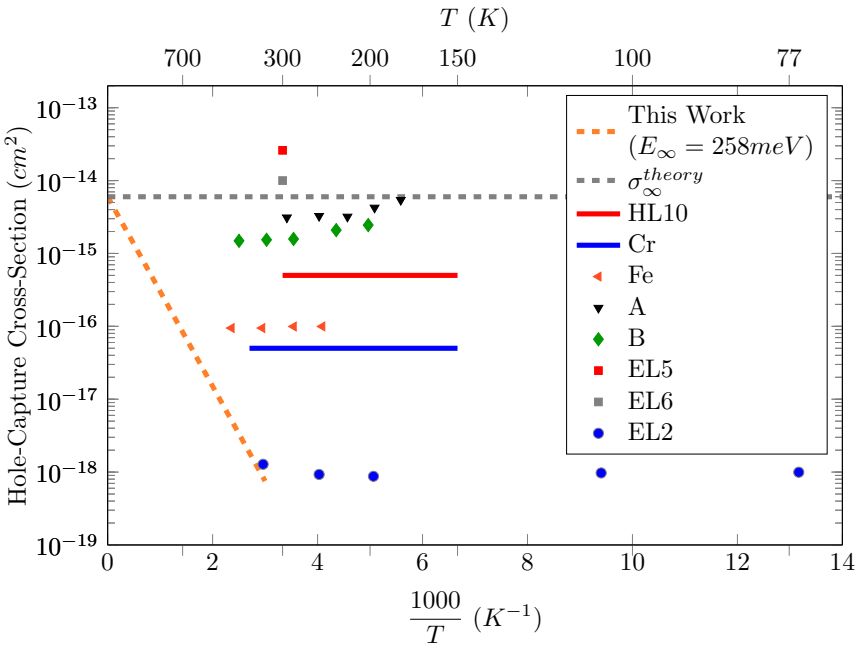

Figure 6.1: Hole-capture cross-sections (σ_p) previously measured in as-grown GaAs using DLTS for EL2 [8], EL5 [9], EL6 [10], HL10 [9], Level A [8], Level B [8], Cr [9], and Fe [8]. Results for EL6 were presented without specified temperature [10], and so 300K is assumed. The grey dashed line shows $\sigma_\infty^{theory} \approx (6 \times 10^{-15})cm^2$ from MPE capture [11], and the orange dashed line shows $\sigma_\infty^{theory} e^{-E_\infty/k_B T}$ using $E_\infty = 258meV$ measured in this work from surface-fits to TD-TR-PLD on the MBE-GaAs DH samples.

6.2 Defect Identification

In all samples studied using TD-TR-PLD, the measured τ_{bulk} dropped exponentially when temperature was increased above 300K. This drop is due to the exponential increase in σ of the dominant defect, and is characterized by E_∞. In the $N_D = 2 \times 10^{18}cm^{-3}$ CZ-GaAs experiments, $E_\infty = (261 \pm 7)meV$ was obtained by fitting the LLI τ_{nr} lifetimes measured from 500-600K using TR-PLD fit with (3.20). In the LLI regime, the minority-carrier lifetime is observed, and so this E_∞ characterizes a change in σ_p of the dominant defect in the CZ-GaAs sample. Fig. 6.1 shows σ_p previously measured by others in as-grown GaAs using DLTS for EL2 [8], EL5 [9], EL6 [10], HL10 [9], Level A [8], Level B [8], Cr [9], and Fe [8]. According to MPE theory [11], σ should intercept at $\sigma \approx 6 \times 10^{-15}cm^2$, and so this value is plotted as a

grey dashed line. The orange dashed line shows a theoretical estimate of the expected σ_p using the theoretical σ_∞ and the value of $E_\infty = 258meV$ measured in this work.[3] Previously proposed dominant defects in GaAs include EL2 [30, 31], HL10 [9], EL6 [10], and EL5 [12]. Based on the known σ_p, we can rule out EL5, EL6, Level A, Level B, and HL10 since they are too close to σ_∞ and should yield either a low E_∞ value, or a high ($> 700K$) onset temperature for the change. Fe and Cr are closer candidates; however, the onset temperate should be around 600-700K if they were to exhibit this E_∞. EL2 clearly has a low enough σ_p to provide room for an increase with the measured E_∞ from 500-600K. EL2 is the only defect found in as-grown GaAs that is consistent with the E_∞ observed in the n-CZ-GaAs.

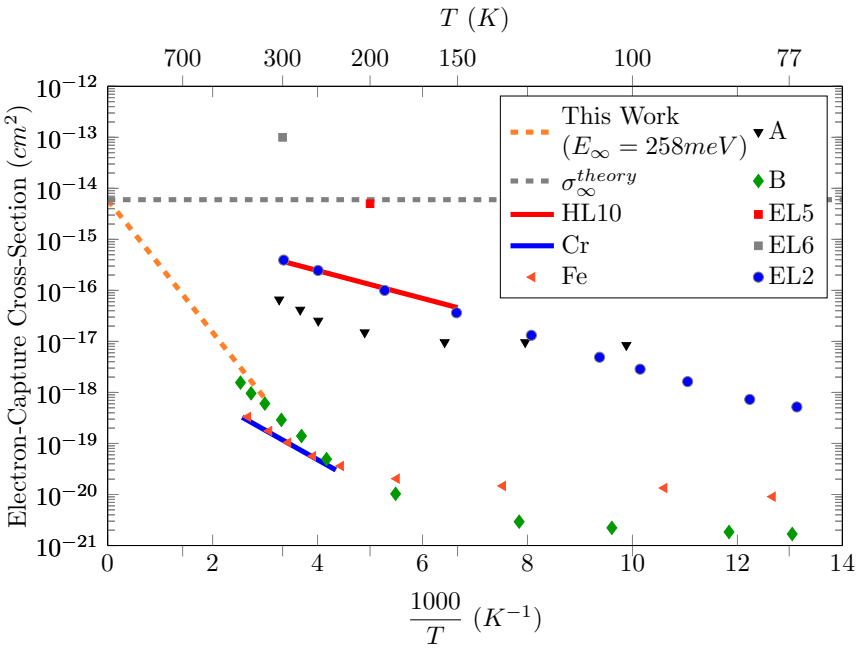

Figure 6.2: Electron-capture cross-sections (σ_n) previously measured in as-grown GaAs using DLTS for EL2 [8], EL5 [12], EL6 [10], HL10 [9], Level A [8], Level B [8], Cr [9], and Fe [8]. Results for EL5 [12] and EL6 [10] were presented without specified temperature, and so 300K is assumed. The grey dashed line shows $\sigma_\infty^{theory} \approx (6\times10^{-15})cm^2$ from MPE capture [11], and the orange dashed line shows $\sigma_\infty^{theory} e^{-E_\infty/k_BT}$ using $E_\infty = 258meV$ measured in this work from surface-fits to TD-TR-PLD on the MBE-GaAs DH samples.

[3]This value of E_∞ was obtained from the fits to MBE-GaAs TD-TR-PLD, and is consistent with the measured value in CZ-GaAs.

In the MBE-GaAs samples, strong excitation was used to observe the HLI lifetime. Under HLI conditions, the electron and hole densities are approximately constant ($n \approx p$), and so recombination is limited by capture of the carrier with the smallest cross-section. Because of this, and the common E_∞ value measured from both samples, I have found that recombination is limited by the capture of a single carrier type (i.e. either electrons or holes) in the TD-TR-PLD performed on MBE-GaAs of both doping types under HLI conditions. The σ_p have been discussed above, and Fig. 6.2 shows σ_n for all known defects previously measured in as-grown GaAs using DLTS. The value of $E_\infty = (258 \pm 1)meV$ measured from MBE-GaAs is consistent with the $E_\infty = (261 \pm 7)meV$ measured from n-CZ-GaAs. Since the n-CZ-GaAs measurements were done under LLI conditions, it was the hole-lifetime that was measured and σ_p that was characterized. Given the consistency in E_∞ measured from CZ and MBE samples, I believe that the hole-lifetime has been measured in both MBE samples as well. This means that Level B is not a candidate defect for the lifetime-limiting defect, even though its σ_n has $E_\infty \approx 0.25eV$. EL2 is the only defect known in as-grown GaAs to have a sufficiently low σ_p to exhibit the observed E_∞ with an onset temperature as low as 300K, and its relatively high σ_n explains why hole-capture limits recombination under HLI conditions in the TR-PLD experiments on MBE-GaAs of both doping-types. In Section 6.4, I will discuss experiments that can be done to determine if EL2 is truly dominant in these materials, as suggested by these TD-TR-PLD experiments.

6.3 Electric-Field Enhancement of EL2

Previous arguments against dominance of EL2 [9] have suggested that its cross-section is too low to limit the lifetime to the values observed in GaAs. Electric fields on the order of those observed [90] at the bare surface of GaAs ($\sim 10kV/cm$) have been shown to increase the minimum EL2 cross-sections by 5 to 6 orders of magnitude [8], and this mechanism drives these defects to be more effective at capturing carriers

than their zero-field σ_o would suggest. An alternative conclusion that cannot be ruled out without further experimentation would be the presence of a secondary defect that limits below room temperature.

To estimate the surface field present in our MBE-GaAs DHs, I performed simulations using wxAMPS. The surface field of the InGaP/GaAs heterostructure depends on the InGaP surface charge (Fermi-level pinning), the doping in the InGaP layer [91], and the InGaP/GaAs band offset. Midgap Fermi-level pinning was assumed, in the absence of experimental data relevant to our lightly doped DH with native oxide on the InGaP surface. Fermi-level pinning is expected in the DH, since carriers are prevented from reaching the front surface and altering its charge. Hashizume [95] has measured Fermi-level pinning in n-InGaP, and measured the surface Fermi-level at $250meV$ above midgap for samples treated with HCL:2·H_2O and $50meV$ above midgap for samples treated with HF:5·C_2H_5OH; however, they are using Si-doped material (ours is undoped) and they have etched away the native oxide that they also claim dominates the electronic properties of the InGaP surface. In addition, InGaP surfaces vary considerably with orientation, atomic surface arrangement, and sublattice ordering effects [95]. As a result, I have no reason to believe that the surface Fermi-level reported by [95] is representative of our undoped InGaP surface with its native oxide intact.[4] The simulated band-diagrams are shown in Fig. 6.3 and 6.4. The electric-field strengths and their ratio ($E_{\text{n-type}}/E_{\text{p-type}}$) are shown in Figs. 6.5 and 6.6, respectively.

The experimentally observed band offset in the conduction band, between InGaP and GaAs ranges from $60meV$ [96] to $100meV$ [97]. In simulating the system using wxAMPS, I used the smaller estimate of $60meV$ to make a conservative[5] estimate at how much larger the n-type surface field is. While a $60meV$ barrier may confine carriers at 300K and below, one is justified to wonder if an EL2 signal is actually measured

[4]Simulations were also done using the Fermi-level position from [95], and a strong built-in potential was still present, with comparable electric-field strengths (still on the order of $10kV/cm$) in the n-type and p-type (with the n-type being slightly higher).

[5]Simulation using the $100meV$ conduction-band offset yields a higher E_n/E_p ratio than $60meV$.

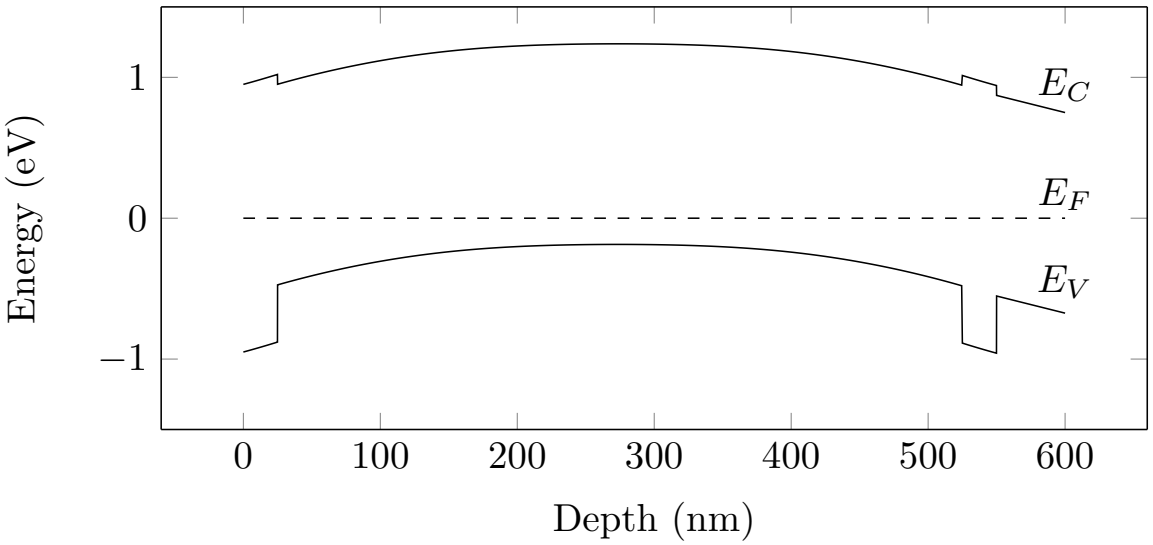

Figure 6.3: Band diagram (simulated using wxAMPS) for the p-MBE-GaAs sample. The simulation (and samples) included a $50nm$ (undoped) GaAs buffer layer. Midgap ($E_C - 0.95EV$) E_F-pinning was assumed for InGaP, and $E_C - 0.75eV$ in the GaAs buffer layer, as proposed for interfaces between lightly doped and SI GaAs by Chandra et al. [13].

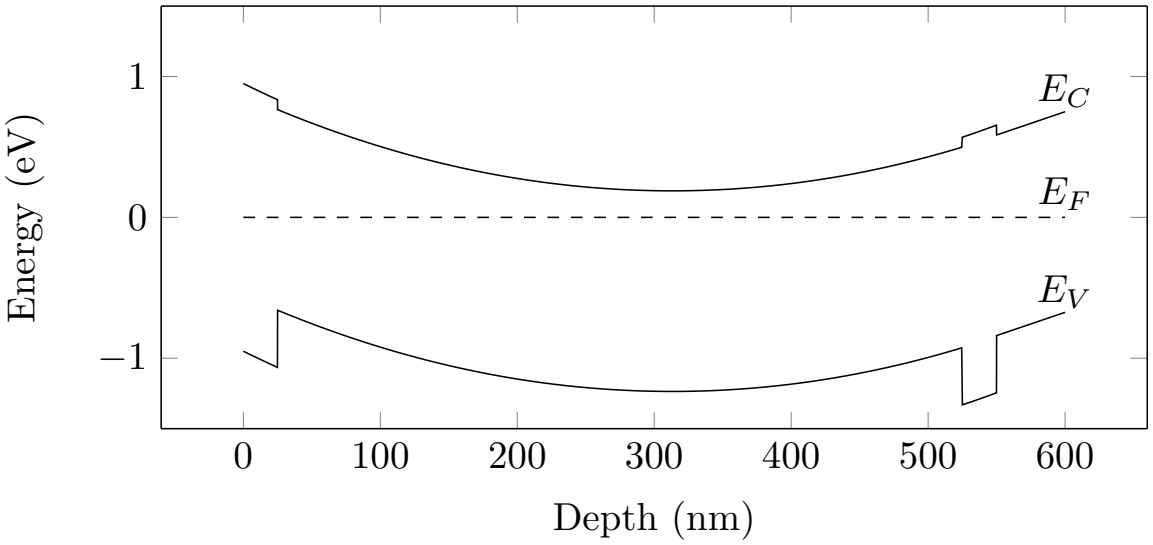

Figure 6.4: Band diagram (simulated using wxAMPS) for the n-MBE-GaAs sample. The simulation (and samples) included a $50nm$ (undoped) GaAs buffer layer. Midgap ($E_C - 0.95EV$) E_F-pinning was assumed for InGaP, and $E_C - 0.75eV$ in the GaAs buffer layer, as proposed for interfaces between lightly doped and SI GaAs by Chandra et al. [13].

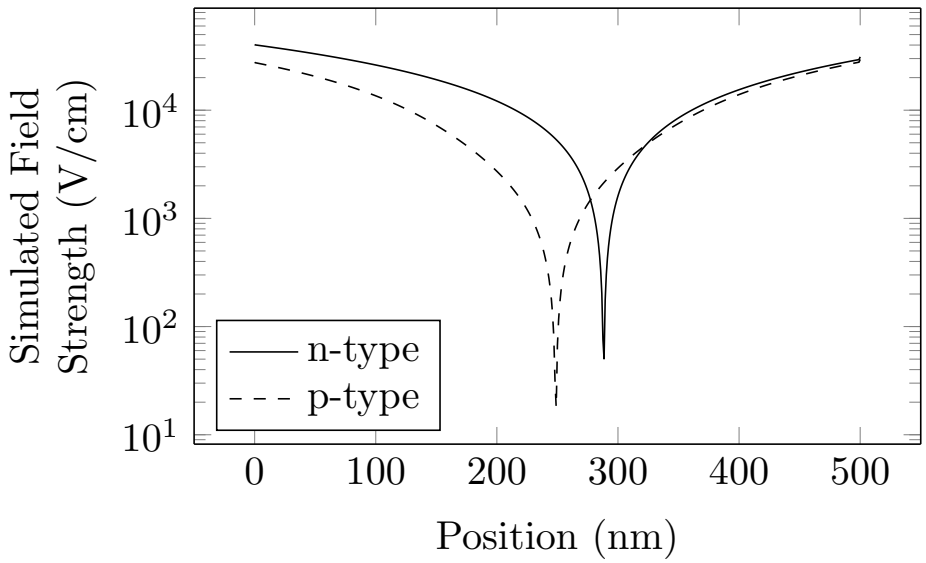

Figure 6.5: Simulated electric fields in the n-type and p-type MBE-GaAs samples (from the wxAMPS simulations in Figs. 6.3 and 6.4) in the GaAs layer.

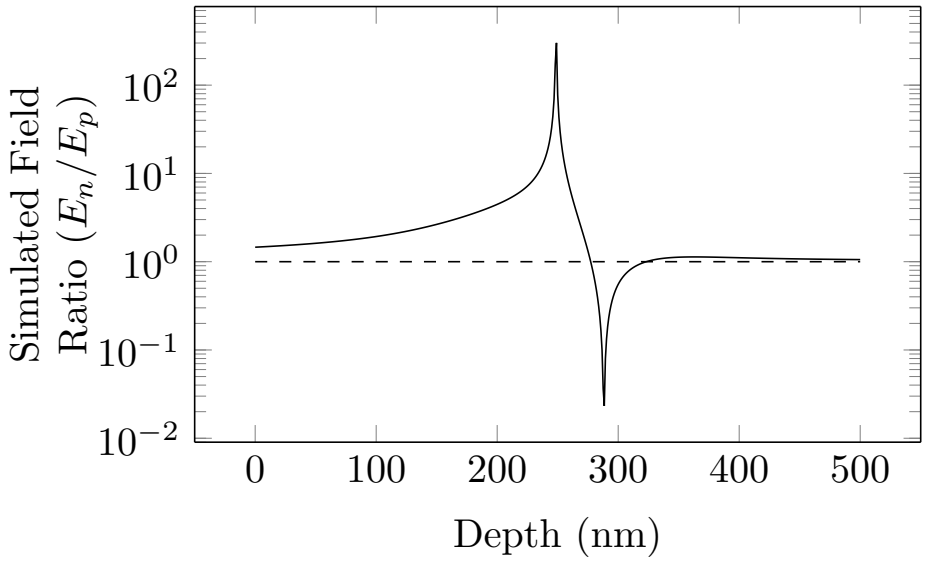

Figure 6.6: Simulated ratio of electric fields n-type and p-type MBE-GaAs samples in the GaAs layer. The dotted line is a visual aid for when $E_p = E_n$.

due recombination in the semi-insulating substrate, where there is an intentionally large concentration of this defect.[6] While these arguments are valid, the trapping effect of the electric field confines the carriers to the front surface, where the barrier is much higher. From the wxAMPS simulations, the barrier associated with the built-in surface potential is $570meV$ in n-type and $290meV$ in p-type. While simulations are useful in gaining understanding, the key experimental evidence that recombination is occurring in the MBE-GaAs (and not the SI-GaAs substrate) is the observation of a higher lifetime in p-type material than in n-type.[7] If the InGaP barrier were overcome as temperature is increased, then we would observe an abrupt drop in the lifetime into the picosecond regime, as verified by the TR-PLD measurements on the bare SI-GaAs substrate (shown in Fig. 6.7). The absence of carrier migration into the SI-GaAs provides another line of evidence that there is a sufficient built-in potential at the surface to confine the electrons in our p-MBE-GaAs DH.

The most simple model is that EL2 is the single dominant defect. The observed differences in r_σ can be explained by surface-field enhancement of σ_o [8]. From our experiments the ratio of σ_o can be calculated[8] in our samples by the ratio of measured r_σ values to be $r_\sigma^{\text{p-type}}/r_\sigma^{\text{n-type}} = (2.50 \pm 0.05)$. Electric-field enhancement can explain the difference in r_σ observed between doping types in the MBE-GaAs TD-TR-PLD experiments, leaving the viable conclusion of EL2 as the single dominant defect.

[6] EL2 is used to compensate (i.e. trap the holes from) the large acceptor concentration (associated with carbon impurities) in CZ-GaAs [58].

[7] While the surface depletion confines the minority-carriers in our lightly doped MBE-GaAs samples, this will not be the case in samples with higher doping. To approach the study of high-temperature lifetime in GaAs, it may be necessary to consider capping layers made with materials with larger conduction band offsets in p-type (InGaP can still be used for n-type, as the barrier is $\sim 400meV$, [96]).

[8] Since a common defect limits the lifetime above 300K in both samples the two $r_\sigma = \sigma_\infty/\sigma_o$ have the same value for σ_∞, and therefore $r_\sigma^{\text{p-type}}/r_\sigma^{\text{n-type}} = \sigma_o^{\text{n-type}}/\sigma_o^{\text{p-type}}$.

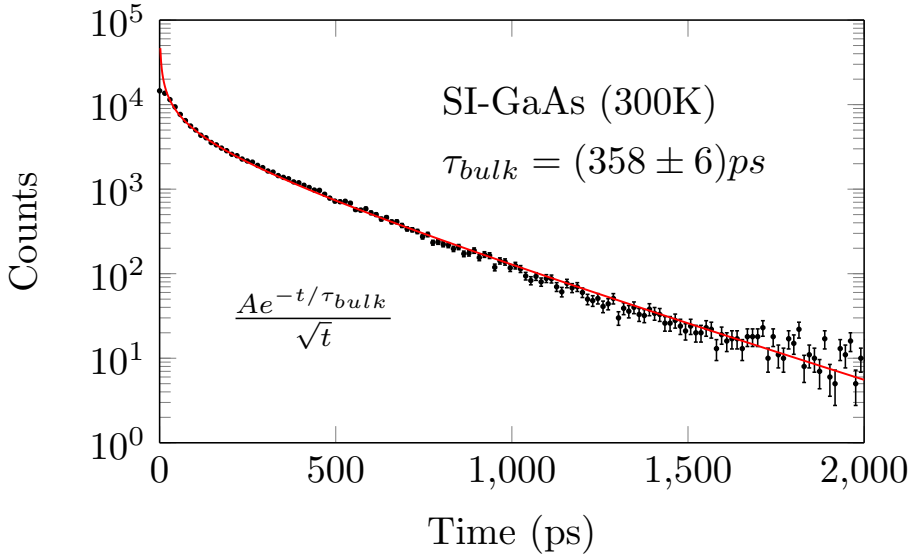

Figure 6.7: TR-PLD measurement (black data points) made on SI-GaAs wafer with $4\mu J$ excitation pulse-energy. The fit (red line) was performed using (3.20).

6.4 Future Work

I have shown that $f(T)$ can be measured in GaAs by fitting the temperature dependence of τ_{nr}. These experiments should be repeated with variation in the doping-level and doping-type, to further test the capabilities of the TD-TR-PLD technique, and the new models that have been derived for its analysis. With these capabilities, we are able to make new quantitative comparisons between GaAs grown using different methods, and a comparison between the $f(T)$ measured from MBE and MOCVD samples would be very interesting. Study of $f(T)$ with varied sample width should provide greater insight into the photon-recycling [49, 50] model for the dependence of τ_r on thickness. The TD-TR-PLD system has been designed with a high optical bandwidth to accommodate a wide variety of direct-bandgap semiconductors. The new models derived for analysis of TD-TR-PLD have been presented in generalized forms that allow their application to experiments in any of these material systems, and so it should be possible to measure $f(T)$ from other direct bandgap semiconductors.

The identification of EL2 as the lifetime-limiting defect in our samples relied on the

existing knowledge gained by DLTS characterization of GaAs. Although GaAs is the most well-studied compound semiconductor, there are still gaps in our understanding of the temperature dependence of σ. In particular, it would be of great value to this technique if high-temperature DLTS were performed to measure σ for EL2 (and other defects) up to temperatures of 700K and above. This would strengthen our understanding of the MPE capture mechanism, and provide better estimates of the E_∞ associated with each defect. A good example of this type of characterization is the σ_p reported for the "O" defect (State 1) in GaP by [11], where its high-E_∞ increase was observed to begin above 500K. Exponential increases have also been observed in the σ of defects in InGaP [20], GaAsN [21], InP [22] and InGaAs [23]; however, the DLTS characterization literature available is not nearly as comprehensive as for GaAs. Improved knowledge of how the σ of each defect depends on temperature will enable TD-TR-PLD to be applied to the identification of lifetime-limiting defects in other GaAs structures, as well as in other direct-bandgap semiconductors.

Given the electric-field enhancement of recombination, surface-depletion plays a role in trapping minority carriers and reducing τ_{bulk} and $f(T)$. The depletion problem can be mitigated through optimization of the InGaP doping-level, as this has been shown (using photoreflectance) to be able to eliminate the interface field between InGaP and SI-GaAs [91]. This can allow for the use of low doping, without the losses associated with surface-depletion trapping. Lifetimes measured from TR-PLD can be used to optimize the doping-levels of the InGaP and GaAs layers to allow for lightly-doped structures with minimal depletion-enhanced recombination, and this can be further supported by $f(T)$ measurements from TD-TR-PLD. Devices where high-doping is required (with long diffusion lengths still desired) will be limited by τ_{nr}, and in this case other means (such as inhibited emission [51]) might be useful in achieving higher τ_{bulk}.

To determine if a secondary defect is limiting τ_{nr} below 300K, it is necessary to change the concentration of one of the species and look for a correlation in the measured

lifetimes. Since there is no defect-specific signature present in τ_{nr} below 300K, we do not have any information as to what this defect might be from the TD-TR-PLD results alone. In light of this, it makes sense to first vary the EL2 concentration, and this can be done by variation of the growth-stoichiometry [98] and MBE growth-temperature [28, 66]. Further study may reveal that a secondary defect does play a role in limiting τ_{nr} below 300K. In either case, I have shown that the common defect (that I have associated with EL2) contributes to nonradiative recombination at 300K. If a secondary defect is limiting τ_{nr} below 300K, then EL2 would still be responsible for about 3% (n-type) and 7% (p-type) of the nonradiative recombination at 300K. Many devices (such as concentrator solar cells) operate above 300K due to heat dissipation, and the increase in the EL2 cross-section yields a minimum contribution of 12% (n-type) and 24% (p-type) at 350K; and so I have shown that EL2 is responsible for significant temperature-induced lifetime reduction.

Using new models and the TD-TR-PLD system, the radiative-efficiency and bulk-lifetime have been measured and found to be limited by the EL2 defect in GaAs grown using MBE and CZ methods. This work has demonstrated the utility of information gained by previous research on GaAs using DLTS. With this new complementary technique, the characterization done on GaAs and other direct bandgap semiconductors has gained significant value to the identification of dominant defects. Lifetime-limiting defects are of particular interest to photovoltaics, as any defect that limits $f(T)$ also limits the efficiency of solar energy conversion. Identification of these defects should provide guidance to developing devices with higher radiative efficiency, which is relevant to any solid-state devices that are designed to emit or detect light efficiently.

Bibliography

[1] J Lagowski, DG Lin, T-P Chen, M Skowronski, and HC Gatos. Native hole trap in bulk GaAs and its association with the double-charge state of the arsenic antisite defect. *Applied Physics Letters*, 47(9):929–931, 1985.

[2] Keung L Luke and Li-Jen Cheng. Analysis of the interaction of a laser pulse with a silicon wafer: Determination of bulk lifetime and surface recombination velocity. *Journal of Applied Physics*, 61(6):2282–2293, 1987.

[3] J. Vaitkus. The nonequilibrium hall effect and related transport phenomena in semiconductors under inhomogeneous excitation by laser pulse. *Physica Status Solidi Applied Research*, 34:769–775, 1976.

[4] A.B. Sproul. Dimensionless solution of the equation describing the effect of surface recombination on carrier decay in semiconductors. *Journal of Applied Physics*, 76:2851, 1994.

[5] Brian A Ruzicka, Lalani K Werake, Hassana Samassekou, and Hui Zhao. Ambipolar diffusion of photoexcited carriers in bulk GaAs. *Applied Physics Letters*, 97(26):262119, 2010.

[6] David E Aspnes and AA Studna. Dielectric functions and optical parameters of Si, Ge, GaP, GaAs, GaSb, InP, InAs, and InSb from 1.5 to 6.0eV. *Physical Review B*, 27(2):985, 1983.

[7] F Cadiz, D Paget, ACH Rowe, VL Berkovits, VP Ulin, S Arscott, and E Peytavit. Surface recombination in doped semiconductors: Effect of light excitation power and of surface passivation. *Journal of Applied Physics*, 114(10):103711, 2013.

[8] V Ya Prinz and SN Rechkunov. Influence of a strong electric field on the carrier capture by nonradiative deep-level centers in GaAs. *Physica Status Solidi (b)*, 118(1):159–166, 1983.

[9] A Mitonneau, A Mircea, GM Martin, and D Pons. Electron and hole capture cross-sections at deep centers in gallium arsenide. *Revue de Physique Appliquée*, 14(10):853–861, 1979.

[10] ZQ Fang, TE Schlesinger, and AG Milnes. Evidence for EL6 (E_c-0.35 eV) acting as a dominant recombination center in n-type horizontal Bridgman GaAs. *Journal of applied physics*, 61(11):5047–5050, 1987.

[11] CH Henry and DV Lang. Nonradiative capture and recombination by multiphonon emission in GaAs and GaP. *Physical Review B*, 15(2):989, 1977.

[12] Liang Bingwen, Zou Yuanxi, Zhou Binglin, and AG Milnes. Minority carrier diffusion lengths in bulk n-type GaAs. *Journal of electronic materials*, 16(3):177–180, 1987.

[13] Amitabh Chandra, Colin EC Wood, David W Woodard, and Lester F Eastman. Surface and interface depletion corrections to free carrier-density determinations by Hall measurements. *Solid-State Electronics*, 22(7):645–650, 1979.

[14] William Shockley and Hans J Queisser. Detailed balance limit of efficiency of p-n junction solar cells. *Journal of Applied Physics*, 32(3):510–519, 1961.

[15] J. Müller, H. Reichl, and H. Bernt. A method to determine minority carrier lifetime in GaAs light-emitting diodes. *Solid-State Electronics*, 22(3):257 – 260, 1979.

[16] HY Ryu, KH Ha, JH Chae, KS Kim, JK Son, OH Nam, YJ Park, and JI Shim. Evaluation of radiative efficiency in ingan blue-violet laser-diode structures using electroluminescence characteristics. *Applied Physics Letters*, 89(17):1106, 2006.

[17] Stefan Rein. *Lifetime spectroscopy: a method of defect characterization in silicon for photovoltaic applications*, volume 85. Springer Science & Business Media, 2006.

[18] Douglas M Powell, Mark T Winkler, Al Goodrich, and Tonio Buonassisi. Modeling the cost and minimum sustainable price of crystalline silicon photovoltaic manufacturing in the United States. *IEEE Journal of Photovoltaics*, 3(2):662–668, 2013.

[19] GM Martin, A Mitonneau, D Pons, A Mircea, and DW Woodward. Detailed electrical characterisation of the deep Cr acceptor in GaAs. *Journal of Physics C: Solid State Physics*, 13(20):3855, 1980.

[20] Aurangzeb Khan, Masafumi Yamaguchi, Nothaj Dharmaso, Jacques Bourgoin, Koshi Ando, and Tatsuya Takamoto. Deep level transient spectroscopy analysis of 10 MeV proton and 1 MeV electron irradiation-induced defects in p-InGaP and InGaP-based solar cells. *Japanese Journal of Applied Physics*, 41(3R):1241, 2002.

[21] Boussairi Bouzazi, Hidetoshi Suzuki, Nobuaki Kojima, Yoshio Ohshita, and Masafumi Yamaguchi. Double carriers pulse DLTS for the characterization of electron–hole recombination process in GaAsN grown by chemical beam epitaxy. *Physica B: Condensed Matter*, 406(5):1070–1075, 2011.

[22] Koshi Ando, Masafumi Yamaguchi, and Chikao Uemura. Nonradiative-recombination-enhanced defect-structure transformation in low-temperature γ-ray-irradiated inp. *Physical Review B*, 34(4):3041, 1986.

[23] A Mircea, A Mitonneau, J Hallais, and M Jaros. Study of the main electron trap in $Ga_{1-x}In_xAs$ alloys. *Physical Review B*, 16(8):3665, 1977.

[24] GA Baraff and M Schluter. Bistability and metastability of the gallium vacancy in GaAs: the actuator of EL2? *Physical Review Letters*, 55(21):2340, 1985.

[25] J.M. Baranowski and P. Trautman. *Energy levels and fundamental properties of the EL2 defect in GaAs.* In Brozel and Stillman [99], 1995.

[26] BK Meyer. Electron nuclear double resonance (ENDOR) spectroscopy of the EL2 defect in GaAs. *Revue de Physique Appliquee*, 23(5):809–816, 1988.

[27] MO Manasreh and DW Fischer. Infrared absorption properties of the EL2 and the isolated as ga defects in neutron-transmutation-doped GaAs: Generation of an EL2-like defect. *Physical Review B*, 39(5):3239, 1989.

[28] MO Manasreh, David C Look, KR Evans, and CE Stutz. Infrared absorption of deep defects in molecular-beam-epitaxial GaAs layers grown at 200C: Observation of an EL2-like defect. *Physical Review B*, 41(14):10272, 1990.

[29] GM Martin. Optical assessment of the main electron trap in bulk semi-insulating GaAs. *Applied Physics Letters*, 39(9):747–748, 1981.

[30] MD Miller, GH Olsen, and M Ettenberg. The effect of gas-phase stoichiometry on deep levels in vapor-grown GaAs. *Applied Physics Letters*, 31(8):538–540, 1977.

[31] JC Bourgoin and N De Angelis. The defect responsible for non-radiative recombination in GaAs materials. *Semiconductor Science and Technology*, 16(6):497, 2001.

[32] S.W. Johnston and R.K. Ahrenkiel. Measurement of the temperature-dependent recombination lifetimes in photovoltaic materials. In *American Institute of Physics Conference Series*, volume 462, pages 505–510, 1999.

[33] Brian Tuck. Conduction band density of states in impure GaAs. *Journal of Physics and Chemistry of Solids*, 29(4):615–622, 1968.

[34] BI Halperin and Melvin Lax. Impurity-band tails in the high-density limit. i. minimum counting methods. *Physical Review*, 148(2):722, 1966.

[35] W Shockley and WT Read Jr. Statistics of the recombinations of holes and electrons. *Physical Review*, 87(5):835, 1952.

[36] J. P. Bergman, C. Hallin, and E. Janzén. Temperature dependence of the minority carrier lifetime in GaAs/AlGaAs double heterostructures. *Journal of Applied Physics*, 78(7), 1995.

[37] JM Olson, RK Ahrenkiel, DJ Dunlavy, Brian Keyes, and AE Kibbler. Ultralow recombination velocity at $Ga_{0.5}In_{0.5}P$/GaAs heterointerfaces. *Applied Physics Letters*, 55(12):1208–1210, 1989.

[38] CR Haughn, KJ Schmieder, JMO Zide, A Barnett, C Ebert, R Opila, and MF Doty. Quantification of trap state densities in GaAs heterostructures grown at varying rates using intensity-dependent time resolved photoluminescence. *Applied Physics Letters*, 102(18):182108, 2013.

[39] Antonio Luque, Antonio Martí, Elisa Antolín, and César Tablero. Intermediate bands versus levels in non-radiative recombination. *Physica B: Condensed Matter*, 382(1):320–327, 2006.

[40] T. Trupke, R. A. Bardos, and M. D. Abbott. Self-consistent calibration of photoluminescence and photoconductance lifetime measurements. *Applied Physics Letters*, 87(18), 2005.

[41] R. A. Bardos, T. Trupke, M. C. Schubert, and T. Roth. Trapping artifacts in quasi-steady-state photoluminescence and photoconductance lifetime measurements on silicon wafers. *Applied Physics Letters*, 88(5), 2006.

[42] Ronald A Sinton and Andres Cuevas. Contactless determination of current–voltage characteristics and minority-carrier lifetimes in semiconductors from quasi-steady-state photoconductance data. *Applied Physics Letters*, 69(17):2510–2512, 1996.

[43] W. Bludau and E. Wagner. Recombination dynamics of electric-field-perturbed free carriers in gallium arsenide. *Journal of Luminescence*, 12–13:541 – 545, 1976. Proceeding of the 1975 International Conference on Luminescence.

[44] Takeshi Kamiya and Elmar Wagner. Shallow acceptor binding energy and lifetime of donor-acceptor pairs in gallium arsenide. *Journal of Applied Physics*, 47(7):3219–3223, 1976.

[45] RJ Nelson and RG Sobers. Minority-carrier lifetimes and internal quantum efficiency of surface-free GaAs. *Journal of Applied Physics*, 49(12):6103–6108, 1978.

[46] R. J. Nelson and R. G. Sobers. Interfacial recombination velocity in GaAlAs/GaAs heterostructures. *Applied Physics Letters*, 32(11), 1978.

[47] GB Lush, MR Melloch, MS Lundstrom, DH Levi, RK Ahrenkiel, and HF MacMillan. Microsecond lifetimes and low interface recombination velocities in moderately doped n-GaAs thin films. *Applied Physics Letters*, 61(20):2440–2442, 1992.

[48] GB Lush, HF MacMillan, BM Keyes, DH Levi, MR Melloch, RK Ahrenkiel, and MS Lundstrom. A study of minority carrier lifetime versus doping concentration in n-type GaAs grown by metalorganic chemical vapor deposition. *Journal of Applied Physics*, 72(4):1436–1442, 1992.

[49] P Asbeck. Self-absorption effects on the radiative lifetime in GaAs-GaAlAs double heterostructures. *Journal of Applied Physics*, 48(2):820–822, 1977.

[50] RK Ahrenkiel, DJ Dunlavy, Brian Keyes, SM Vernon, TM Dixon, SP Tobin, KL Miller, and RE Hayes. Ultralong minority-carrier lifetime epitaxial GaAs by photon recycling. *Applied Physics Letters*, 55(11):1088–1090, 1989.

[51] E. Yablonovitch, T. J. Gmitter, and R. Bhat. Inhibited and enhanced spontaneous emission from optically thin AlGaAs/GaAs double heterostructures. *Phys. Rev. Lett.*, 61:2546–2549, Nov 1988.

[52] E. Yablonovitch, T. Gmitter, J.P. Harbison, and R. Bhat. Extreme selectivity in the lift-off of epitaxial GaAs films. *Applied Physics Letters*, 51(26):2222–2224, 1987.

[53] DV Lang. Deep-level transient spectroscopy: A new method to characterize traps in semiconductors. *Journal of Applied Physics*, 45(7):3023–3032, 1974.

[54] GM Martin, A Mitonneau, and A Mircea. Electron traps in bulk and epitaxial GaAs crystals. *Electronics Letters*, 13(7):191–193, 1977.

[55] FD Auret, AWR Leitch, and JS Vermaak. A deep level transient spectroscopy analysis of electron and hole traps in bulk-grown GaAs. *Journal of Applied Physics*, 59(1):158–163, 1986.

[56] HJ Von Bardeleben, D Stievenard, D Deresmes, A Huber, and JC Bourgoin. Identification of a defect in a semiconductor: EL2 in GaAs. *Physical Review B*, 34(10):7192, 1986.

[57] A.R. Peaker. *Deep states in as-grown epitaxial GaAs.* In Brozel and Stillman [99], 1996.

[58] S. Yasuami. *Structure of native defects in undoped SI LEC GaAs.* In Brozel and Stillman [99], 1995.

[59] I Tkach, K Krambrock, and J-M Spaeth. On the problem of the EL2 structure in semi-insulating GaAs: high-frequency ODEPR/ODENDOR measurements in W-band. *Physica B: Condensed Matter*, 308:753–756, 2001.

[60] J Lagowski, HC Gatos, JM Parsey, K Wada, M Kaminska, and W Walukiewicz. Origin of the 0.82-eV electron trap in GaAs and its annihilation by shallow donors. *Applied Physics Letters*, 40(4):342–344, 1982.

[61] ER Weber, H Ennen, U Kaufmann, J Windscheif, J Schneider, and T Wosinski. Identification of As_{Ga} antisites in plastically deformed GaAs. *Journal of Applied Physics*, 53(9):6140–6143, 1982.

[62] Jaroslaw Dabrowski and Matthias Scheffler. Isolated arsenic-antisite defect in GaAs and the properties of EL2. *Physical Review B*, 40(15):10391, 1989.

[63] JF Wager and JA Van Vechten. Atomic model for the EL2 defect in GaAs. *Physical Review B*, 35(5):2330, 1987.

[64] M Kamińska, M Skowroński, and W Kuszko. Identification of the 0.82-eV electron trap, EL2 in GaAs, as an isolated antisite arsenic defect. *Physical Review Letters*, 55(20):2204, 1985.

[65] S Gupta, MY Frankel, JA Valdmanis, JF Whitaker, GA Mourou, FW Smith, and AR Calawa. Subpicosecond carrier lifetime in GaAs grown by molecular beam epitaxy at low temperatures. *Applied Physics Letters*, 59(25):3276–3278, 1991.

[66] David C Look, DC Walters, MO Manasreh, JR Sizelove, CE Stutz, and KR Evans. Anomalous hall-effect results in low-temperature molecular-beam-epitaxial GaAs: Hopping in a dense EL2-like band. *Physical Review B*, 42(6):3578, 1990.

[67] G Vincent and D Bois. Photocapacitance quenching effect for "oxygen" in GaAs. *Solid State Communications*, 27(4):431–434, 1978.

[68] H. C. Gatos and J. Lagowski. Comment on "identification of a defect in a semiconductor: EL2 in GaAs". *Phys. Rev. B*, 36:7668–7670, Nov 1987.

[69] H. J. von Bardeleben, J. C. Bourgoin, and D. Stievenard. Reply to "comment on 'identification of a defect in a semiconductor: EL2 in GaAs' ". *Phys. Rev. B*, 36:7671–7672, Nov 1987.

[70] H. J. von Bardeleben, J. C. Bourgoin, and D. Stievenard. Comment on "atomic model for the EL2 defect in GaAs". *Phys. Rev. B*, 39:1966–1966, Jan 1989.

[71] J. F. Wager and J. A. Van Vechten. Reply to "comment on 'atomic model for the EL2 defect in GaAs". *Phys. Rev. B*, 39:1967–1969, Jan 1989.

[72] P Trautman and JM Baranowski. Evidence for trigonal symmetry of the metastable state of the EL2 defect in GaAs. *Physical Review Letters*, 69(4):664, 1992.

[73] W Van Roosbroeck and W Shockley. Photon-radiative recombination of electrons and holes in germanium. *Physical Review*, 94(6):1558, 1954.

[74] T Trupke, Mr A Green, P Würfel, PP Altermatt, A Wang, J Zhao, and R Corkish. Temperature dependence of the radiative recombination coefficient of intrinsic crystalline silicon. *Journal of Applied Physics*, 94(8):4930–4937, 2003.

[75] S.A. Stockman. *Carbon doping of GaAs.* In Brozel and Stillman [99], 1995.

[76] P Wurfel. The chemical potential of radiation. *Journal of Physics C: Solid State Physics*, 15(18):3967, 1982.

[77] Simon M Sze and Kwok K Ng. *Physics of semiconductor devices.* John Wiley & Sons, 2006.

[78] U Strauss, WW Rühle, and K Köhler. Auger recombination in intrinsic GaAs. *Applied Physics Letters*, 62(1):55–57, 1993.

[79] RK Ahrenkiel, DJ Dunlavy, RY Loo, and GS Kamath. Minority-carrier lifetime in n-$Al_{0.38}Ga_{0.62}As$. *Journal of Applied Physics*, 63(10):5174–5176, 1988.

[80] D Redfield, JP Wittke, and JI Pankove. Luminescent properties of energy-band-tail states in GaAs: Si. *Physical Review B*, 2(6):1830, 1970.

[81] M Borgwardt, P Sippel, R Eichberger, MP Semtsiv, WT Masselink, and K Schwarzburg. Excitation correlation photoluminescence in the presence of Shockley-Read-Hall recombination. *Journal of Applied Physics*, 117(21):215702, 2015.

[82] JI Pankove. Absorption edge of impure gallium arsenide. *Physical Review*, 140(6A):A2059, 1965.

[83] Martin Gerber and Rafael Kleiman. Afterpulse background suppression in time-correlated single photon counting lifetime experiments using optimized gate filter. In *Photovoltaic Specialist Conference (PVSC), 2014 IEEE 40th*, pages 1899–1902. IEEE, 2014.

[84] LJ van der Pauw. A method of measuring specific resistivity and Hall effect of discs of arbitrary shape. *Philips Research Reports*, 13:1–9, 1958.

[85] Wolfgang Becker. *Advanced time-correlated single photon counting techniques*, volume 81. Springer Science & Business Media, 2005.

[86] Brian R Bennett, Richard A Soref, and Jesís A del Alamo. Carrier-induced change in refractive index of InP, GaAs and InGaAsP. *Quantum Electronics, IEEE Journal of*, 26(1):113–122, 1990.

[87] SM Sze and JC Irvin. Resistivity, mobility and impurity levels in GaAs, Ge, and Si at 300 K. *Solid-State Electronics*, 11(6):599–602, 1968.

[88] G.B. Lush. *Electron lifetime in p-type GaAs.* In Brozel and Stillman [99], 1995.

[89] G.B. Lush, M.R. Melloch, and M.S. Lundstrom. *Hole lifetime in n-type GaAs*. In Brozel and Stillman [99], 1995.

[90] R Cohen, L Kronik, A Shanzer, David Cahen, A Liu, Y Rosenwaks, JK Lorenz, and AB Ellis. Molecular control over semiconductor surface electronic properties: Dicarboxylic acids on CdTe, CdSe, GaAs, and InP. *Journal of the American Chemical Society*, 121(45):10545–10553, 1999.

[91] Jenn-Shyong Hwang, Zhijiang Hang, Shin-Long Tyan, Sheng-Wei Ding, Jen-Hsiung Tung, Chin-Yuan Chen, Biing-Jye Lee, and Jung-Tsung Hsu. Photoreflectance studies of $Ga_{0.5}In_{0.5}P$/GaAs heterostructures grown by metalorganic chemical vapor deposition technique. *Japanese Journal of Applied Physics*, 31(5A):L571, 1992.

[92] S Rein and SW Glunz. Electronic properties of the metastable defect in boron-doped Czochralski silicon: Unambiguous determination by advanced lifetime spectroscopy. *Applied Physics Letters*, 82(7):1054–1056, 2003.

[93] M Gandouzi, JC Bourgoin, L El Mir, M Stellmacher, and V Ortiz. Antisite incorporation during epitaxial growth of GaAs. *Journal of crystal growth*, 234(2):279–284, 2002.

[94] Darius Kuciauskas, Ana Kanevce, James M Burst, Joel N Duenow, Ramesh Dhere, David S Albin, Dean H Levi, and Richard K Ahrenkiel. Minority carrier lifetime analysis in the bulk of thin-film absorbers using subbandgap (two-photon) excitation. *Photovoltaics, IEEE Journal of*, 3(4):1319–1324, 2013.

[95] Tamotsu Hashizume. Surface Fermi-level position and gap state distribution of InGaP surface grown by metalorganic vapor-phase epitaxy. *Applied Physics Letters*, 81(13):2382–2384, 2002.

[96] Jianhui Chen, JR Sites, IL Spain, MJ Hafich, and GY Robinson. Band offset of GaAs/$In_{0.48}Ga_{0.52}P$ measured under hydrostatic pressure. *Applied Physics Letters*, 58(7):744–746, 1991.

[97] MA Haase, MJ Hafich, and GY Robinson. Internal photoemission and energy-band offsets in GaAs-GaInP p-i-n heterojunction photodiodes. *Applied Physics Letters*, 58(6):616–618, 1991.

[98] DE Holmes, RT Chen, Kenneth R Elliott, CG Kirkpatrick, and Phil Won Yu. Compensation mechanism in liquid encapsulated Czochralski GaAs: Importance of melt stoichiometry. *Electron Devices, IEEE Transactions on*, 29(7):1045–1051, 1982.

[99] M.R. Brozel and G.E. Stillman, editors. *Properties of Gallium Arsenide*. Institution of Electrical Engineers, Stevenage, United Kingdom, 1996.

[100] Armin G Aberle, Stefan Glunz, and Wilhelm Warta. Impact of illumination level and oxide parameters on Shockley-Read-Hall recombination at the Si-SiO_2 interface. *Journal of Applied Physics*, 71(9):4422–4431, 1992.

[101] Michael P Bristow. Suppression of afterpulsing in photomultipliers by gating the photocathode. *Applied optics*, 41(24):4975–4987, 2002.

[102] Mingguo Liu, Chong Hu, Joe C Campbell, Zhong Pan, and Mark M Tashima. Reduce afterpulsing of single photon avalanche diodes using passive quenching with active reset. *Quantum Electronics, IEEE Journal of*, 44(5):430–434, 2008.

Appendix A

Surface Recombination in the HLI Regime

Here, I address the question as to whether or not the surface recombination velocity can be decoupled from the decay using an expression (A.1) that I have derived for the deep-level dominated, injection-level dependent surface recombination velocity. In this limit, I demonstrate that the surface and bulk lifetimes have essentially the same injection-level dependence and therefore cannot be decoupled unless there is a significant difference between bulk and surface injection levels; however, I also fit data from the literature and demonstrate some validity of the model.

I have extended the SRH formalism by solving the general integral used by Stefan Rein [17] to describe surface recombination, for the specific case where surface recombination occurs mostly via midgap states. This is an effective density of states approach, where the more complex density of surface states is described by a single discrete deep energy level. The resulting effective surface recombination velocity (A.1) is parametrized by a minority carrier surface recombination velocity (S_{min}) and the ratio of surface capture cross sections for minority and majority carriers ($\sigma^S_{min}/\sigma^S_{maj}$).

$$S(\eta) = S_{min}\left(\frac{1+\eta}{1+\left(1+\frac{\sigma^S_{min}}{\sigma^S_{maj}}\right)\eta}\right) \tag{A.1}$$

As an example, I consider the two (equally well-passivated) surface case, following the approach of Sproul [4] to obtain (A.2) in terms of the film thickness (W).

$$\tau_S(\eta) = \frac{W}{2S_{min}}\left(1+\frac{\sigma^S_{min}}{\sigma^S_{maj}}\left(\frac{\eta}{1+\eta}\right)\right) \tag{A.2}$$

From (A.2), I see that the surface lifetime has a LLI value ($\tau^S_{LLI} = W/2S_{min}$), a HLI value ($\tau^S_{HLI} = (W/2)(S^{-1}_{min} + S^{-1}_{maj})$), and identical injection level dependence to the bulk SRH model ($\tau_S = (\tau^S_{LLI} + \tau^S_{HLI}\eta)/(1+\eta)$). As a result the bulk and surface lifetimes cannot be decoupled using injection-level variation, unless a significant deviation between the bulk and surface carrier densities exists.

The injection level dependence of the surface lifetime has been studied experimentally [100] with comparisons to theoretical equations that involve the input of cross sections, density of states and surface charge measured using complementary techniques. I have fit the data of [100] (see Fig. 13) with (A.1) obtaining comparable fit quality and measured parameters. Most notably, our fit yields $\sigma^S_n/\sigma^S_p = 2000 \pm 1000$, which agrees with the cross-sections ($\sigma_n = 2\times10^{-14}cm^2$ and $\sigma_p = 10^{-17}cm^2$) used in the theoretical calculations of [100].

Appendix B

Afterpulse Filtering Can Improve Acquisition Time

Photomultiplier tubes and avalanche photodiodes both exhibit a phenomenon called afterpulsing, when the detector emits a secondary pulse typically a few microseconds after it has emitted the primary pulse related to the detection of a photon. In high repetition rate experiments, these afterpulses are falsely recorded as photons, and show up as a signal-dependent background [85].

In order to obtain reliable lifetime results, it is desired that all background signals be subtracted. Removing both the background associated with dark counts and that associated with afterpulses comes at a cost of acquisition time; however, it is not productive to compare acquisition times between signals with and without significant systematic error. In this study, we make appropriate comparisons between situations that would result in the same degree of systematic error and assess acquisition time on this basis.

The subtraction of dark counts can be effectively executed by using a chopper and having the electronics add detection events when the chopper is open, and subtract events when it is closed [85]. This comes at a cost of a factor of two to the acquisition

time; however, it is crucial that the ADD/SUBTRACT signal is synchronized and in-phase with the TR-PLD signal to avoid SNR degradation due to signal subtraction.

In general, it is best to avoid using detectors with significant afterpulsing issues; however, the afterpulse background can be suppressed by increasing the dead time during an experiment in the case where an afterpulsing detector is the only option. The logical approach to removing this background involves reducing the repetition rate of the system [85]. This introduces an expected dead time given by (B.1) into the system every repetition for a given repetition rate, f_{rep}, since only one event can be recorded per repetition in a TCSPC system. This is an expected dead time, because the majority of events occur near $t = 0$ when the lifetime and repetition rate are low.

$$T_D = \frac{1}{f_{rep}^{low-rep}} \tag{B.1}$$

This approach works in theory; however, acquisition time increases dramatically. Often, repetition rates above 10MHz are desired, and to get a few microseconds of dead time, we would have to reduce our repetition rate (and detection rate) to ∼100kHz. So the acquisition time can increase by a few hundred times if afterpulsing is to be removed in this manner. We can recover some of this loss in acquisition time, while maintaining a dead time of T_D, by only introducing the dead time after each detection event. This gating method allows us to push the repetition rate above the 100kHz required to filter our afterpulses via repetition-rate reduction.

Let the ratio of detection events to repetitions be called r:

$$r = \frac{f_{det}}{f_{rep}} \tag{B.2}$$

The amount of acquisition time required to measure the same total number, N, of photons via the low-repetition-rate and gating methods is then:

$$\begin{aligned} T_{low-rep}^{Total} &= \frac{NT_D}{r} \\ T_{gated}^{Total} &= \frac{N}{rf_{rep}} + NT_D \end{aligned} \tag{B.3}$$

In the background-free case, both methods will result in the same ratio, r, of detection to repetition rates. Therefore, the improvement in acquisition time for the gated case relative to the low-repetition-rate case is given by:

$$\frac{T_{low-rep}^{Total}}{T_{gated}^{Total}} = \frac{f_{rep}T_D}{1 + rf_{rep}T_D} \tag{B.4}$$

Since $f_{rep}T_D > 1$ and $0 < r \leq 0.01$, we can place bounds on the potential acquisition-time improvement:

$$\frac{100}{101} < \frac{100f_{rep}T_D}{100 + f_{rep}T_D} < \frac{T_{low-rep}^{Total}}{T_{gated}^{Total}} < \frac{1}{r} < f_{rep}T_D \tag{B.5}$$

For various values of r, we can see how this improvement varies with $f_{rep}T_D$ in Fig. B.1.

The gating circuit used in this study (Fig. B.2) was a monostable multivibrator with a propagation delay of 31ns. The circuit contained a single monostable multivibrator integrated circuit (54HC4538) and other circuit elements to set the various time constants. The circuit diagram is given in the datasheet. The silicon single photon avalanche diode utilized has two outputs (analog and transistor-transistor logic, TTL), and one gate input. The analog signal is fed to the timing board, while the TTL signal can be sent to the monostable multivibrator. The output of the monostable circuit is connected to the gate of the detector, so that afterpulses that occur during the dead time of the circuit are suppressed.

Other groups have previously made circuits to gate photomultiplier tubes [101] and single photon avalanche diodes [102]; however, the examples in the literature require access to the gain voltage of the detector. In this circuit, we provide an external means

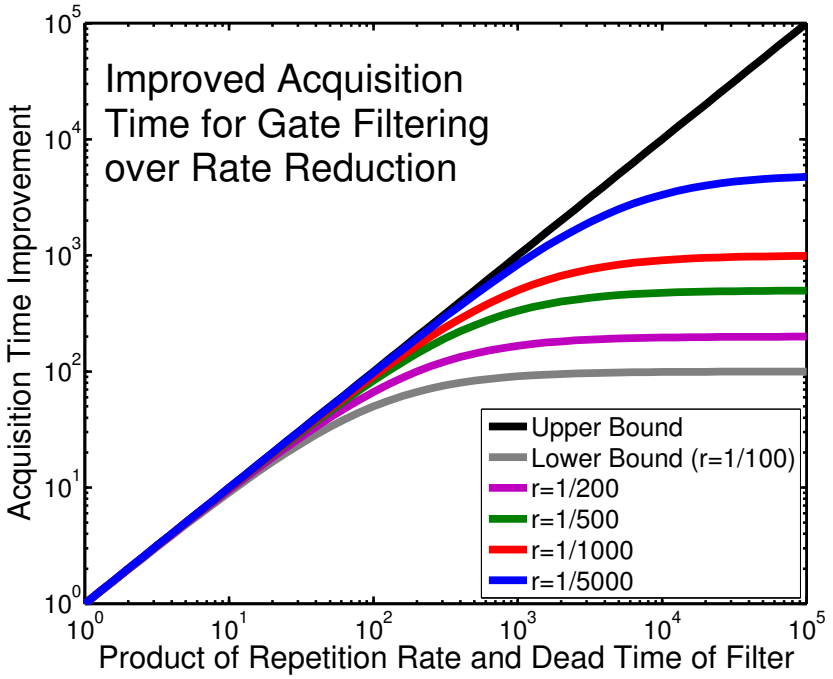

Figure B.1: Theoretical range of acquisition time improvements for gating of afterpulses, over the approach of reduced repetition rate.

of filtering afterpulses, for the case in which access to the gain voltage is limited.

Photoluminescence decay curves were taken at 40MHz with a 500nm GaAs DH (with InGaP capping layers). Lifetimes were measured at various dead time settings in the filter in order to optimize the time constant. If the time constant is too short, too many afterpulses get recorded. If the time constant is too long, then the acquisition time increases without any gain in quality of the result. The results shown in Fig. B.3 indicate that a $\sim$50 μs dead time is sufficient to block most of the afterpulse background, while the change from 50 to 200 microseconds is less drastic.

The largest contrast between ungated and gated signals was found for the largest time constant of 200 μs. Fig B.4 shows the impact of the 200 μs afterpulse filter. Note the improved linear dynamic range where the unfiltered result is linear for $\sim$10 ns ($\sim 2\tau$) whereas the filtered result is linear for $\sim 6\tau$.

The linearity of the logarithmic data is improved greatly by the afterpulse filter.

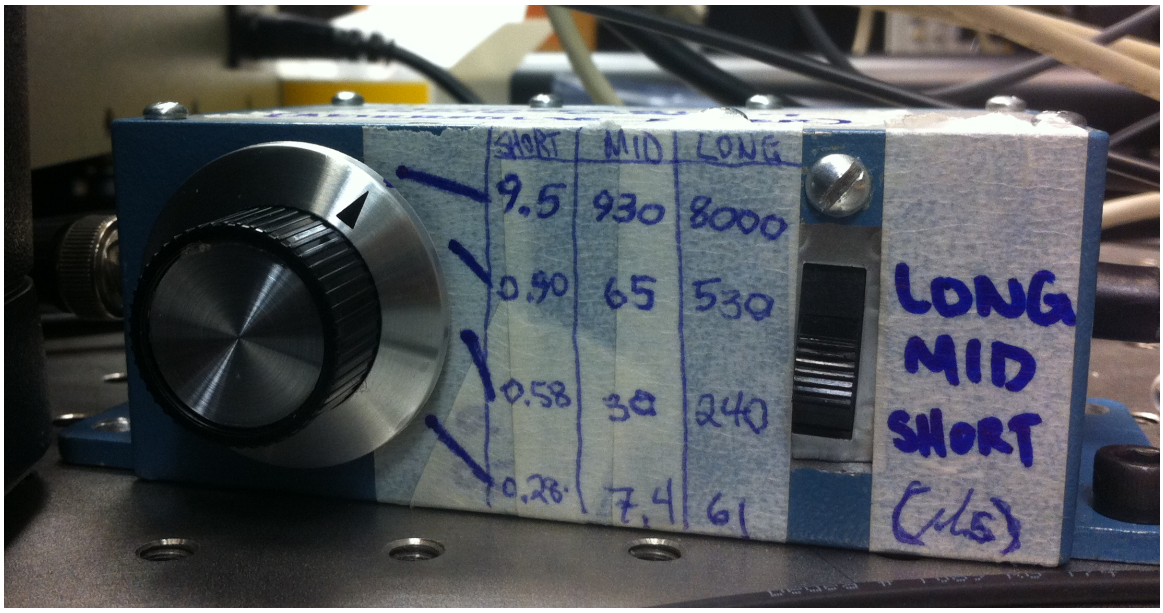

Figure B.2: Afterpulse filter (monostable multivibrator gate).

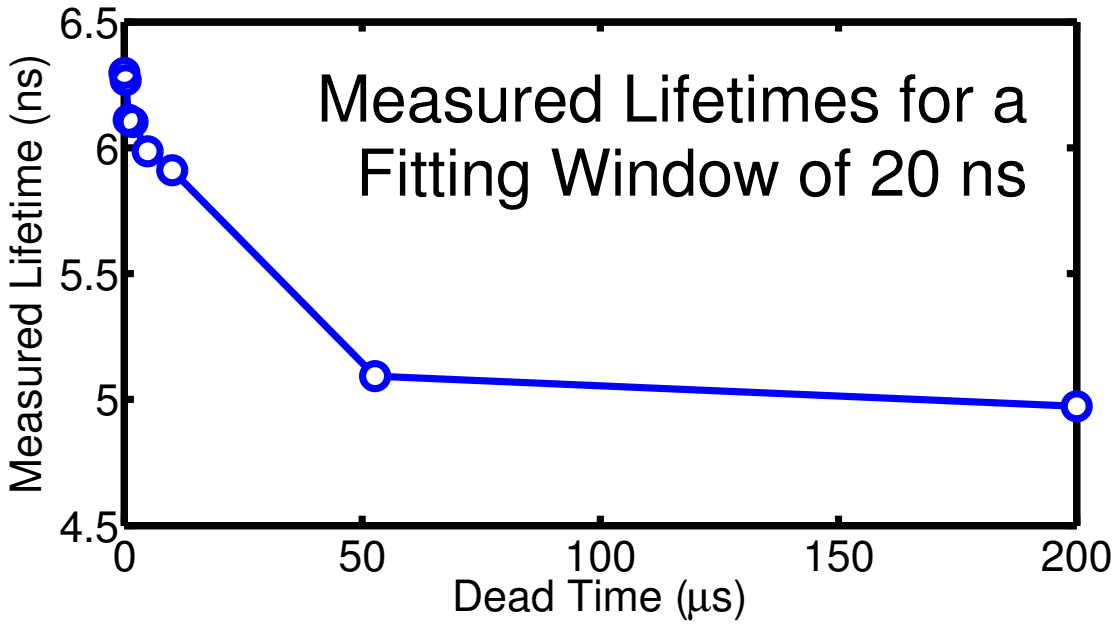

Figure B.3: Reduction in systematic error in measured lifetime as dead time of monostable gating circuit increases (at 40MHz).

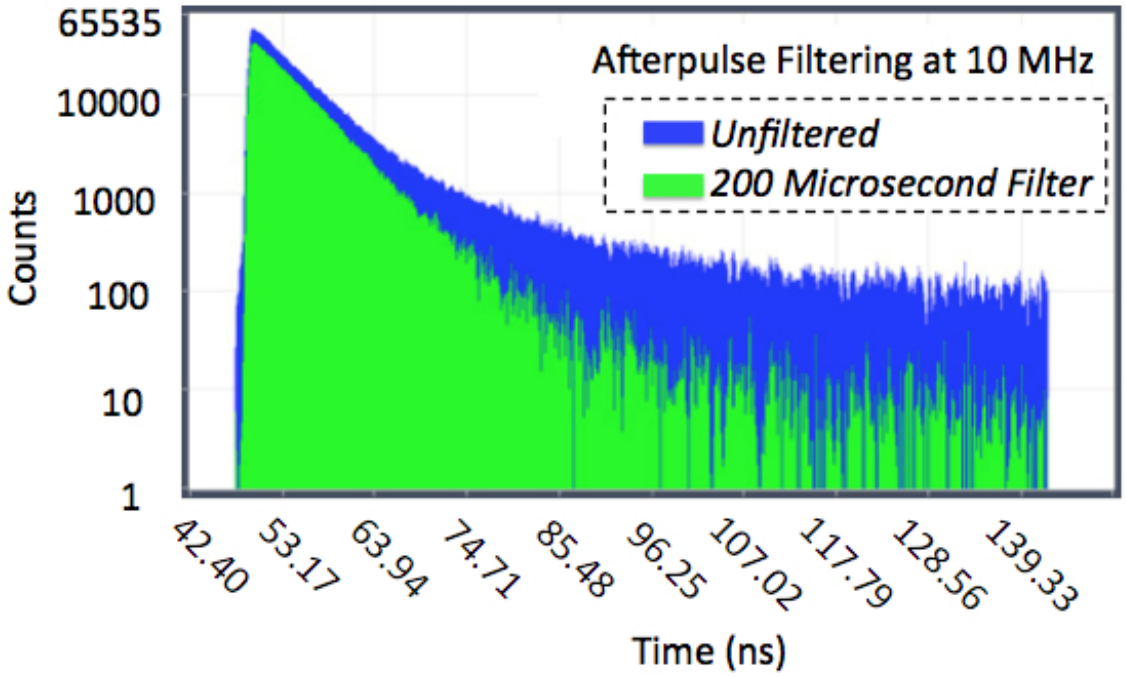

Figure B.4: Filtering of afterpulses is visually apparent at 10 MHz with a 200 μs dead time monostable filter.

Fig. B.5 shows unfiltered fit results alongside fit results from the optimized 53 μs filter. Note that the linear fit departs significantly from the data near the intercept in the unfiltered data, while the line remains within the range of the data in the filtered case.

In conclusion, the lifetime of the 500nm GaAs layer was found to be $\tau = (5.0 \pm 0.1) ns$. When compared with the lifetime measured in the unfiltered case ($6.3 ns$), we note that I have removed systematic error of $1.3 ns$, corresponding to 25% of the measured lifetime. Through repeated measurements under these conditions, the standard deviation of the mean was found to be $\sim$8 ps; however, this only accounts for the random noise and we are likely still in a situation where our uncertainty is dominated by systematic sources like afterpulsing and dark counts. This range has been narrowed down to less than $\pm 0.1 ns$ by analyzing the difference between the 200 and 53 μs results. With a systematic change of $0.1 ns$ to the closest data point, it would be unjustified to claim the purely random error magnitude of $8 ps$ as the uncertainty. Since we are removing

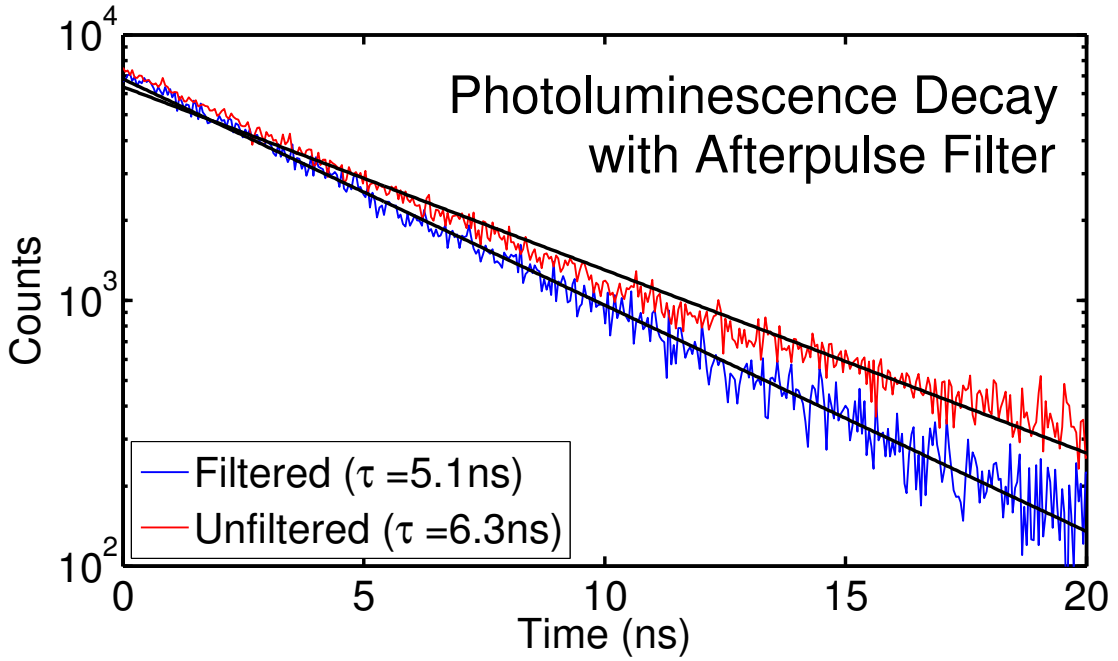

Figure B.5: Two linear fits highlighting improved linearity over the 4τ dynamic range with the 53 μs dead time monostable filter at 40MHz.

the dark background differentially, and suppressing the afterpulse background with the filter, this uncertainty estimate is probably overly conservative.

Theoretically, it was shown that the acquisition time for gating at high repetition rate to suppress afterpulsing is always shorter than that obtained by reducing the repetition rate, and by very large amounts for weak signals, low lifetimes, and long afterpulsing tails. The reduced repetition rate method suffers from a few microseconds of dead time every cycle, while the gating measurement only results in this dead time (at most) every 1 in 100 pulses. The value of the ratio, r, was estimated to be ∼0.14%, which corresponds to a ∼500X improvement in acquisition time when compared to a reduced repetition-rate experiment with the same effective dead time. Limits were placed on acquisition time improvement, in the case where an estimate for r is not known. For our optimized (53μs dead time) filter at 40MHz, we know that the improvement is between 100X and 2000X through application of (B.5).

A significant improvement in the dynamic range was shown to be attainable at

10MHz using a 200 μs filter. The improvement increased the linear regime from $\sim 2\tau$ to $\sim 6\tau$, as shown in Fig. B.4.

Appendix C

Effective Density of States

I have used nonlinear fitting to find an approximation (C.1) to the conduction-band density of states ($N_C(T)$) from IOFFE. The model for $N_C(T)$ takes into account the non-parabolicty[1] of the minimum at Γ, and from the contributions[2] from the X and L valleys. Fig. C.1 shows the fit to the IOFFE conduction-band effective-DOS, along with the valence-band effective-DOS for reference. The valence band follows the parabolic-approximation for effective-DOS ($N_V(T) = (1.83 \times 10^{15} cm^{-3}) T^{3/2}$, IOFFE). There was no physical motivation for the mathematical form of (C.1), but rather the form was chosen based on intuition and experience with exponential activations. Fig. C.2 shows that there is less than 2% error incurred from 77K to 700K.

$$N_C^{fit} = 8.369 \times 10^{13} cm^{-3} (1 + 52.39 e^{-171.5 meV/k_B T}) T^{3/2} \tag{C.1}$$

[1] The simple $T^{3/2}$ dependence in the DOS comes from the first-order (parabolic) approximation to the band-structure near the Γ minimum

[2] At sufficiently high temperature, indirect thermal excitation from the valence band Γ point to the minima at X and L becomes probable.

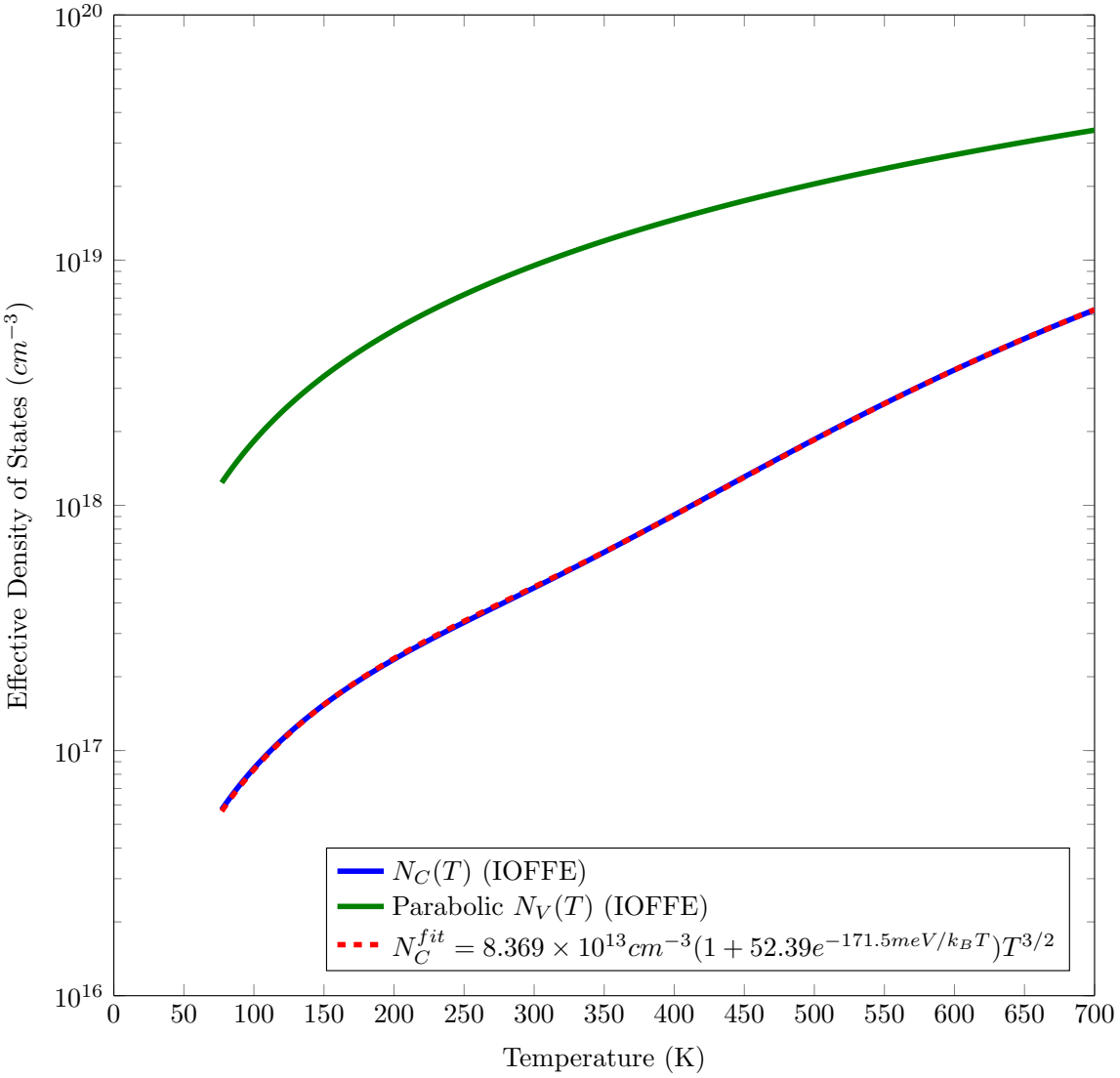

Figure C.1: Approximation (C.1) to the conduction band density of states.

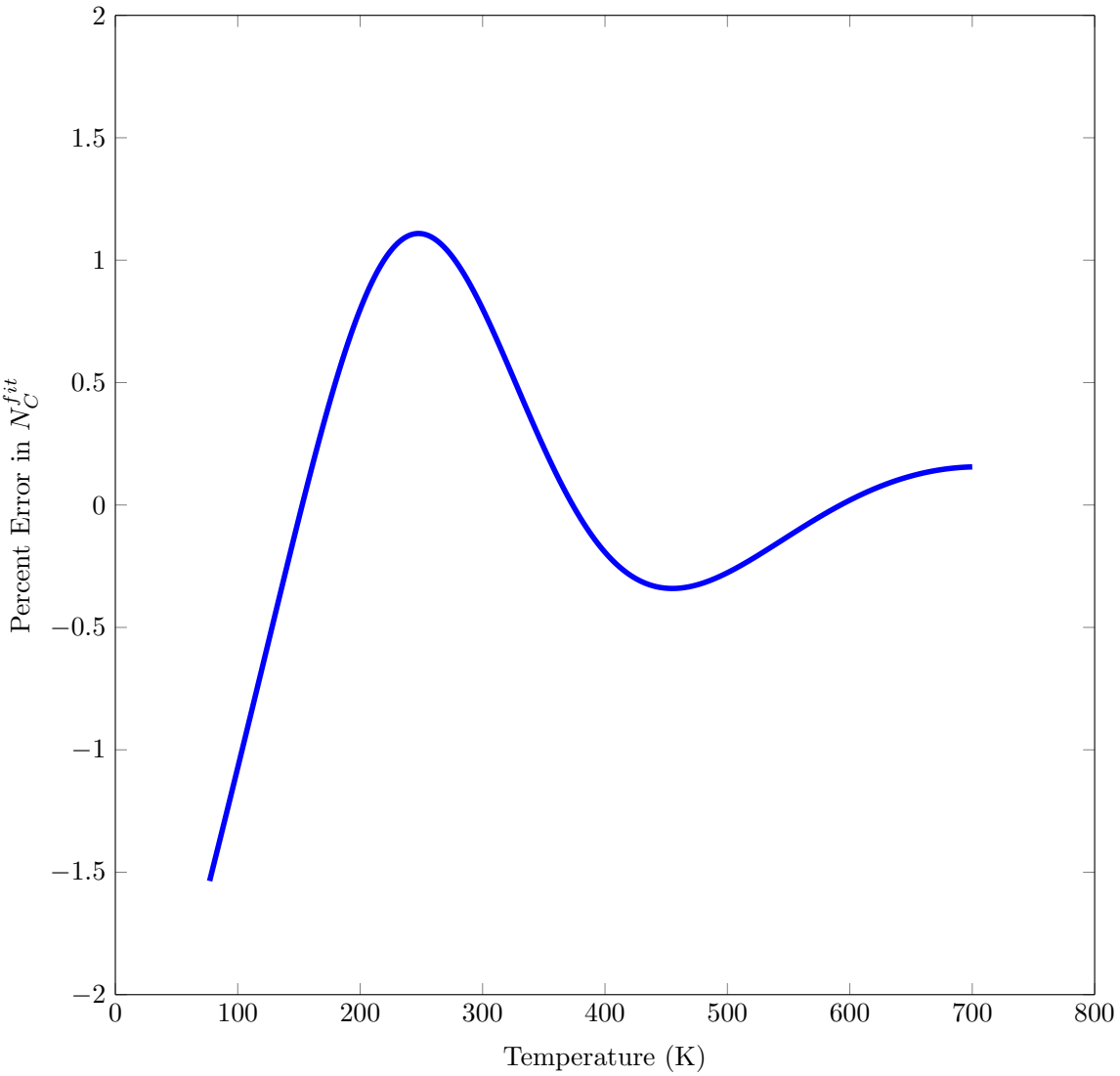

Figure C.2: Percent error (i.e. $100\% \times (N_C^{fit} - N_C^{IOFFE})/N_C^{IOFFE})$) associated with the approximation (C.1) to the conduction band density of states (shown in C.1).

Appendix D

Experimental Apparatus

I have taken some additional photographs of the experimental apparatus. Fig. D.1 shows the laser head, driver, and fibre, while Fig. D.2 shows diffuse 532nm reflections contained in the laser-confinement box. Liquid nitrogen is added to the cryostat through the funnel shown in Fig. D.3. The stabilized pressure reading from the Pirani gauge (Fig. D.4) using the pump in Fig. D.5 is shown in Fig. D.6. The interior of the cryostat must removed for sample mounting (Fig. D.7), leaving behind the cryostat base (Fig. D.8). Light is collected using a high solid-angle (F/#=1) lens, shown in Fig. D.9. The grating turret for the monochromator is shown in Fig. D.10. Photons are detected using an APD (Fig. D.11) and the detector pulses are timed using TCSPC electronics (Fig. D.12).

Figure D.1: Laser head, driver and fibre described above.

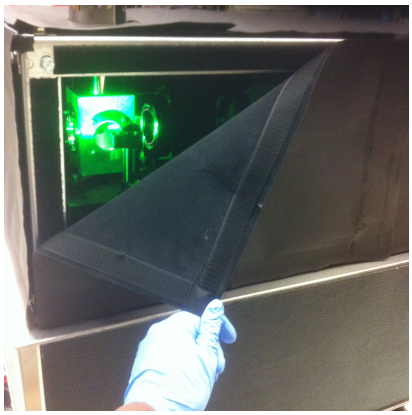

Figure D.2: Glow of the 532nm diffuse reflections (from the cryostat) contained by the laser-confinement box.

Figure D.3: Funnel used to fill cryostat with liquid nitrogen.

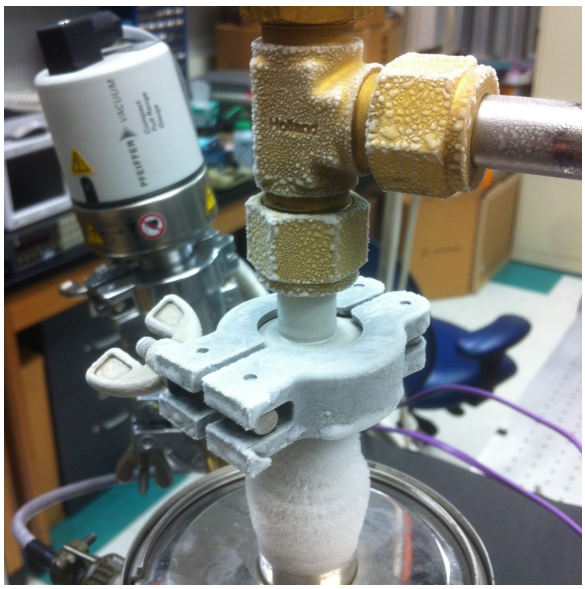

Figure D.4: Connection for filling liquid nitrogen, with Pirani gauge shown in the background (top left).

Figure D.5: Pumping station (turbo pump, with diaphragm backing pump).

Figure D.6: Stabilized 300K pressure reading (from Pirani gauge in Fig. D.4) of pump connected to cryostat (as shown in Fig. 4.1).

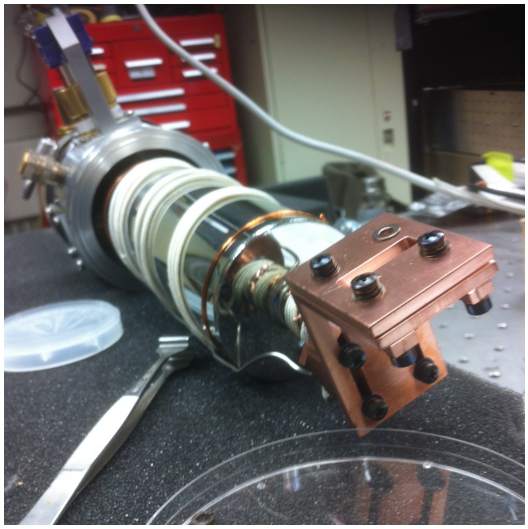

Figure D.7: Interior of cryostat is removed from the fixed sheath (see Fig. D.8) to access the copper sample holder.

Figure D.8: The base of the cryostat, with the interior (see Fig. D.7) removed for sample mounting.

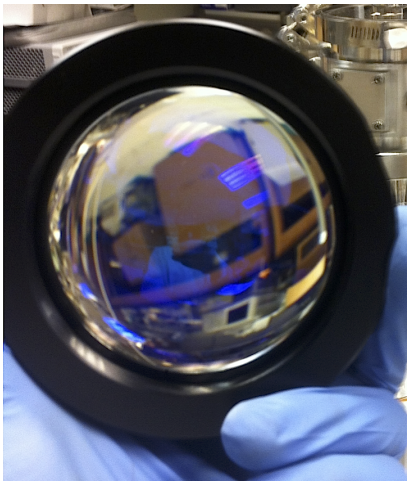

Figure D.9: High solid-angle (F/#=1) collection lens used in this work.

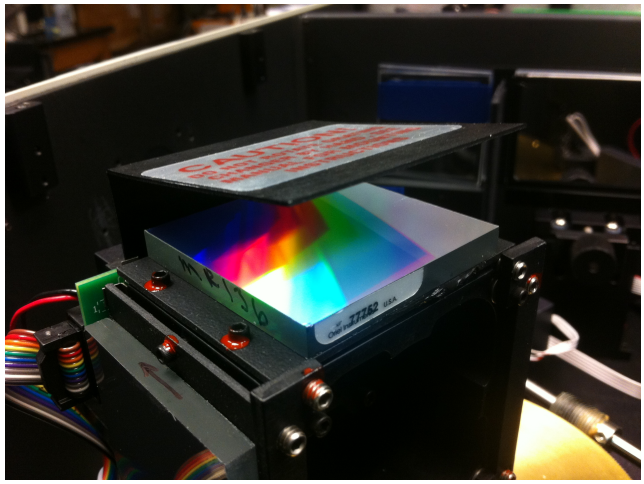

Figure D.10: Diffraction grating from monochromator.

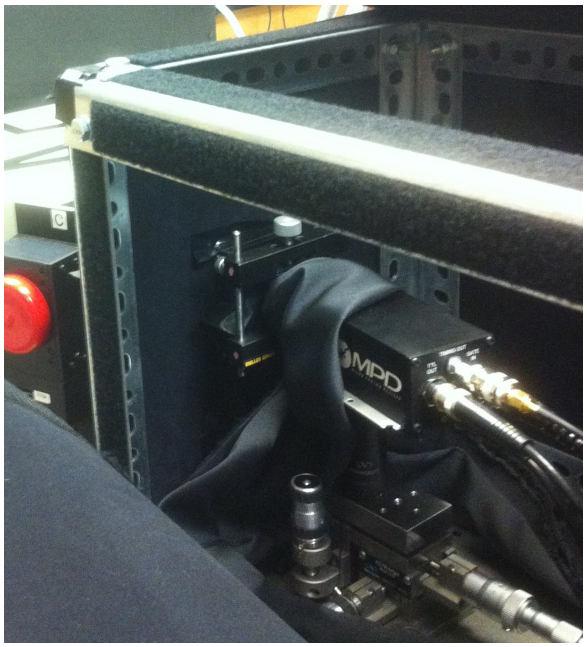

Figure D.11: Single-photon avalanche photodiode.

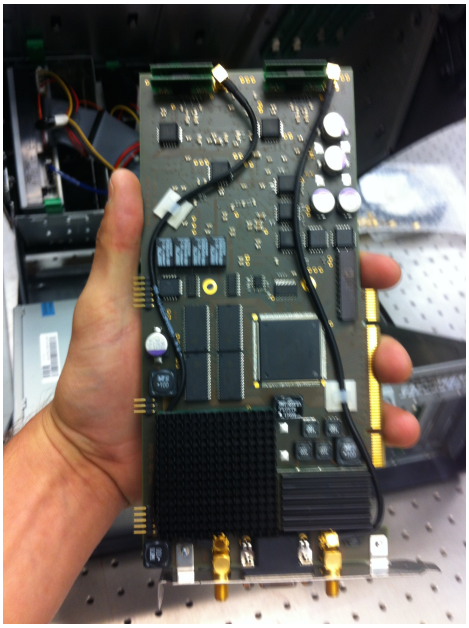

Figure D.12: Time-Correlated Single-Photon Counting (TCSPC) electronics.